Stress wave propagation in aircraft structures under bird impact

Author:
M.H. Schouten

AIRBUS

TU Delft Delft University of Technology

Stress wave propagation in aircraft structures under bird impact

by

M.H. Schouten

to obtain the degree of Master of Science at Delft University of Technology, to be defended publicly on Tuesday July 7, 2020 at 09:30 AM.

Student number:	4171233	
Project duration:	March 1, 2019 – July 7, 2020	
Thesis committee:	Prof. Dr. C. Bisagni,	TU Delft, Chair
	Dr. Ing. S. Heimbs,	Airbus
	Dr. C.D. Rans,	TU Delft
	Dr. Ir. J.M.J.F. van Campen,	TU Delft

TU Delft

Abstract

As collisions between aircraft and birds happen many thousands of times every year, all aspects of such impact events need to be taken into account in the process of designing an aircraft. One aspect that poses a risk is caused by the vibrations induced during bird impact. These vibrations are propagated through the aircraft structure by stress waves. Severe vibrations can negatively affect aircraft components and electrical systems located near the point of impact. While a vast amount of knowledge and research on the modelling of direct bird impact damage is already available, a gap in understanding exists regarding such vibrations.

The purpose of this thesis is to help fill this research gap. Therefore, this thesis tries to answer whether the shock effect caused by the stress waves generated during a bird impact on an aluminium alloy plate can be accurately predicted using state-of-the-art numerical modelling techniques. Two aspects are investigated. Firstly, it is evaluated whether the stress waves that propagate the impact loads through the structure can be identified in the model. Secondly, it is analysed how well the severity of the induced vibrations can be modelled.

This is done by utilising five bird impact tests, which were performed by Airbus. In each of these tests, a bird impacts an aluminium alloy test plate, which represents a simplified aircraft structure. A dummy mass, attached to these test structures, represents an electrical system influenced by the vibratory response of the plate. The displacement of the plate is recorded using digital image correlation (DIC). Accelerometers at several locations of the test structure are used to record the vibrations. The author created a dynamic explicit finite element model of the test structures to analyse how well current modelling techniques can determine these stress waves and vibrations. The structure in this model employs mostly conventional shell elements. For the bird, a smooth particle hydrodynamic (SPH) model is used.

Several types of stress waves are analysed. The main stress wave types evaluated are the in-plane longitudinal and the out-of-plane Rayleigh wave. An attempt is made to identify these waves in both the numerical model and the physical test. It is found that the DIC data of the impact test shows too much disturbance to evaluate these waves. In the numerical model, both an in-plane and an out-of-plane stress wave is seen. Their recorded velocities are seen to approach their theoretical value as the mesh is refined. The propagation velocity of the out-of-plane stress wave is found to depend on the structure of the mesh. When propagating diagonally to the mesh, a 17% lower wave propagation velocity is found compared to a wave travelling tangentially to the mesh.

No research was available in which the vibrations of an aircraft structure due to bird impact are analysed. Therefore, the shock response spectrum (SRS) technique, as applied in the space industry to evaluate the severity and damaging potential of vibrations, is utilised. This is the first known research in which an SRS is applied to a bird impact problem. In this research, the SRS is used to compare vibrations from the tests and the numerical model. Such an SRS is generated from the acceleration-time signal of a vibration. It is found that the trend of the SRSs obtained from the numerical model approximates the SRSs from the bird impact test closely. However, due to the fickle pattern of the SRSs, a maximum discrepancy of 5 to 10 dB between model and test is common.

Acknowledgments

While I am the one who has written this thesis, it would not have been possible without the help of a lot of people.

Firstly, I would like to thank all the people at Airbus Operations GmbH in Hamburg, Germany. Specifically, I want to thank Sebastian Heimbs and Erkan Kirtil for their supervision, advice and expertise on this difficult topic.

Secondly, I want to thank Chiara Bisagni, professor of aerospace structures and computational mechanics at Delft University of Technology. As my supervisor from the side of the university, she was able to guide me towards the finish line in the final stages of my work.

I want to acknowledge all the people that made my stay in Hamburg such a great experience. Especially Lucile and Robin and all the people at Generation Airbus.

Lastly, I want to thank the people who supported me in other ways in writing this thesis.

M.H. Schouten
Hamburg, June 2020

Contents

List of figures

List of tables

Nomenclature

Acronyms

CFR	Code of Federal Regulations
CS	Certification Specifications
DIC	Digital Image Correlation
DOF	Degree of Freedom
$EASA$	European Union Aviation Safety Agency
EoS	Equation of State
ESA	European Space Agency
FAA	Federal Aviation Administration
FE	Finite Element
FEM	Finite Element Method
$ICAO$	International Civil Aviation Organization
$NASA$	National Aeronautics and Space Administration
$SDOF$	Single Degree of Freedom
SPH	Smoothed Particle Hydrodynamics
SRS	Shock Response Spectrum

Roman

A	Cross-sectional area
a	Impactor radius
a_{fast}	Huth fastener type coefficient
B	Strain hardening coefficient
b_1, b_2	Huth joint coefficients
C	Huth shear flexibility
C_{CS}	Cowper-Symonds strain rate parameter
C_{int}	Intercept of the u_s-u_p curve
C_{JC}	Johnson-Cook strain rate coefficient
$C_0 - C_6$	Polynomial EoS constants
c	1D Longitudinal wave velocity
c_F	Flexural wave velocity in a plate
c_i	Wave velocity of wave i
c_L	Longitudinal wave velocity in a plate
c_R	Rayleigh wave velocity
c_r	Speed of sound in shocked material
c_S	Shear horizontal wave velocity
c_0	Speed of sound
D	Damage variable
D_{flex}	Flexural stiffness
D_1-D_5	Johnson-Cook damage parameters

d	Diameter
E	Young's modulus
E_i	Internal energy
E_m	Internal energy per unit mass
E_p	Plastic hardening modulus
f	Ordinary frequency
f_{max}	Maximum ordinary frequency
f_n	Ordinary natural frequency
G	Elastic shear modulus
g_k	Field variable of a particle k
h	Plate thickness
h_{smooth}	Smoothing length
J	Torsional constant
K	Bulk modulus
K_1	Fastener longitudinal stiffness
K_2, K_3	Fastener shear stiffnesses
K_4	Fastener torsional stiffness
K_5, K_6	Fastener bending stiffnesses
k	Material constant from linear Hugoniot equation
L	Length
l	Mesh size
l_{min}	Minimum element length
m	Thermal softening exponent
m_k	Mass of a particle k
N	Number of nodes per wavelength
N_p	Number of particles
n	Strain hardening exponent
p	Pressure
p_H	Hugoniot pressure
p_s	Steady flow pressure
p_0	Reference pressure
p_{CS}	Cowper-Symonds strain rate parameter
Q	Quality factor
q	Effective stress
r	Radial distance from impact centre
S_1, S_2, S_3	Grüneisen constants
T	Temperature
T_m	Melting temperature
T_r	Room temperature
T^*	Nondimensional (homologous) temperature
t	Time
t_B	Release wave travel time to impact centre
t_D	Impact duration
t_{max}	Time between impact and maximum displacement
u_p	Particle velocity
$\bar{u}^{pl}$	Plastic displacement
u_s	Shock wave velocity

u_0	Initial impactor velocity
V	Velocity
V_C	Cruise velocity
V_{imp}	Impact velocity
V_{rec}	Recorded velocity
v	Term of the interpolating kernel function
W	Interpolating kernel function
$\ddot{x}$	Acceleration response
$\vec{x}_i$	Position of a particle i
$\ddot{y}$	Base acceleration input

Greek

A	Murnaghan EoS constant
α	Grüneisen constant
α_R	Rayleigh mass proportional damping parameter
β_R	Rayleigh stiffness proportional damping parameter
β	Plastic hardening parameter
γ_0	Grüneisen gamma
γ	Murnaghan EoS constant
Δt	Time step
ΔV	Net velocity change
ΔX	Displacement in X-direction
ΔX_{max}	Maximum displacement in X-direction
$\Delta\bar{\epsilon}^{pl}$	Increment of equivalent plastic strain
E	Error
ϵ	Strain
$\dot{\epsilon}$	Strain rate
$\bar{\epsilon}^{pl}$	Equivalent plastic strain
$\dot{\bar{\epsilon}}^{pl}$	Equivalent plastic strain rate
$\bar{\epsilon}_f^{pl}$	Equivalent plastic strain at failure
ϵ_{vol}	Logarithmic volumetric strain
$\bar{\epsilon}_0^{pl}$	Equivalent plastic strain at damage initiation
$\dot{\epsilon}_0$	Reference strain rate
$\dot{\epsilon}^*$	Dimensionless plastic strain rate
ζ_1, ζ_2	Impact pressure distribution constants
η	Stress triaxiality
θ	Density ratio from EoS
λ	Wave length
μ	Density ratio from EoS
ν	Poisson's ratio
ξ	Damping ratio
ξ_i	Critical damping variable of mode i
ρ	Density
ρ_k	Density of a particle k
ρ_{ref}	Reference density
ρ_0	Initial density
σ	Stress

$\bar{\sigma}$	Stress of an undamaged element
σ_{vm}	Von Mises stress
σ_y	Dynamic yield stress
σ_{y0}	Yield stress at damage initiation
σ_0	Yield stress at $\bar{\epsilon}^{pl} = 0$
σ_1, σ_2, σ_3	Principal stresses
ω	Angular frequency
ω_d	Damped angular natural frequency
ω_i	Natural frequency of mode i
ω_n	Angular natural frequency

1

Introduction

1.1. Research motivation

The collision of aircraft with birds has been a problem since the very start of aeronautic history. The first impact of a bird onto an airplane was recorded by the Wright brothers in 1905 [1], less than two years after their first flight took place. In 1912 the first person was killed after a bird strike event [2]. From that moment, with ever-growing numbers of air travel, the number of reports of wildlife collisions has been rising. The most famous recent example of the problems caused by aircraft and birds sharing the same airspace occurred on the 15th of January 2009. A commercial Airbus A320 jetliner, taking off from LaGuardia, impacted a flock of birds, causing both engines to shut down. The pilots had to make an emergency landing in the Hudson river, ensuring the survival of all passengers and crew [3].

The occurrence of these problems is not just limited to a few incidents. Since 1988 wildlife strikes have globally lead to the death of over 262 people and the destruction of 247 aircraft. In the United States of America, 166.276 wildlife strikes were reported from 1990-2015 of which the vast majority involved birds. In 2015 alone the cost to US civil aviation was estimated to be 229 million [3]. According to the International Civil Aviation Organization (ICAO), 97.751 wildlife strikes were reported globally in the period from 2008-2015, which is a sharp increase from the period before [4]. This increase can largely be attributed to the continuing increase of air travel combined with a growth of the population of large birds [3]. The sections of the aircraft that are most likely to be struck are the windshield, wing, nose and radome [4].

To ensure safe flight of aircraft, aviation safety authorities require aircraft manufacturers to show the robustness of their vehicles in order to get certified. The FAA and EASA address this topic in their 14 CFR Part 25.571 and CS 25.631 certification documents, respectively. They require that large commercial aircraft assure a ”capability of continued safe flight and landing of the aeroplane after impact with a 4 lbs bird when the velocity of the aeroplane (relative to the bird along the aeroplane’s flight path) is equal to V_c at sea level or 0.85 V_c at 8000 ft, whichever is the more critical”[5]. Impact resistance must thus be shown for all front surfaces of the aircraft. In 14 CFR Part 25.631, the FAA poses the additional requirement that ”the empennage structure must be designed to assure capability of continued safe flight and landing of the airplane after impact with an 8-pound bird when the velocity of the airplane is equal to V_c at sea level”.

In addition to this, EASA [5] adds that ”Bird-strike induced deformations and *accelerations* on items, systems and equipment” should still allow for safe flight and landing. Currently, aircraft manufacturers such as Airbus only evaluate whether an aircraft structure is resistant to the damage caused directly by the contact between the bird and the structure. The accelerations experienced by equipment near the impact zone due to induced vibrations are

not considered in the certification process. However, increased reliance on electronic systems and their high concentration near the cockpit leads to a vulnerability to bird impact shock [6]. This indicates that, to assess the full effect of a bird strike, not only the direct impact damage should be analysed but also the accelerations induced by the impact shock.

For the evaluation of the impact tolerance of aircraft structures, aircraft manufacturers make vast use of numerical finite element modelling (FEM). These models have several advantages over physical testing, the most important one being a cost advantage, which has led to them replacing physical tests more and more [7]. With a numerical simulation, many tests with varying impact locations and orientations can be performed using the same model. Lastly, as these models are very detailed and can capture a large amount of different data types at a high frequency the impact event can be more easily understood. Thoroughly validated numerical models have even become accepted by aviation authorities as a valid way to show compliance with regulations [8].

However, as analysis of impact-induced stress waves and vibratory response has not been required for aircraft certification, the capabilities of these modelling techniques in this regard are unknown. In order to address the concerns regarding impact induced-vibrations and possible future requirements for aircraft certification, Airbus sought to investigate whether these vibrations could be simulated using existing FEM modelling techniques. Additionally, there was a desire from Airbus to determine whether the dynamic propagation of impact-induced stresses are correctly shown in these FE models.

In order to research this, Airbus performed several bird impact tests. However, when these tests were performed, no method had been chosen yet with which the results would be analysed. This was the starting point for the author of this thesis.

1.2. Research questions

It has become clear that there are still open questions regarding the vibratory response of a structure when impacted by a bird. This gap in research is twofold. Firstly, it is unknown whether the way in which the impact shock propagates through the structure is accurately captured using current modelling techniques. Secondly, the capability of these numerical models to simulate the effect of bird impact-induced vibrations on nearby located systems is unknown. This thesis aims to fill this gap. This leads to the following research question:

Can the shock effect caused by the stress waves generated during a bird impact on an aluminium alloy plate be accurately predicted using state-of-the-art numerical modelling techniques?

This research question is broken up into the following sub-questions:

- Can stress waves be correctly shown using a finite element model?
- Can the vibratory response of systems mounted near the impact zone be modelled?
  - What is the effect of using a Lagrangian bird model compared to a smoothed particle hydrodynamics model on calculation time and accuracy?
  - What is the effect of neglecting or including strain rate hardening in the material properties of the aluminium target on calculation time and accuracy?
  - What is the effect of using shell elements, continuum shell elements or solid elements on calculation time and accuracy?

1.3. Thesis outline

In this thesis, first, a summary of the history and information on bird impact modelling is given in Chapter 2. Additionally, this chapter describes several stress wave types through which loads are propagated through a material. Next, the test setup of the bird impact tests is described in Chapter 3. The numerical model based on this setup is presented in Chapter 4.

Chapter 5 details how the propagation velocity of stress waves is determined in both the impact tests and the numerical model. Additionally, this chapter provides the method to convert an acceleration signal into a shock response spectrum. This is used to evaluate the severity of vibrations generated during the bird impact. The results of the bird impact tests and the numerical model are described and compared in Chapter 6. The conclusions and recommendations for future work are given in Chapter 7.

2

Theoretical background

The risk of bird strike has been known for a long time. However, the first substantial research did not start until the 70s, when Wilbeck [9] started researching the pressure applied to a rigid target due to bird impact. Since then, a lot of interest in this topic has led to extensive research. This chapter will describe the basis of the bird impact problem. The early foundational work of Wilbeck will be shown in Section 2.1. The pressure generated by the bird is highly dependent on the behaviour of the material its body is made up off. Therefore, Section 2.2 gives several bird material formulations, which can be used to model the bird. The response of the impacted structure depends on the material used to create that structure. Some characteristics of metals that are of interest in this research, and ways to model these metals, are presented in Section 2.3.

In Section 2.4, some background information and history is given on the numerical modelling techniques used in this research. Section 2.5 describes different geometries with which the bird can be approximated when building a model. Lastly, multiple types of stress waves, with which impact loads propagate through the structure, are discussed in Section 2.6.

2.1. Soft body impact

To gain better understanding of the bird impact problem, Wilbeck tried to separate the influence of the physics related to the bird and that related to the interaction with the target. He did this by investigating the impact of birds on a rigid plate.

To describe a solid under impact, Hopkins and Kolsky [10] noted that the physical behaviour of a solid changes with impact speed. They characterised the behaviour at low speeds as elastic impact and for increasing impact speeds as plastic impact, hydrodynamic impact, sonic velocity impact and explosive impact. A hydrodynamic impact response occurs when the stresses in the material are much higher than its strength. This causes the material to behave as a fluid. During this behaviour it is not the strength of the material but its density which dominates material behaviour. This is the behaviour that can be observed in high velocity bird impacts and is called ‘soft body impact’ [9].

Taking this fluid like behaviour into account, it is possible to apply the theory of the impact of water jets to this problem. The process of a water jet impacting a surface can be split up into four different regimes as shown in Figure 2.1 [11]. At first, the impactor approaches the target, as shown in Figure 2.1a. Then, at the moment of impact, the particles of the projectile at the contact area are instantaneously brought to rest. This generates a shock wave, as shown in Figure 2.1b. This shock wave travels from the contact surface further in to the impactor, generating a high pressure area behind it. This high pressure is indicated by the shaded surfaces in Figure 2.1. As the pressure behind the shock wave is very high, while the pressure at the free edges of the jet is low, a high stress gradient is formed. Immediately after impact, this causes the impactor material to propel radially outward, which releases the

pressure at the outer edges of the bird. This causes a pressure release wave to form, which travels from the free edges to the centre of the projectile [8]. During the release regime, the release waves meet at the centre of the impact and the shock pressure is released from the surface. Several reflections of the release waves will cause the shock wave to weaken [8] and, for a subsonic impact, eventually disappear [9]. This is when steady flow is fully developed, as shown in Figure 2.1d, leading to a constant pressure and velocity [8]. For steady flow to fully develop, it is required that the impactor has a length over diameter ratio $L/d > 1$ [9]. The steady flow continues until the end of the projectile reaches the target surface and the impact event is terminated.

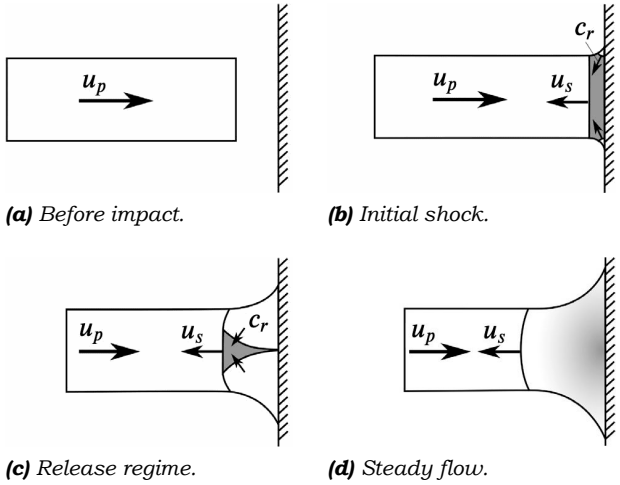

(a) *Before impact.* **(b)** *Initial shock.*

(c) *Release regime.* **(d)** *Steady flow.*

Figure 2.1: *Stages of bird impact [11].*

The pressure generated on the surface by the initial shock is given by Equation (2.1) [9] and is called the Hugoniot pressure p_H.

$$p_H = \rho_0 u_s u_0 \tag{2.1}$$

Here ρ_0 and u_0 are the initial density and initial velocity of the impactor, respectively. The shock wave velocity is given by u_s.

For a right circular cylinder, the duration of the release regime t_B is the time it takes for the release wave to travel from the free edge towards the centre. This is determined in Equation (2.2).

$$t_B = a/c_r \tag{2.2}$$

In this equation, a is the radius of the cylinder and c_r is the speed of sound in the shocked material [9].

The steady flow pressure at the centre of the impact is the stagnation pressure p_s. It can be derived from the Bernoulli equation and is given by Equation (2.3) [9]. This equation is valid for incompressible flow only.

$$p_s = \frac{1}{2}\rho_0 u_0^2 \tag{2.3}$$

The total duration of the impact event t_D is determined by the time it takes for the projectile to “flow through its length” [9], as given in Equation (2.4).

$$t_D = L/u_0 \tag{2.4}$$

Here, L is the length of the projectile. An example of the theoretical, experimental and numerical pressure - time history of a bird impact at the centre of a rigid plate was given by

Dar et al. in Figure 2.2 [12]. It can be seen that there is a significant discrepancy between the theoretical Hugoniot pressure and the peak pressure measured by Wilbeck. This was attributed by Wilbeck to the more rounded shape of a real bird compared to a flat cylinder, as well as the presence of feathers, legs and wings. Additionally, Dar et al. noted that, as the peak pressure only lasts for a few microseconds, this peak might not be recorded by the pressure sensors used by Wilbeck in the 1970s.

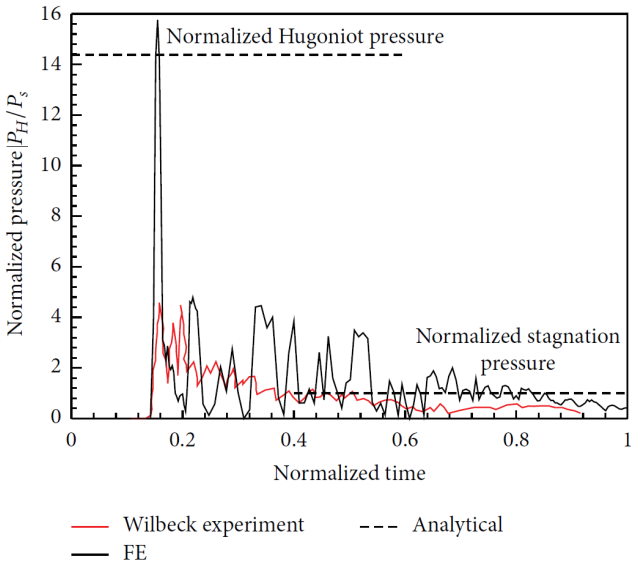

Figure 2.2: *Theoretical, experimental and numerical pressures at the centre of a rigid plate during bird strike [12].*

Two formulations have been derived for the contact pressure between the bird and the target during the steady flow regime. They are given in Equation (2.5) [13] and Equation (2.6) [14]. These equations give the contact pressure p as a function of the radial distance r from the centre of impact. These pressure distributions were originally derived for the normal impact of a water jet on a flat surface [15].

$$p = p_s \exp\left\{-\zeta_1 \left(\frac{r}{a}\right)^2\right\} \tag{2.5}$$

$$p = p_s \left\{1 - 3\left(\frac{r}{\zeta_2 a}\right)^2 + \left(\frac{r}{\zeta_2 a}\right)^3\right\} \tag{2.6}$$

Here a is the radius of the impactor, $\zeta_1 = 0.5$ and $\zeta_2 = 2.58$. It should be noted that this equation is only valid for incompressible fluids. However, it only shows small deviations for impact speeds commonly occurring in bird strikes.

2.2. Material model of the bird

To correctly represent the physical behaviour of the bird in a numerical model, two aspects need to be taken into account. Firstly, a constitutive model needs to be defined to determine the deformation of the bird when subjected to the encountered loads. Several constitutive models commonly used are described in Section 2.2.1. Secondly, as the bird experiences very high stresses and strains it will often break up into smaller sections. To include this behaviour in a numerical model, some failure criteria are discussed in Section 2.2.2.

2.2.1. Constitutive models

To be able describe how the impactor behaves, a constitutive model for the bird material needs to be set up. It was stated by Khan [16] that for this, an elastic-plastic hydrodynamic

solid model can be used. At low pressures this describes elastic-plastic isotropic behaviour. At high pressures such a model describes the hydrodynamic relation between pressure and volume using an equation of state (EoS). The equation of state gives the relationship between the volumetric strain in the bird material and the pressure p. Many variations of these relations are available.

The equation of state that is used most often is the polynomial equation shown in Equation (2.7) [17, 18]

$$p = C_0 + C_1\mu + C_2\mu^2 + C_3\mu^3 + (C_4 + C_5\mu + C_6\mu^2)E_i \tag{2.7}$$

where C_0-C_6 are material constants that can be experimentally determined and $\mu = (\rho/\rho_0) - 1$ [15]. The ratio ρ/ρ_0 gives the current mass density over the initial mass density and E_i is the internal energy. Some research suggests using fewer polynomial terms has a negligible effect while speeding up the numerical calculation [19]. Therefore, the effect of C_4-C_6 is sometimes neglected, as was done by Anghileri and Bisagni [20]. Parameter C_1 is also called the bulk modulus and is often called K [15].

The material constants C_1-C_3 can be derived from the pressure-density relation across a shock as given in Equation (2.8) [9, 16].

$$p = \frac{\rho_0 c_0^2 \theta}{(1 - k\theta)^2} \tag{2.8}$$

Here c_0 is the sound speed in the material, $\theta = 1 - \rho_0/\rho$ and k is a material constant as given in Equation (2.9) [9].

$$u_s = c_0 + k u_p \tag{2.9}$$

This equation is called the linear Hugoniot. It relates the velocity of a shock wave u_s in a material to the speed of sound c_0 and the particle velocity u_p, which, for impact on a rigid target, is equal to the initial velocity of the projectile [9]. For water, a value of $k = 2$ is often assumed [15]. It is found that the linear Hugoniot is valid for most fluids and solids, including air and water [9].

Using a series expansion of Equation (2.8) and neglecting C_4-C_6, this leads to the following expressions [16].

$$C_1 = \rho_0 c_0^2 \tag{2.10}$$

$$C_2 = (2k - 1)C_1 \tag{2.11}$$

$$C_3 = (k - 1)(3k - 1)C_1 \tag{2.12}$$

A simpler EoS, commonly used in hydrodynamics, is the Murnaghan EoS [8, 15]. It is described by Equation (2.13).

$$p = p_0 + \mathrm{A}\left[\left(\frac{\rho}{\rho_0}\right)^{\gamma} - 1\right] \tag{2.13}$$

In this equation, A and γ are material constants and p_0 is a reference pressure. The value of these material constants can be determined in two ways. In the first method, the values are determined by first taking reference values from literature. The analysis is then performed using these values. The simulation results are then compared to test results, after which A and γ are tweaked to achieve a better agreement between test and simulation. This technique is used by McCarthy [17], who found the values $\mathrm{A} = 128MPa$ and $\gamma = 7.98$. It should, however, be noted that different studies can give different values for these constants.

Alternatively, Wilbeck [9] described them using Equations (2.14) and (2.15)

$$\mathrm{A} = \frac{\rho_0 c_0^2}{4k - 1} \tag{2.14}$$

$$\gamma = 4k - 1 \tag{2.15}$$

The Murnaghan EoS is normally used for water. It assumes that no porosity is present. Porosity is the inclusion of air in the modelled material. Wilbeck [9], however, noted that a porosity of 10% gives the best agreement between tests and simulations. Therefore Wilbeck shows a way to adjust Equation (2.13) to take porosity into account by combining the Murnaghan EoS with an EoS of air [21].

One additional EoS is called the Grüneisen equation of state. For compressed materials, where $\mu > 0$, it is given in Equation (2.16) [8, 22].

$$p = \frac{\rho_0 C_{int}^2 \mu \left[1 + (1 - \frac{\gamma_0}{2})\mu - \frac{\alpha}{2}\mu^2\right]}{\left[1 - (S_1 - 1)\mu - S_2 \frac{\mu^2}{\mu+1} - S_3 \frac{\mu^3}{(\mu+1)^2}\right]^2} + (\gamma_0 + \alpha\mu)E_i \tag{2.16}$$

For expanded materials, where $\mu < 0$, the pressure is described in Equation (2.17) [22].

$$p = \rho_0 C^2 \mu + (\gamma_0 + \alpha\mu)E_i \tag{2.17}$$

Here, γ_0 is the Grüneisen gamma, E_i is the internal energy, C_{int} is the intercept of the u_s-u_p curve and S_1-S_3 and α are constants. Nizampatnam [21] stressed that the Grüneisen EoS is only valid for materials that remain solid through the entire impact and states that researchers who used this relation for hydrodynamic behaviour achieved less accurate results. However, the Grüneisen EoS is still used extensively in research. Alternative formulations of the Grüneisen EoS are also available, such as the simplified form given by Mohagheghian and Zhang [23, 24].

Often the choice of which EoS is used depends on which options are available in the particular finite element analysis software that is used. To give users freedom in their EoS definitions, many commercial software packages allow a tabulated EoS definition. In Abaqus such a relation is defined as given in Equation (2.18) [25].

$$p = f_1(\epsilon_{vol}) + \rho_{ref} f_2(\epsilon_{vol}) E_m \tag{2.18}$$

Here, f_1 and f_2 are functions of ϵ_{vol}, which is the logarithmic volumetric strain defined as $\epsilon_{vol} = ln(\rho_0/\rho)$. The parameter E_m is the internal energy per unit mass and ρ_{ref} is a reference density. A list with specific values of f_1 and f_2 can be implemented for a range of volumetric strains.

2.2.2. Failure criteria

In addition to a pressure-volume relationships given by the equation of state, the bird material requires a description of its failure criteria. While it is possible to not define a failure criterion, as was done by Anghileri [26], the impactor would not be able to fragment into smaller pieces but only show stretching. This may lead to inaccurate results or, when elements are stretched excessively, result in termination of the simulation. Most of the literature found does not give any information regarding the use of a failure criterion for the bird material, but some gives a basic description. One way of implementing failure behaviour is given by Stoll [27], who defines an ultimate stress value equal to the yield strength and deletes an element when its experienced stress exceeds this value. This ultimate stress value corresponds to a certain degree of flattening of an element. Liu [28] and Yulong [29] implemented a maximum failure strain as criterion for element deletion and Brockman [30] specifies an allowed 500% plastic deviatoric strain after which the element fails.

Dar et al. [12] describe how mass can be lost when elements are deleted, leading to inaccuracies. This can be prevented by, when an element is deleted, distributing the mass of the elements over the neighbouring nodes. The inertia of the impactor is thus retained and failed

sections can still interact with the target [12, 30]. In case all the elements of the impactor are deleted a cloud of independent point masses would thus remain [31].

2.3. Material model of the impacted structure

To model the dynamic behaviour of the structure the properties of the materials used to create this structure need to be known. Additionally, they need to be defined such that they can be used in a structural model. The literature found describes bird impacts on many different types of materials. These range from metals and plastics to composites, such as carbon fibre reinforced plastics and fibre metal laminates. In this research only material models for metals will be considered. In Section 2.3.1, possible constitutive relations of metals are described. In Section 2.3.2, several failure criteria are given.

2.3.1. Constitutive models

To describe the response of the target structure accurately, the key material characteristics must be captured by its constitutive relation.

Under loading, metals typically first experience linear elastic deformation up to their initial yield strength σ_0, as shown in Figure 2.3. This linear elastic behaviour depends solely on the Young's modulus E and the Poisson ratio ν, where E gives the slope of the linear section of the stress-strain curve [32].

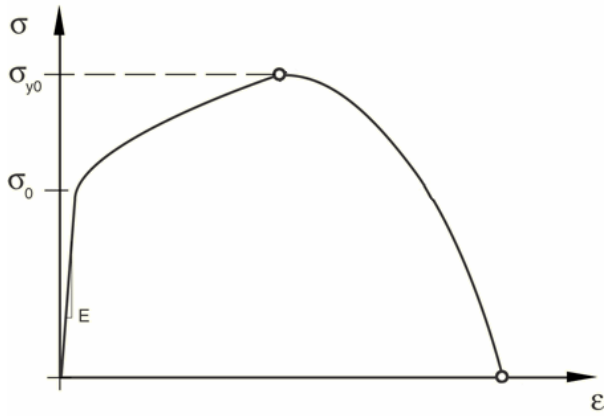

Figure 2.3: *Typical stress strain behaviour of metals [25].*

When the yield strength is exceeded, the material starts to deform plastically. This is shown in Figure 2.3 by the nonlinear behaviour after σ_0 is reached. Whether or not the yield strength is exceeded is determined by a yield criterion, of which the most popular, the von Mises stress criterion σ_{vm}, is shown in Equation (2.19) [33].

$$\sigma_{vm} = \frac{1}{\sqrt{2}}\sqrt{(\sigma_1 - \sigma_2)^2 + (\sigma_2 - \sigma_3)^2 + (\sigma_3 - \sigma_1)^2} \tag{2.19}$$

In this equation σ_1, σ_2 and σ_3 are the principle stresses. The von Mises stress criterion can be thought of as a cylinder in the stress space, whose centre axis coincides with the main diagonal $\sigma_1 = \sigma_2 = \sigma_3$ and whose radius is $\sqrt{2/3}\sigma_y$, where σ_y is the dynamic yield stress. This is shown in Figure 2.4. The surface of this cylinder is called the yield surface. When the von Mises stress of the material changes from a point inside this cylinder to a point on the yield surface, the von Mises stress equals the yield stress. If the von Mises stress then increases to a point outside the cylinder, the material starts to deform plastically [33]. As plastic deformation occurs the material experiences plastic hardening, which causes the yield surface to change. As explained by Oller [34], two types of plastic hardening exist. The first is called isotropic hardening, which results in a radial expansion of the stress cylinder.

The second is kinematic hardening, which lead to a translation of the described cylinder. Therefore, after kinematic hardening has taken place, the material behaviour is not isotropic anymore. These two types of hardening are visualised in Figure 2.5.

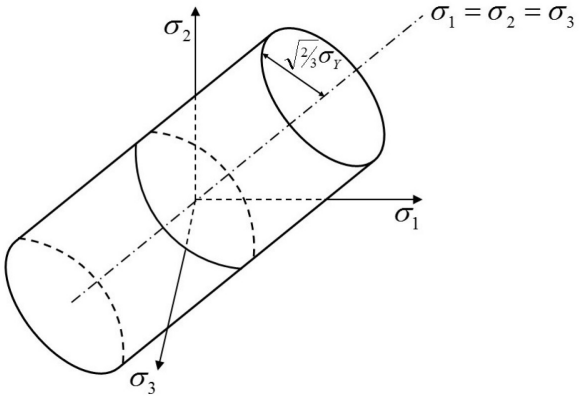

Figure 2.4: *The von Mises stress cylinder [35].*

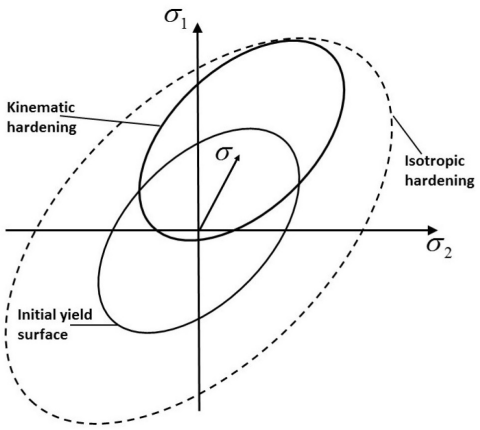

Figure 2.5: *Isotropic and kinematic hardening [35].*

Another effect on material behaviour is determined by the strain rate $\dot{\epsilon}$. As bird impact is a highly dynamic phenomenon, taking in the order of milliseconds, high strain rates occur [21, 36]. Strain rate increases with impact velocity and rates of up to $\dot{\epsilon} = 300s^{-1}$ may be reached for bird impacts at $180m/s$ [37]. Many types of materials, including a lot of metals, experience a sensitivity to strain rate. This is called strain rate hardening [33]. This hardening causes the plastic section of the stress strain curve to shift upward, giving more resistance to deformation at higher strain rates. An example of this is seen in Figure 2.6, which shows the strain rate sensitivity of an aerospace grade aluminium alloy.

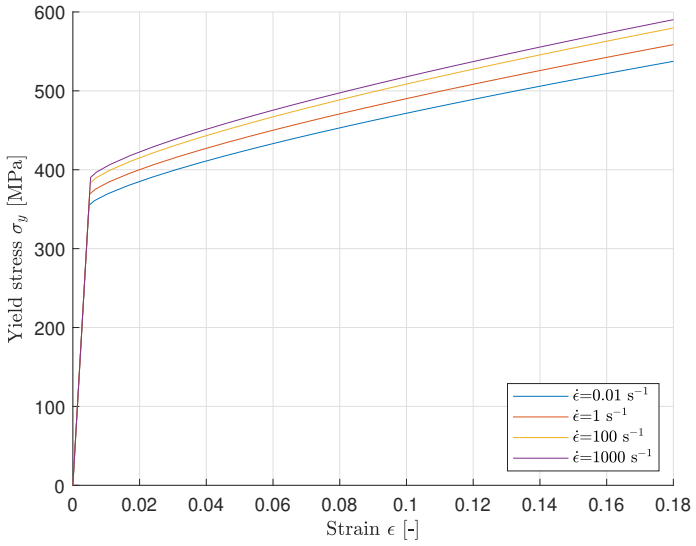

Figure 2.6: *Strain rate effect on the plasticity of an aerospae grade aluminium alloy. Created using Equation* (2.22) *and the material definition given by Kay [38].*

It may not always be necessary to include the strain rate effect in the material model. Heimbs et al. [32] observed that for the aluminium alloy AA6061 no significant strain rate effects are present at rates of up to $\dot{\epsilon} = 1000s^{-1}$ and thus did not take strain rate into account. Similarly, Liu [39] ignored strain rate effects for the aluminium alloys 2024 and 7075 as these were deemed insensitive to strain rate. This may, however, lead to a conservative

result. Smojver et al. [40] specifically state the importance of including the strain rate effect for aluminium alloy 2024. In a bird impact analysis, Smojver et al. found a 31% lower maximum deformation of a wing leading edge slat when including strain rate effects. This was true even though a relatively low impact velocity of $90m/s$ was used.

Finally, the effect of temperature is considered, which Johnson and Cook [41] called thermal softening. It describes a decrease in material strength at elevated temperatures. While some literature states that temperature effects are taken into account [24, 42, 43], often it is neglected [37, 44]. The temperature increase of the material during deformation due to conversion of kinetic energy into heat has not been mentioned in any literature that was found. This is therefore not believed to play an important role in bird impacts.

One material model that can be used to describe the plastic behaviour of metals is the Cowper-Symonds material model. It describes the dynamic yield stress σ_y, as given in Equation (2.20) [29]. The term in the first set of brackets gives the plastic hardening effect. The term in the second set of bracket is the Cowper-Symonds strain rate hardening effect. In Equation (2.20), the described plastic hardening effect shows linear plastic hardening behaviour. That is to say, for a change in plastic strain, a proportional change, scaled by the plastic hardening modulus E_p, is observed in the yield strength.

$$\sigma_y = [\sigma_0 + \beta E_p \bar{\epsilon}^{pl}][1 + (\dot{\epsilon}/C_{CS})^{1/p_{CS}}] \tag{2.20}$$

Here, σ_0 is the yield stress when no plastic strain is present, $\bar{\epsilon}^{pl}$ is the equivalent plastic strain, $\dot{\epsilon}$ is the strain rate and C_{CS} and p_{CS} are the Cowper-Symonds strain rate material parameters, respectively. The constant β is the hardening parameter, which ranges from 0 for purely kinematic hardening to 1 for fully isotropic hardening.

An alternative description of the strain hardening effect is given in Equation (2.21) [28] by a power law relation.

$$\sigma_y = [\sigma_0 + B(\bar{\epsilon}^{pl})^n][1 + (\dot{\epsilon}/C_{CS})^{1/p_{CS}}] \tag{2.21}$$

where B is the strain hardening coefficient and n is the strain hardening exponent. The strain rate effect is still described by the Cowper-Symonds term. Both these Cowper-Symonds material models neglect the effect of thermal softening.

A more elaborate description of the dynamic yield stress σ_y is given by Johnson and Cook in Equation (2.22) [41]. Here the first term is the same as in Equation (2.21) and gives the plastic hardening effect. The second term gives a different description of the strain rate hardening effect. Additionally the Johnson-Cook model gives a term for thermal softening in the final set of brackets.

$$\sigma_y = [\sigma_0 + B(\bar{\epsilon}^{pl})^n][1 + C_{JC} \ln \dot{\epsilon}^*][1 - (T^*)^m] \tag{2.22}$$

Here, $\dot{\epsilon}^* = \dot{\bar{\epsilon}}^{pl}/\dot{\epsilon}_0$ is a dimensionless plastic strain rate, where $\dot{\bar{\epsilon}}^{pl}$ is the equivalent plastic strain rate and $\dot{\epsilon_0}$ is a user defined reference strain rate, often taken as $\dot{\epsilon_0} = 1s^{-1}$. The homologous temperature of the material is given by $T^* = (T - T_r)/(T_m - T_r)$, where T, T_r and T_m are the current temperature, room temperature and melting temperature, respectively. Parameter C_{JC} is the Johnson-Cook strain rate coefficient and m is the thermal softening exponent. The homologous temperature is limited to a minimum of 0 for which the thermal softening disappears and a maximum of 1, after which the material is in its molten state. The Johnson-Cook model is very well known and used in models such as those of Vignjevic and Zhang [24, 43] and sometimes used while neglecting the thermal softening term as done by Langrand [44].

The material behaviour can also be described in tabulated form as used by Heimbs et al. [32]. In Abaqus this is done by defining a set of yield stresses for specific values of plastic strain. Abaqus will then generate a continuous stress-strain curve by interpolating these data points. Additionally, multiple curves can be stated for varying strain rates and temperatures.

2.3.2. Failure criteria

In case the target material in an impact problem is at risk of exceeding the failure strength or strain, a failure criterion must be defined. Regrettably, most authors do not mention which material failure criteria they use for the target. However, some authors state using a maximum tensile strain criterion. In this criterion, an element is removed once a certain level of strain is reached. For the aluminium alloys 7075 and 2024, Liu et al. used a strain limit of 0.14 and 0.2, respectively [39]. Other literature implementing a tensile strain limit is given by Heimbs et al. and Liu et al. [32, 37]. Instead of a tensile strain limit, Smojver et al. [40] use a shear failure criterion. This criterion states that when the equivalent plastic strain reaches a defined limit, an element fails. It is said to be specifically suited to dynamic problems.

2.4. Numerical modelling methods

When performing a numerical bird strike analysis, there are several numerical modelling techniques that can be applied. The earliest numerical analyses decoupled the bird and target models. The influence of the bird on the target was purely described as a pressure distribution on the impacted structure. This started with using a uniform pressure load over a specified amount of time. Later pressure functions included a variation in pressure with time and distance of from the centre of impact [8]. These pressure functions are however unable to capture interactions between the impactor and the target. Therefore, this chapter describes the two most commonly used numerical methods in bird impact modelling.

The modelling of the target structure is almost exclusively done using a Lagrangian formulation, which is described in Section 2.4.1. The Lagrangian approach can also be used when modelling the bird. The second numerical method is the smooth particle hydrodynamic (SPH) formulation and is described in Section 2.4.2. SPH models fluid-like behaviour and is therefore only used to model the bird and not the structure.

2.4.1. Lagrangian formulation

In the Lagrangian approach, the mesh and its corresponding nodes are attached to the material that it describes. This means that as the material translates, rotates and deforms the mesh does as well, as shown in Figure 2.7. A Lagrangian approach is most often used when modelling solids. In the research that was found, the target structure was always described using the Lagrangian formulation. Additionally, the Lagrangian method can be used to model the bird.

A benefit of the Lagrangian formulation is the application of the boundary conditions. As the mesh moves with the material the edges of an object are exactly defined and it is easy to apply boundary conditions to the material boundaries. Additionally, the Lagrangian approach makes it very easy to track the material properties over time [45].

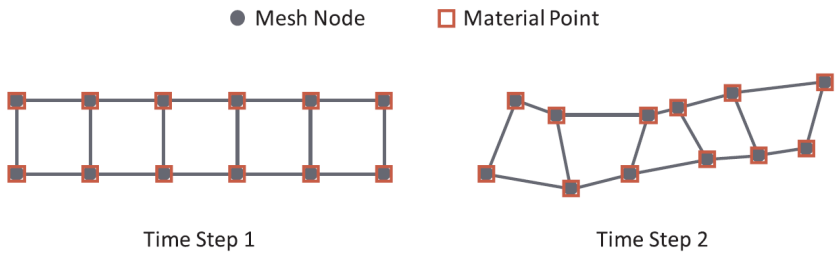

Figure 2.7: *Illustration of a Lagrangian modelling approach [18].*

When using the Lagrangian method to describe the bird, the large deformations experienced by the bird lead to several problems. Firstly, the elements will experience the same large deformations as the material, which leads to a decrease in mesh quality and a loss in accuracy [18]. Secondly, when modelling a highly dynamic impact problem, use is made of an explicit finite element analysis. For such an analysis the time step Δt used is dependent on the

minimum element length l_{min}. This time step is determined using Equation (2.23) [45]

$$\Delta t = \frac{l_{min}}{c_0} \tag{2.23}$$

where c_0 is the speed of sound. The large mesh distortions will cause some element dimensions to contract drastically. This leads to a large increase in the calculation time needed [45].

Finally, highly deformed elements might lead to severe hourglassing and even develop negative volumes, which can lead to termination of the calculation. The high element deformation can also generate an artificial stiffness, which reduces the accuracy of the generated impact pressure [8].

One solution to this problem is to delete an element once a certain strain limit is reached. Different failure criteria can be used, such as the shear failure criterion used by Zhu [46] and Brockman [30] or limiting the degree of flattening as used by Stoll [27]. However, choosing a failure limit that leads to good results can be challenging [26]. Additionally, element erosion can generate other inaccuracies as strain energy and mass is taken out from the system [21]. This can partly be solved by distributing the mass of a deleted element over its neighbouring nodes and retaining freed nodes in the model as point masses. This will preserve both mass and momentum and leaves these freed nodes to interact with other elements [27].

Another problem is that the deletion of elements induces oscillations in the contact forces. As the bird is discretised into elements, the deletion of such elements in the contact area results in a sharp drop in contact pressure. This contact pressure is regained when the next element contacts the target. The magnitude of these oscillations is dependent on mesh size. Mao et al. [47], who used a bird to element length ratio of 1/30, found that by using a refined mesh the oscillations could be reduced to a negligible level.

In the second solution, when deformations become too large the highly deformed area is remeshed in between calculation steps. This removes the distortion of the elements and will thus lower the inaccuracies related to mesh quality and increase the time step. The remeshing step will, however, add to the solution time, introduce its own inaccuracies and in some situations might not be possible at all [21].

2.4.2. Smoothed particle hydrodynamics formulation

The second commonly used method is the smoothed particle hydrodynamics (SPH) method. The SPH modelling method is only used to model the bird and not the structure. This method was developed in 1977 by Gingold and Monaghan [48] and Lucy [49] to model astrophysical phenomena. In the 90s, Groenenboom used this method in hypervelocity impact problems of space debris [50]. The use of SPH in bird impact modelling was first done by Audic [51] in 2000. In recent literature, the SPH method has grown to be the most popular formulation in modelling bird strike problems.

The SPH formulation consists of discrete interacting particles not connected to each other by elements. It is thus said to be a meshless approach. The lack of a mesh allows the object to deform greatly without resulting in numerical instabilities or inaccuracies related to highly deformed elements. Thus, it does not require the deletion of such highly deformed elements [52]. This makes it highly suited for problems with large deformations or when the impactor is split into multiple pieces. It is thus commonly used to model materials behaving as fluids. The SPH formulation is a Lagrangian technique, which allows it to be used in combination with a Lagrangian model for the structure with a relatively simple interaction formulation. The equations below show the core functions of the SPH method [21].

The value of field variables g of a particle i at position $\vec{x}_i$ depend on the other particles in the model and are approximated by the discrete kernel approximation given in Equation (2.24) [21, 51].

$$\langle g(\vec{x}_i)\rangle = \sum_{k=1}^{N_p} m_k \frac{g_k}{\rho_k} W(\vec{x}_i - \vec{x}_k, h_{smooth}) \tag{2.24}$$

In this equation m_k and ρ_k are the mass and density of particle k, respectively. The variable h_{smooth} is the smoothing length of particle i and N_p is the number of particles that fall within the sphere of influence of particle i. The function W is the interpolating kernel function and its most used version is the B-spline as given in Equation (2.25) [21, 51]

$$W(v, h_{smooth}) = \frac{1}{\pi h_{smooth}^3} \begin{cases} (1 - \frac{3}{2}v^2 + \frac{3}{4}v^3) & 0 < v < 1 \\ \frac{1}{4}(2 - v)^3 & 1 < v < 2 \\ 0 & other \end{cases} \tag{2.25}$$

where $v = \frac{|\vec{x}_i - \vec{x}_k|}{h_{smooth}}$. An illustration of a kernel function is shown in Figure 2.8.

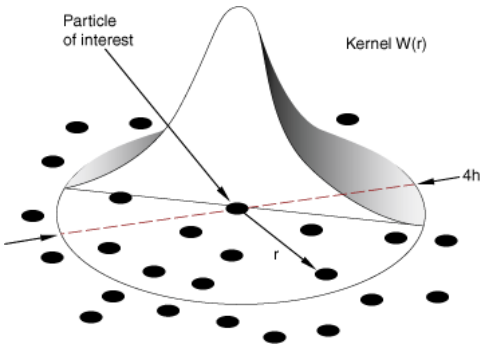

Figure 2.8: *A 2-dimensional representation of a kernel function [25].*

It can be seen that when the distance of a particle k to particle i is larger than $2h_{smooth}$ the interpolating kernel function turns to zero. Therefore only particles within a sphere with radius $2h_{smooth}$ influence particle i and are said to fall within its neighbourhood. To reduce the computational effort when calculating the properties of a particle, a sorting algorithm is used to determine which particles fall within its neighbourhood. Then, only neighbouring particles need to be considered in Equation (2.24).

According to Huertas-Ortecho [53], in the first uses of SPH, the smoothing length h was equal for all particles and held constant throughout the simulation. It was however found that a variable smoothing length for all individual particles prevented problems when the material expands and contracts. This variable smoothing distance is dependent on the local density of particles as a sufficient number of other particles is required to be present in the neighbourhood of a particle. If the smoothing length is held constant a compressed material would be much more computationally expensive as each particle has a high number of neighbours. Conversely, an expanded material would result in a lack of neighbours and may result in numerical fracture. A minimum and maximum smoothing length can be defined, which can improve computational efficiency [53].

Apart from its advantages the meshless approach also has several disadvantages. When compared to the Lagrangian method the SPH method requires a relatively high number of particles. It was identified by Ortecho [53] that this may lead to a high memory and CPU usage. This can however be mitigated to a large extend by using multiple CPU cores. Additionally, other authors contradict this statement and show a highly reduced CPU usage. Anghileri et al. [26] showed a calculation time of only 33% compared to a Lagrangian formulation while obtaining a higher accuracy. A second drawback is that no clear material boundary is present. This may pose problems in the definition of boundary conditions and the interaction between the impactor and the target [54].

The SPH method may also suffer from a phenomenon called tensile instability. This occurs when a material is loaded in tension and can cause particles to clump together [55, 56]. However, Anghileri [26] found that this does not always pose a problem. Instead, in the research of Anghileri the tension instability created a failure criterion, which seemed beneficial to the solution. The SPH model resulted in very similar scattering behaviour as seen in experimental tests.

When using the SPH approach in combination with a rounded geometry, the discretisation of a curved surface results in a flattened end, as shown in Figure 2.9. This effect is somewhat reduced by refining the mesh but will still be present. As shown by Allaeys et al. [11], this may increase the initial peak pressure and locally represent that of a flat cylinder.

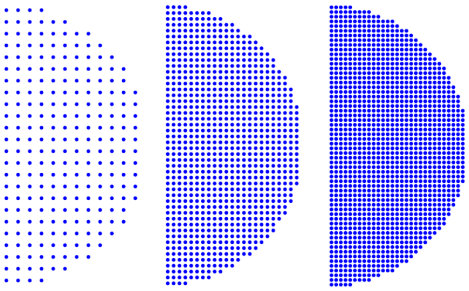

Figure 2.9: *SPH mesh refinement of rounded impactor [11].*

2.5. Bird geometry

While Section 2.4 describes the two common numerical techniques with which the bird can be modelled, it does not describe the shape in which to model the bird. To better approximate the impact effects of real birds, several studies have been performed comparing different impactor geometries. The most often used geometries are the right circular cylinder, a cylinder with hemispherical ends, an ellipsoid and a sphere, as shown in Figure 2.10 [8].

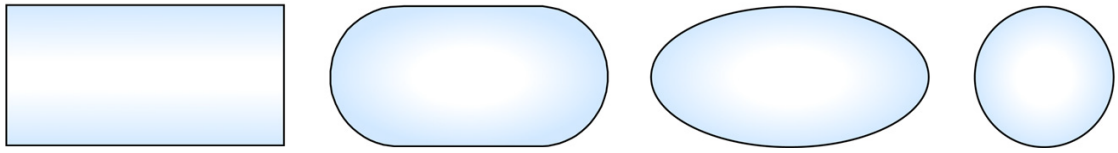

(a) *Cylinder.* ***(b)*** *Cylinder with hemispherical ends.* ***(c)*** *Ellipsoid.* ***(d)*** *Sphere.*

Figure 2.10: *Different bird model geometries [8].*

Early research by Wilbeck [9] found that the bird material starts to flow steadily after impact. Wilbeck notes that for a right circular a length over diameter ratio $L/d > 1$ is needed in order for this steady flow to develop. This suggests that the spherical model, which by definition has $L/d = 1$, has trouble developing steady flow. Wilbeck found that for flat ended cylinders the best results were obtained when using $L/d = 2$, which has since then been followed in most literature.

Airoldi and Cacchione [57] found that the peak pressure exerted by a right circular cylindrical impactor at the centre of impact corresponds reasonably well with experimental results. The cylinder however shows an overestimation of the initial peak force. This was caused by the large initial contact area compared to real birds. To improve this result, a cylindrical model with hemispherical ends was used. It was found that the force history when using this geometry showed a much better correlation with experimental results. Also, the initial peak pressure was seen to be lower when the impactor is rounded. For a cylinder with hemispherical ends Airoldi and Cacchione also found that initial peak force decreases for

increasing L/d ratios. Additionally, an aspect ratio of $L/d = 1.6$ was seen to most closely resemble experimental values of peak force, peak pressure, steady flow pressure and transferred impulse. Meguid et al. [58] showed similar correlation of increasing peak impact force with decreasing L/d while the effect of L/d on the peak pressure at the centre of impact was small.

A comparison of the damage caused on a laminated glass plate by a right circular cylinder to that created by a cylinder with a hemispherical nose was made by Mohagheghian et al. [23]. In agreement with Airoldi and Cacchione and Meguid et al. [57, 58], a lower impact force and pressure was found for the rounded impactor. This contributed to the fact that damage was initiated at lower impact velocities for the flat ended cylinder. When using a circular ended cylinder the target could sustain higher impact velocities. An additional contributing factor to this was that the duration of the shock pressure was longer in the flat ended cylinder than in the cylinder with a hemispherical front.

Meguid et al. and Mao et al. [36, 58] compared the right cylinder, hemispherical and ellipsoid model. It showed a large influence of geometry on both initial impact force and initial impact pressure, which was attributed to the difference in instantaneous contact area. This caused the right cylinder to exhibit a shock pressure 43% higher compared to the hemispherical geometry, which already showed a 30% increase over the ellipsoid model. Most literature agrees that the hemispherical model gives the most accurate impact results [21, 36, 57, 58]. Coincidentally, this is the geometry which is most commonly applied.

Some authors attempted to improve impactor geometry to a more realistic bird shape. McCallum and Constantinou [59] included actual features of the bird such as the wings, neck and head. In their research a multi-material bird model of a goose was used, where different densities were ascribed to the different sections of the bird. In addition to this, Nizampatnam [21] also used different densities for the bones and lungs. McCallum noted that for a realistic bird model impacting head first, the impact pressure is initially lower than that of a cylinder with hemispherical ends. The pressure is, however, sustained for a longer duration and increases as the torso reaches the target. Additionally, the impact of the head and neck has the effect of pre-stressing the material before impact of the torso. This may have a significant effect on damage initiation and failure of the target. Nizampatnam found a much smaller effect of the impact of the head and neck. It was mainly found that a realistic bird model showed a more detailed pressure history. Instead of only showing the Hugoniot and steady flow pressure, the realistic bird model showed pressure peaks related to individual components of the bird. As one would expect, the magnitude of these pressure peaks were shown to increase with increasing density of these components.

Instead of using a multi-material model, Hedayati [7] used one material but with a realistic bird shape. This was done by imaging a mallard in a CT-scanner and using this data to create the model, as shown in Figure 2.11. This model includes the wings, legs, neck and beak, as well as internal cavities.

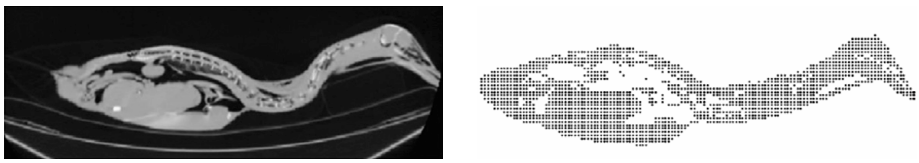

(a) *CT-scan.* ***(b)*** *Modelled approximation.*

Figure 2.11: *Creation of a realistic bird model of a mallard [7].*

The pressures produced by the realistic bird model in a tail first impact were compared to a hemispherical model, theoretical values and experimental values. It was shown that the pressure produced by the realistic bird model had a better correlation to experimental pressure values than the hemispherical model. Especially the Hugoniot pressure, which was significantly overestimated by the hemispherical model, showed an improvement. However,

compared to the theoretical values, the hemispherical ended model showed a better correlation. As it is uncertain which of these values is closest to reality, it is difficult to draw definite conclusions on this research. Additionally, Zhang [24] brings into doubt the quality of the model of Hedayati by finding much better results for a similar model with a hemispherical ended cylinder. No experimental data is ever obtained from a bird with spread wings, making it impossible to directly compare the numerical data of Hedayati with test results.

As realistic bird models increase the complexity and variability of analyses and the hemispherical model already shows good agreement with test data, the author of this report deems it unlikely that such models will be widely used.

2.6. Impact wave propagation

In any structure that is loaded, the propagation of this load through the material occurs by stress waves travelling at the local speed of sound. During quasi-static loading, the propagation of these stress waves occurs on a much smaller time scale than the loading itself. This allows one to ignore the dynamic effects of these stress waves. However, when the loading speed and the sound speed have the same order of magnitude this quasi-static assumption is no longer valid and the dynamic effects of propagating waves must be investigated [60].

There are several different wave types that propagate the loads through the structure, which each have their own characteristics and velocity. The longitudinal wave, sometimes called primary wave or P-wave, is a compression/extension pressure wave. The movement of the particles affected by a longitudinal wave occurs in the same direction as the propagation direction of the wave. The velocity of the longitudinal wave in a one-dimensional isotropic elastic medium c is determined by Equation (2.26) [60]. This wave type propagates at the highest velocity of all wave types. When talking about the wave velocity in this research the velocity of the propagating stress wave is meant and not the velocity of the moving particles in such a wave.

$$c = \sqrt{\frac{E}{\rho}} \tag{2.26}$$

In this equation E and ρ are the Young's modulus and material density, respectively.

For the analysis of a stress wave travelling in a plate, several assumptions can be made about the stress state of that plate. Giurgiutiu [61] assumes that for a plate the through the thickness stress is zero. Additionally, symmetry of shear strains is assumed. The total derivation of the equations of motion of the longitudinal waves as described by Giurgiutiu will be left out here for brevity. However, using these assumptions, the longitudinal stress wave velocity in a plate c_L is determined to be given by Equation (2.27) [61].

$$c_L = \sqrt{\frac{1}{(1-\nu^2)}\frac{E}{\rho}} \tag{2.27}$$

Here, ν is the Poisson's ratio.

A second type of plate wave is the flexural wave. In contrast to longitudinal waves, flexural waves can propagate only through structures of finite bending stiffness. Flexural waves, also called bending waves, are defined by their out-of-plane bending motion as shown in Figure 2.12.

The velocity of flexural waves c_F is derived by Giurgiutiu [61] using Kirchhoff plate theory. c_F is dependent on the plate flexural stiffness D_{flex}, as given by Equation (2.28). In this equation, h denotes the plate thickness. The flexural wave velocity c_F is given in Equation (2.29) [61], where ω is the wave angular frequency. The angular frequency is related to the ordinary frequency f by $\omega = 2\pi f$.

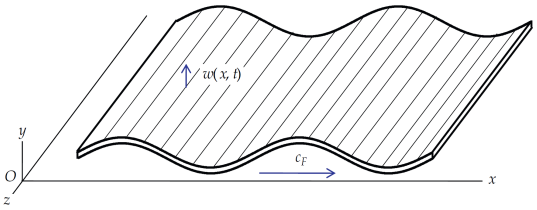

Figure 2.12: *Visualisation of a propagating flexural wave [61].*

$$D_{flex} = \frac{Eh^3}{12(1-\nu^2)} \tag{2.28}$$

$$c_F = \sqrt{\omega}\left(\frac{D_{flex}}{\rho h}\right)^{\frac{1}{4}} = \sqrt{\omega}\left(\frac{Eh^2}{12\rho(1-\nu^2)}\right)^{\frac{1}{4}} \tag{2.29}$$

As the flexural wave speed is proportional to the square root of the wave angular frequency ω, high frequency waves travel faster than those with a lower frequency. Because of this property flexural waves are called dispersive. During an impact event a large range of wave frequencies is excited. Due to their different speeds they disperse as they travel through the plate. This is illustrated in Figure 2.13 [62], which shows an excitation at the centre of a beam. It can be seen that as time passes the waves are dispersed and their shape changes.

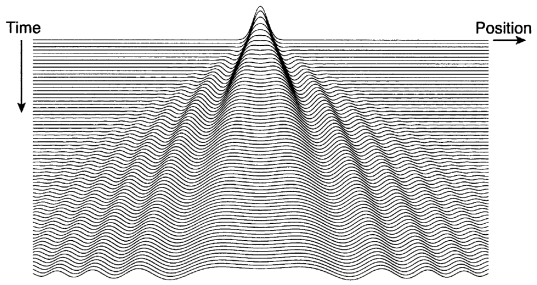

Figure 2.13: *Dispersing flexural waves changing shape in a beam excited at its centre [62].*

Another type of plate wave is the shear horizontal wave or SH-wave. In a shear horizontal wave the particle movement occurs tangentially to the wave front and perpendicular to the wave propagation direction. Its velocity c_S is given by Equation (2.30) [60], where G is the shear modulus. A special case of shear wave is the circular shear wave, which occurs when a torsional load is inflicted on a plate. This circular shear wave has the same wave speed.

$$c_S = \sqrt{\frac{E}{2\rho(1+\nu)}} = \sqrt{\frac{G}{\rho}} \tag{2.30}$$

Lastly, there is the Rayleigh wave or R-wave. This wave propagates along the surface of a solid and its particles are displaced along an elliptic path [60]. The Rayleigh wave velocity c_R is slightly lower than that of the shear-horizontal wave and is approximated by Equation (2.31) [61].

$$c_R = c_S\left(\frac{0.87 + 1.12\nu}{1+\nu}\right) \tag{2.31}$$

These longitudinal, shear-horizontal and Rayleigh waves can be seen in Figure 2.14 [15], which shows the wave propagation within a plate experiencing a loading perpendicular to the surface. For the longitudinal and shear-horizontal wave the particle motion is given by the double-sided arrows.

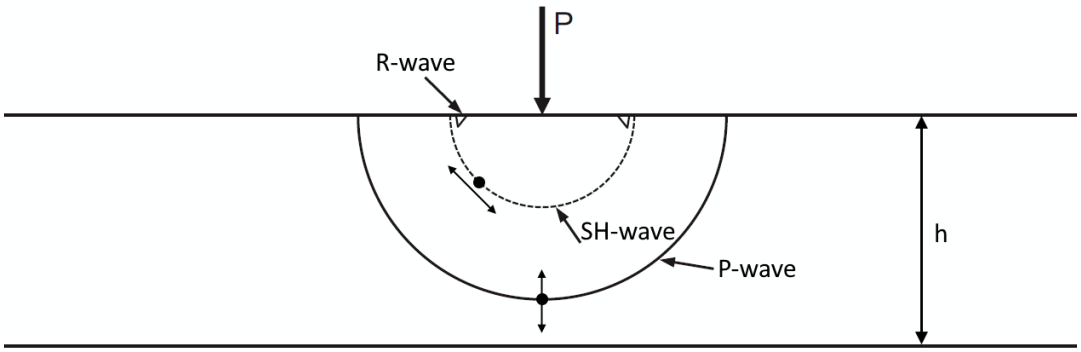

Figure 2.14: *Primary, shear-horizontal and Rayleigh wave in a solid after impact load P [15].*

An overview of the wave velocities of the different wave types is shown in Table 2.1. The wave velocities shown are those for an aerospace grade aluminium alloy.

Table 2.1: *Speeds of different types of stress waves for an aerospace grade aluminium alloy plate with h=3mm, ρ=2.78E-9 tonne/mm^3, ν=0.3 and E=74660 MPa.*

Wave type	Wave speed (km/s)
c_L	5.43
c_S	3.21
c_R	2.98
$c_F(f = 1\ kHz)$	0.099
$c_F(f = 10\ kHz)$	0.31
$c_F(f = 100\ kHz)$	0.99
$c_F(f = 1000\ kHz)$	3.14

3

Bird impact tests

To be able to answer the research questions about the capabilities of current modelling techniques for wave propagation analysis, a test campaign was performed. The goal of these tests was to measure how a bird impact affects a dummy system that is attached to the structure close to the impact zone. All the tests described in this chapter were already performed before the author of this thesis joined Airbus. Therefore, the author could not influence any aspect of the testing method or the data collected. Thus, the following description of the test setup is based on the reporting and imagery that was made available to the author.

Instead of a real aircraft component, custom-built plate structures were used to minimise the influence of complexities, while still being representative of an aircraft structure. The layout of the tests is described in Section 3.1. Two different types of structure were used for the tests, a flat plate and a stiffened plate. These structures are presented in Section 3.2 and Section 3.3, respectively. Several types of measurement equipment were used in these tests. This equipment is described in Section 3.4.

3.1. Test layout and specifications

The test plates were mounted onto a test rig, as shown in Figure 3.1. A pressurised air cannon, shown in Figure 3.2, was used to accelerate the bird to its impact velocity. During all tests the impact was perpendicular to the test subject. Four high-speed video cameras were used to capture the impact event. Camera 1 and 2, shown in Figure 3.1, were used for the digital image correlation measurement, about which more will be explained in Section 3.4. Camera 3 was used to determine the impact velocity and camera 4 provided an overview of the impact event.

The weight of the test birds was, approximately, 1.8 kg (4 lbs), which is based on the regulatory requirements described in Section 1.1. The targeted impact velocity V_{imp} for all tests was 120 m/s. Due to small inconsistencies in the tests, slight variances were noted. The measured impact velocity and weight of the bird are shown in Table 3.1. To limit the aerodynamic forces, which can alter the impact speed and location, the wings of the bird were bound onto its body to keep them from opening.

Table 3.1: *Bird mass, impact velocity and mass of the dummy mass, for the five bird impact tests.*

	Flat plate			Stiffened panel	
	Test 1	Test 2	Test 3	Test 4	Test5
Bird Mass [g]	1821	1820	1824	1815	1818
Bird impact velocity [m/s]	123.8	106.1	124.9	120.1	122.1
Dummy mass [kg]	2.5	5.0	7.5	2.0	2.0

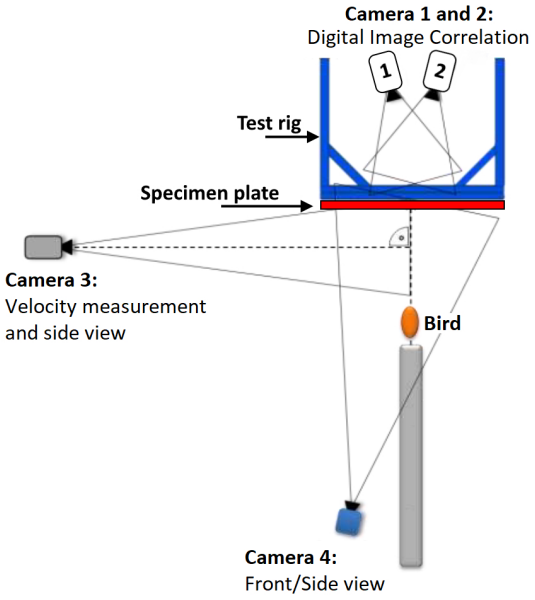

Figure 3.1: *Diagram of the test layout.*

Figure 3.2: *Images of the pressurised air cannon at IABG in Lichtenau.*

3.2. Flat plate

The flat plate test structure is the most simple of the two plate structures. It consists of an aluminium alloy sheet metal plate, which is mounted onto a test rig using bolts with washers. This is shown in Figures 3.3a and 3.3b. The width, height and thickness of the plate are 2.0 m x 1.2 m x 3.0 mm, respectively. The plate is made out of an aerospace grade aluminium alloy.

In the flat plate tests the centre of the plate was targeted as indicated by the red spot in the diagram. At the bottom of Figure 3.4 the impact location and direction are indicated by the red arrow at the centre of the plate.

To represent an (electrical) system subjected to shock as described in Chapter 1, a solid aluminium alloy block was attached as a dummy mass to the back of the plate. This dummy mass is located 0.5 m from the side of the plate and centred in vertical direction. This is shown in Figure 3.4. Three tests were performed using flat plates, each of which using a different size dummy mass, as shown in Table 3.1. The dummy mass was attached using four aluminium alloy L-brackets, shown in Figure 3.5. These were connected to both the plate and the dummy mass using steel bolts. Since the flat plates were significantly plastically deformed during the tests, each test used a new flat plate.

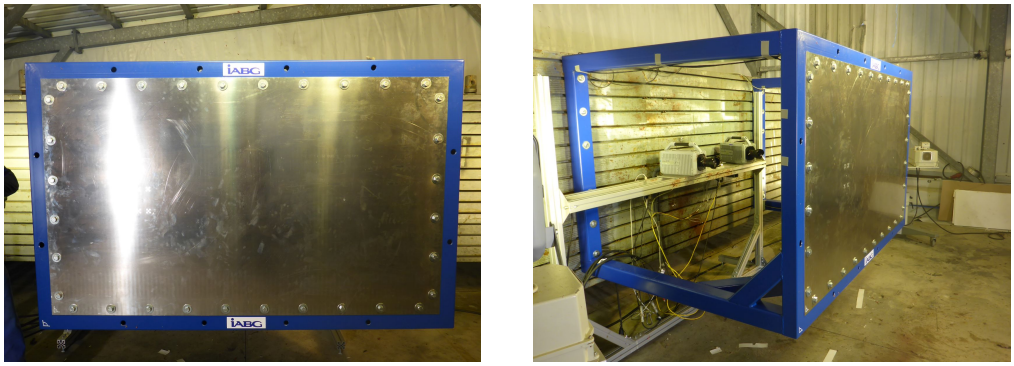

(a) *Front view.* ***(b)*** *Side view.*

Figure 3.3: *Images of the flat plate mounted to the test rig.*

In the first flat plate test, with a dummy mass of 2.5 kg, five accelerometers were attached to the structure. The location of these accelerometers is given in Figure 3.4. These accelerometers were attached to the structure using bolts. Accelerometer 2 is bolted on top of the dummy mass while the other accelerometers are mounted to the plate. All the accelerometers are positioned such that they measure the accelerations in x-direction, parallel to the flight path of the bird.

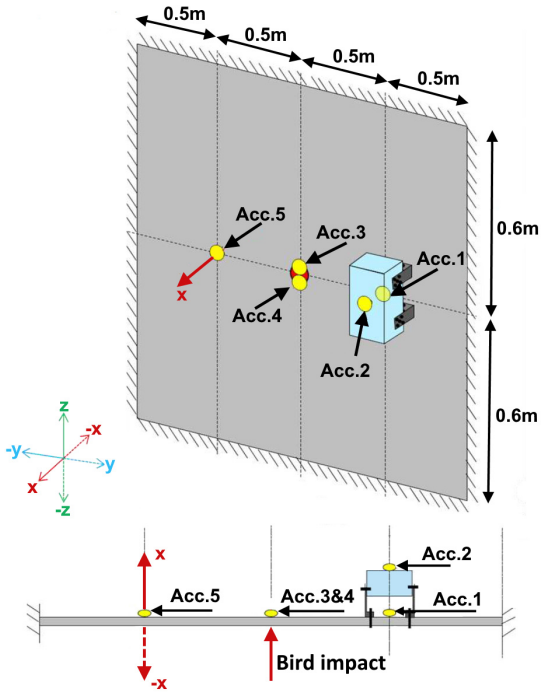

Figure 3.4: *Diagram of the flat plate test layout.*

During the first bird impact test of the flat plate a problem occurred. In test 1 the fasteners used to mount accelerometer 3 and 4, at the centre of the plate, created a stress concentration. This caused the plate to rupture upon impact of the bird, invalidating most results of test 1. To prevent this for further tests, the accelerometers 3 and 4 were not installed, leaving only accelerometers 1, 2 and 5 for the 2nd and 3rd test.

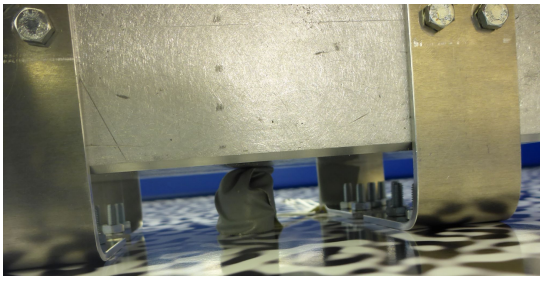

Figure 3.5: *Use of L-brackets to connect the dummy mass to the plate.*

3.3. Stiffened plate

The stiffened plate structure more closely resembles an aircraft structure than the flat plate. However, this also results in added complexities. To limit the production and modelling complexities, both the front surface of the panel as well as the stiffeners were machined out of one solid block of aerospace grade aluminium alloy. This removed the need to join the stiffeners and plate together. As a result of this machining, fillets are present at the connecting surfaces of the stiffeners and the plate as well as in between the stiffeners themselves. The spacing of these stiffeners has been dimensioned in a similar way as one would find on the overhead cockpit area of an A320 sized aircraft.

The stiffened plate tests are performed using the same test rig as the flat plate tests. The stiffened plate is bolted onto the test rig using the stiffeners along its outer border. This means that the bolting directions are perpendicular to the impact direction (i.e. in y-, and z-directions). As this could not be done directly onto the test rig, a 'converter' section is used as indicated using the arrow in Figure 3.6a. The section connects the stiffened panel to the rest of the test rig.

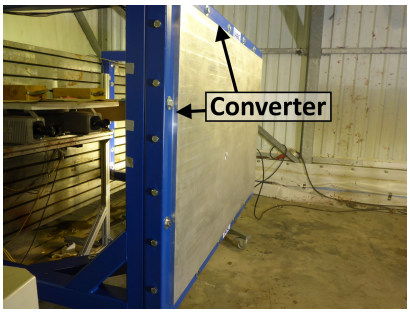

(a) *Front of the panel.*

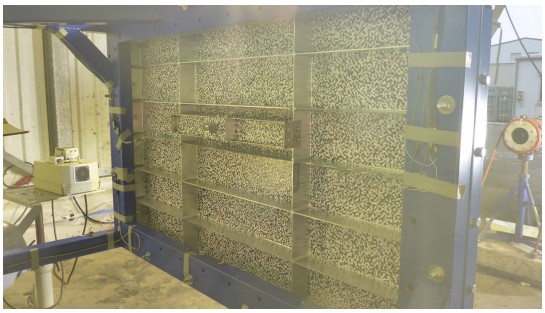

(b) *Backside of the panel.*

Figure 3.6: *Images of the stiffened panel mounted to the test rig.*

As can be seen in Figure 3.6b, a 2.0 kg aluminium alloy block is attached to the structure. Similarly to the flat plate tests, this block acts as a dummy mass, which represents a system mounted to the aircraft structure. Resembling a real aircraft system, this dummy mass is not mounted directly to the panel but is instead connected using a 'mounting profile'. This profile consists of a C-beam and is attached to the stiffeners using two bolts at each side. The dummy mass is attached at the centre of the mounting profile using three bolts, which all run the full length through the dummy mass. This is shown in Figure 3.7. The position of the mounting profile with respect to the stiffened plate is shown in Figure 3.8.

Two tests were performed using the stiffened panel. These were test 4 and test 5, as were shown in Table 3.1. The only difference between these two tests was the location in which the bird impacted. In test 4, the bird targeted a 'pocket' in between the stiffeners, while an intersection point of stiffeners was impacted in test 5. These locations are marked in Figure 3.8. To save cost both tests were performed on the same panel, where only the mounting profile

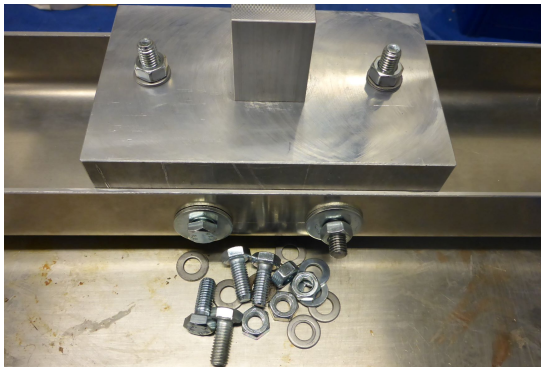

Figure 3.7: *Attachment of the dummy mass to the mounting profile.*

was replaced. Therefore, test 5 was performed with a stiffened panel, which was already dented at the impact location of test 4.

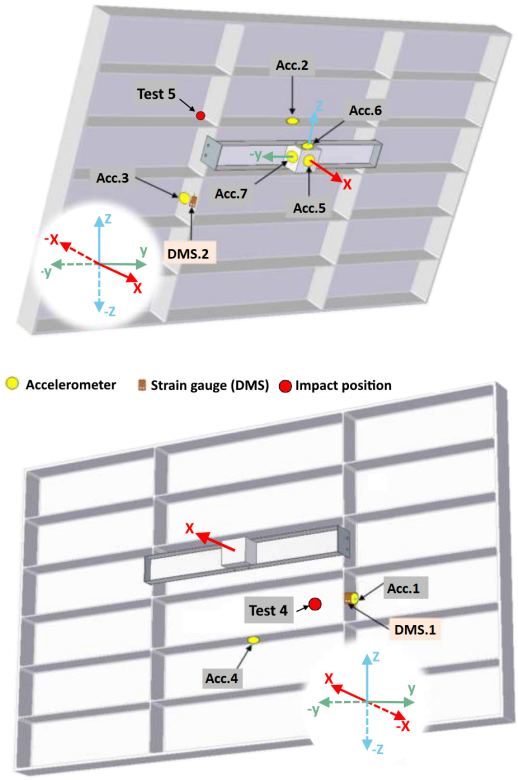

Figure 3.8: *Diagram of the stiffened panel test layout.*

Figure 3.8 also shows the locations of the accelerometers, denoted with 'Acc'. Additionally, two strain gauges were attached to the stiffened plate. Their locations are denoted as 'DMS' in Figure 3.8. Accelerometers 1-4 were mounted onto the stiffeners of the panel. Using an aluminium alloy cube, the accelerometers were positioned such that their measurement direction is parallel to the x-axis, as seen in Figure 3.9. These accelerometers were positioned in the centre of their respective stiffeners. The strain gauges were placed about 10 mm from the edge of the stiffeners. Their measurement direction is parallel to the z-axis.

Accelerometers 5-7, which measure the accelerations of the dummy mass, are not attached directly to the dummy mass but to a cuboid on top of this mass as can be seen in Figure 3.9b.

(a) *Strain gauges and accelerometers 1-4.*

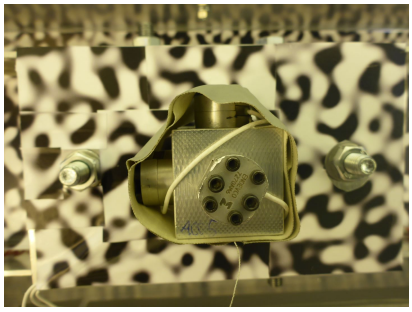

(b) *Accelerometers 5-7 on the dummy mass.*

Figure 3.9: *Attachment of sensors to the stiffened plate.*

The accelerometers are mounted on the sides of this cuboid such that they can measure accelerations in x-, y-, and z-directions.

Several problems occured during the stiffened plate tests. During test 4, the first stiffened plate test, strain gauge 1 and accelerometer 5 were destroyed. This was not noticed during the test day and thus they were not replaced. Therefore, data of these sensors was available for neither test 4 nor test 5. Additionally, accelerometer 4 broke during test 5. This combination of failures significantly reduces the available data.

3.4. Measurement techniques

Several techniques were used to collect data during the tests. These consist of the accelerometers and strain gauges described above. Thirdly, digital image correlation (DIC) was used for all tests. Additionally, slow motion video footage was captured to give qualitative information about the tests. After the tests were performed the panels were also visually inspected to determine any deformation and other damage.

The accelerometers used were Endevco 7270A-60KM6. These recorded the accelerations at a frequency of 100 kHz with a linear range of 60 000 g [63] and a sensitivity of approximately 50 m/s^2.

The strain gauges used were of the type HBM 1-LY13-6/350. The length of the measurement grid of these strain gauges is 6.0 mm in measurement direction with a width of 2.8 mm [64].

The cameras used for the digital image correlation were of the type Photron SA-X2. These cameras recorded in black and white at a frame rate of 20 000 fps and a resolution of 1024x672 pixels. The DIC output data divides the structure up into a grid. An example of a frame of such DIC data is shown in Figure 3.10a. In this image the DIC data output is overlaid onto video footage of the back of the plate, which was taken with one of the DIC cameras. It is seen that at some locations, mainly at the edges of the plate and near the dummy mass, no data is available. This can occur when the view of either one of the DIC cameras is obstructed. Figure 3.10b shows an impression of the vertical spacing of the data grid. It can be seen that the data grid does not align perfectly with the plate. This results in a slight variation in spatial resolution at different locations of the plate. On the left side of the image (negative y-direction) the distance from top to bottom is represented by more rows than on the right side of the image (positive y-direction). This leads to a variation in resolution of approximately 28 to 35 mm. Additionally, due to this misalignment, a horizontal line in the data grid might in reality slope upwards or downwards when it is located away from the centre of the plate.

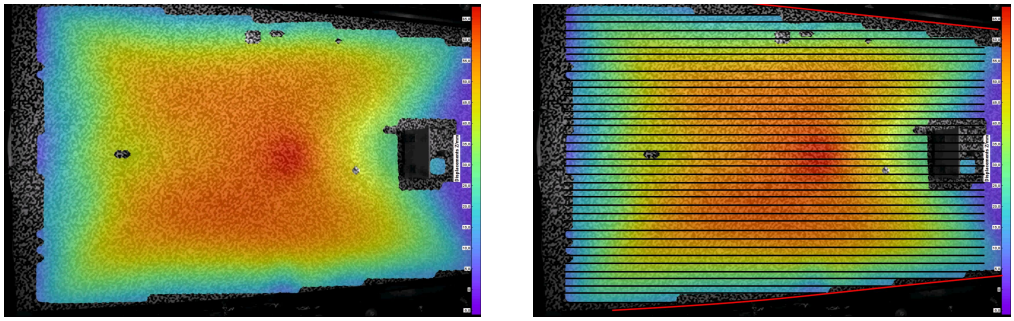

(a) *Frame of DIC data.* ***(b)*** *Data grid lines.*

Figure 3.10: *Frame of the digital image correlation data, overlayed on the structure backside.*

4

Numerical models

The test setups described in Chapter 3 were recreated as numerical models by the author of this thesis. In the creation of these models, advice from Airbus experts and standard practices were taken into account.

First, some general modelling choices are discussed in Section 4.1. In Section 4.2 and Section 4.3 the modelling aspects that are specific to the flat plate model and stiffened plate model respectively are given. The model of the test rig is described in Section 4.4 and the bird models are described in Section 4.5. The definition of contact and the material laws are described in Section 4.6 and Section 4.7, respectively. Section 4.8 describes the modelling of the fasteners. To investigate the sensitivity of the model to some alternative modelling choices, several variations to the model were made. These variations are described in Section 4.9. Finally, a simple model of a large square plate is described in Section 4.10. This model was not based on any physical tests. Instead, it will be used to identify the accuracy of the stress wave velocities in the model, without the interference of the complexities of plates from the physical tests.

4.1. General modelling choices

In this section, the modelling choices will be described that apply to both the flat and stiffened plate models. These models represent some of the state-of-the-art modelling techniques currently used in industry. The modelling choices described here apply to what will from here on be called the 'base' model. Variations to this base model are described in Section 4.9. These model variations will be used to investigate the sensitivity of the model to these changes and will always be compared to the base model.

In this research, commercial software was used for the creation of the numerical model and its analysis. The finite element models were created using *Hypermesh 2017.2.4* and the analysis was performed using *Abaqus v6.13-2* on the high powered computing platform available at Airbus Operations.

In the base model, all thin-walled components were modelled using 4-node reduced integration shell elements (S4R). For other structural components, 8-node linear brick, reduced integration elements (C3D8R) were used. An element size of 5 mm was chosen, although at certain locations this varies to accommodate the local geometry.

In Table 4.1, the nodal degrees of freedom (DOFs), number of integration points and, for shell elements, the number of section points are given. Additionally, it is shown which stress directions are represented in each element type. The 1 and 2 directions indicate the directions in the element plane. In addition to the S4R and C3D8R elements used in the base model, the elements used to investigate the influence of implementing different element types are also included in the table.

Table 4.1: *Properties of different element types in Abaqus.*

	Nodes	DOFs	Int. points	Sec. points	Stresses
S4R	4	1,2,3,4,5,6	1	5	S11,S22,S12
C3D8R	8	1,2,3	1	-	S11,S22,S12, S33, S13, S23
SC8R	8	1,2,3	1	5	S11,S22,S12
C3D8	8	1,2,3	8	-	S11,S22,S12, S33, S13, S23
C3D6	6	1,2,3	1	-	S11,S22,S12, S33, S13, S23
C3D4	4	1,2,3	1	-	S11,S22,S12, S33, S13, S23

4.2. Flat plate

This section gives more details that specifically describe the flat plate model. An overview of the flat plate model is given in Figure 4.1.

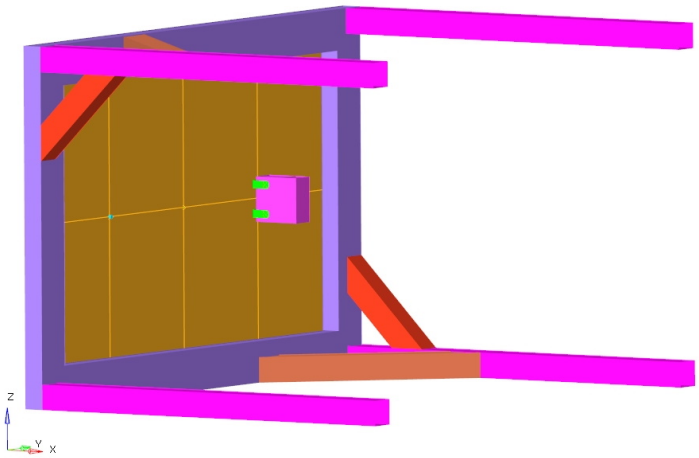

Figure 4.1: *Overview of the back side of the flat plate FE model.*

One point of interest in the flat plate tests is the connection between the dummy mass and the plate. A detailed view of this is shown in Figure 4.2. It can be seen how the mass is attached to the plate using L-brackets. These L-brackets are bolted to both the dummy mass and the plate as described in Section 3.2. The CONN3D2 connector elements, which represent the bolts, run from the centreline of the plate to the centreline of the brackets. They can be seen in Figure 4.2b. How the fastener behaviour is defined is described in Section 4.8.

In early versions of the model, the connection in between the plate and the L-bracket was the only part of the bolt that was modelled. However, it was found that, after impact of the bird, the plate starts to displace in the x-direction at the point of impact. This displacement propagates outward from the impact point. When this displacement reaches the dummy mass, the plate is pressed towards the dummy mass. This caused the L-brackets to collapse to such an extent, that the dummy mass would impact the plate. This would lead to large strains at the bent section of the L-bracket, causing several elements to be deleted. This was in stark contrast to the L-brackets in the physical impact tests, where only a limited amount of plastic deformation could be seen.

The behaviour of the dummy mass could not be clearly seen on the video footage of the bird impact tests. Therefore, for some time, it was unclear what had caused this failure of the L-brackets in the numerical model. Several solutions to improve the model were investigated, but after multiple iterations, the length of the 'bolt endings' sticking out was noticed, as was shown in Figure 3.5.

As these bolts may contact the dummy mass in case of severe displacements, it was deemed necessary to model them. These bolt endings are shown in dark blue and yellow in Figure 4.2.

They are attached to the bracket surface using a tie constraint, where the bolt surface is defined as the slave surface. As the exact length of the bolts was not known, an estimation was made based on available photographs. After including these bolt endings, the movement of the dummy mass represented the video footage of the impact tests much more closely. Also, the problem of damage to the L-brackets was resolved.

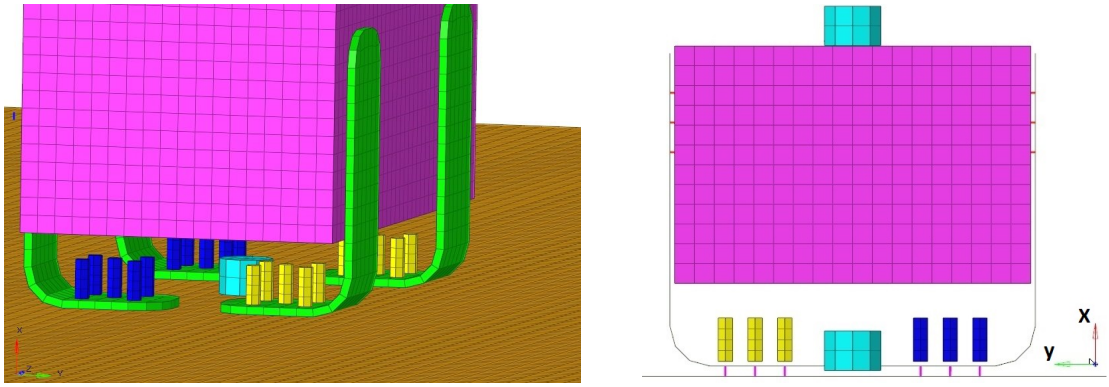

(a) *Three dimensional view of the 5.0 kg dummy mass.* ***(b)*** *Side view of the 2.5 kg dummy mass.*

Figure 4.2: *Detailed views of the dummy mass.*

Two other components, seen in Figure 4.2, are accelerometers 1 and 2, which are attached centrally underneath and on top of the dummy mass, respectively. Similarly to the bolt endings, they are attached to the structure using a tie constraint and their surface is used as the slave surface. A node at the centre of the modelled accelerometer is used to output the acceleration data. All of these accelerometers measure the acceleration in x-direction. To be consistent with the measurements from the bird impact tests, the accelerations are recorded with a sample rate of 100 kHz.

To distribute the load of the bolts that connect the flat plate to the test rig, washers are used in the impact tests. This was shown in Figure 3.3. These bolts were preloaded and tightly clamped the plate in between the washers and the test rig. With the fastener modelling approach described in Section 4.8 this effect is however not seen, as the number of nodes influenced by the fastener connection is limited to those within the radius of influence of the connector element. Additionally, there is no preload present in these connectors as this option is not available in Abaqus/Explicit. Therefore, to approach this clamping effect, a kinematic coupling constraint is applied to all the nodes underneath the washers. This causes these nodes to follow the same rigid body motion as the connecting node of the connector element [25].

4.3. Stiffened plate

This section explores some of the modelling aspects of the stiffened plate. An overview of this plate and its attachment to the test rig is given in Figure 4.3. In this image, the birds of test 4 & 5 are shown just before their impact with the plate.

In the stiffened panel tests, two strain gauges were used. These were modelled by using a 2-node linear 3D truss element (T3D2). These elements were attached to the surface of the structure using a tie constraint. As these strain gauges are very thin they provide a negligible stiffness to the structure. Therefore an artificially low Young's modulus was used to define this element. The element is therefore only used to output the strain measurement at the correct location and has a negligible effect on the simulation. The use of such a strain gauge element is shown in Figure 4.4a.

The dummy mass in the stiffened panel tests is connected to the structure via a mounting profile. This mounting profile is seen in green in Figure 4.4b and is made out of conventional shell elements. The dummy mass is placed inside this profile and small connector elements

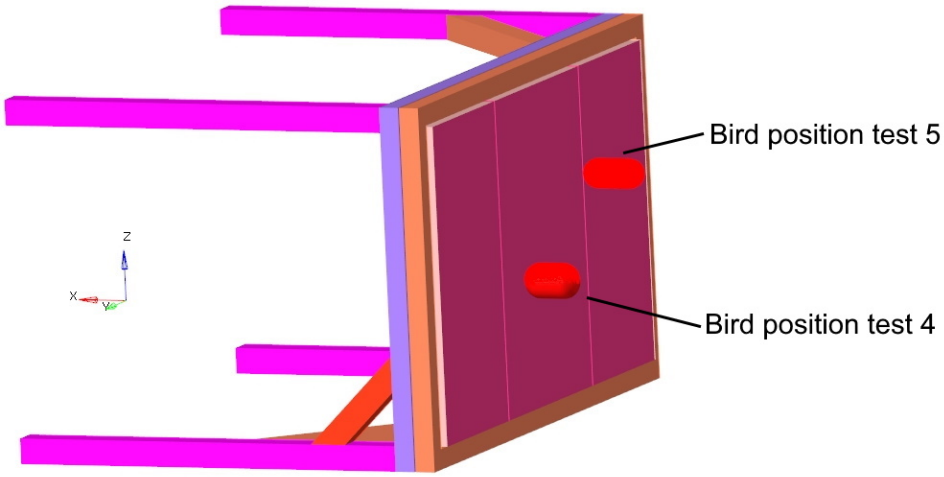

Figure 4.3: *Overview of the front of the stiffened plate FE model and the position of the bird just before impact.*

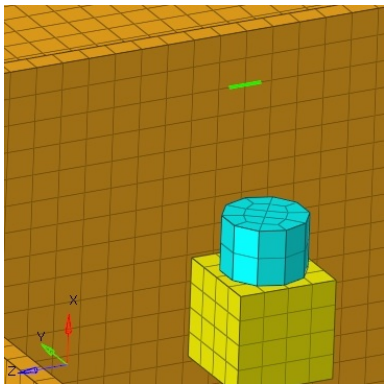

(a) *Attachment of accelerometer (blue) and strain gauge (green stripe).*

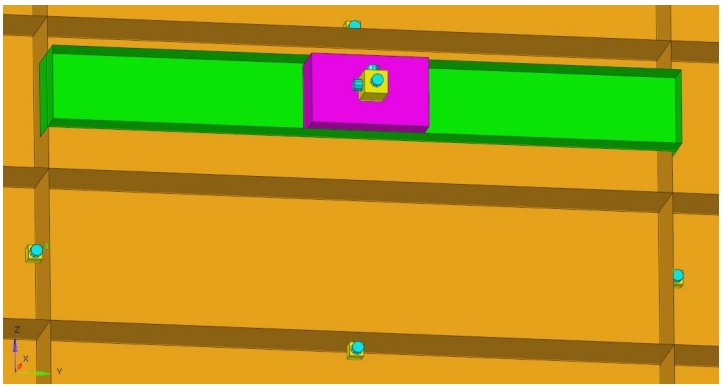

(b) *Attachment of the dummy mass and sensors.*

Figure 4.4: *Detailed views of the stiffened plate model.*

(CONN3D2) attach the surface of the dummy mass to the mounting profile, as shown in Figure 4.5. This is a simplification as in reality long bolts pass from one side of the dummy mass to the other through holes drilled into the aluminium alloy.

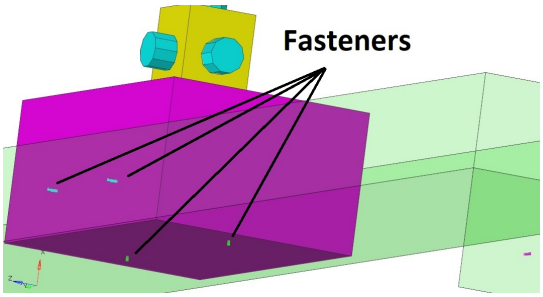

Figure 4.5: *Connection of the dummy mass to the stiffened plate.*

4.4. Modelling of the test rig

In the early model of the flat plate test the test rig was not yet included in the model. Instead, only the front surface of the test rig, where the plate and test rig come into contact, was included. All six DOFs of this front surface were restricted. The reasoning to set this as the

system boundary was that the test rig was made out of thick steel beams, which were deemed unlikely to deform to a significant extent.

This assumption turned out to be false. It was seen that without the inclusion of the test rig, the displacement of the plate at the centre of impact was too small compared to the test results. As the omission of the test rig was one of the first things identified as a potential cause, the model was expanded to include the test rig.

The model of the test rig was used in both the stiffened plate and flat plate models. The test rig and the FE model of the rig are displayed in Figures 4.6a and 4.6b, respectively. As the test rig consists of thin-walled beams it was chosen to model the rig using shell elements. While the wall thickness and cross-section of the beams were known, the exact length of the cross-beams was not. Therefore, photographs were used to estimate their length and the position at which they are interconnected. An example of the simplified modelling of the beams can be seen in Figure 4.6c. For simplification, the rounded corners were assumed to be right-angled, as is shown in the element representation. An exception to this is the corner at the inside of the front of the rig (upper-right). This is the corner that comes into contact with the plate. In this case, the rounding of the corner was implemented to correctly represent the contact between the plate and the test rig.

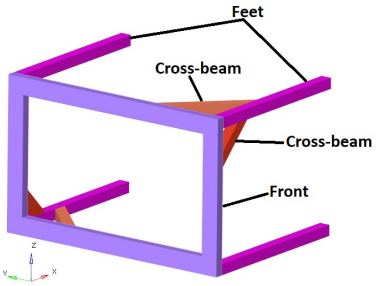

(a) *Image of the test rig model.*

(b) *Photo of the test rig.*

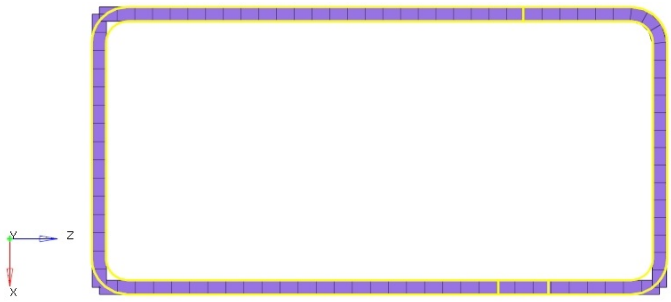

(c) *Cross-section of the test rig front beams. The actual shape is given in yellow while the FE representation is given by the purple elements.*

Figure 4.6: *Multiple representations of the test rig.*

In Figure 4.6, it can also be seen that the rig model ends at the end of the feet. The beam that is bolted to the test stand, seen in Figure 4.6b, is not included. It was thought that this point was far enough from the impact location such that this could be used as the model boundary. As a boundary condition, the nodes along the end of the feet were fixed in all degrees of freedom (DOFs).

As the test rig is made of relatively thick steel beams, which are not directly impacted, it was assumed that the rig did not undergo any plastification. Therefore, only an elastic material description was used, where a Young's modulus $E = 210$ GPa, a Poisson's ratio $\nu = 0.3$ and a density $\rho = 7850$ kg/m^3 was used.

4.5. Bird model

In addition to the structure, the bird also needed to be modelled. The bird models have a weight of 1.814 kg and a length to diameter ratio of $L/d = 1.8$. For each test it was checked whether this ratio was reasonable compared to the bird used by evaluating the video footage taken by camera 3 (see Figure 3.1). In test 1-4 no significant deviation was seen. In test 5 the bird was seen to be more slender. To adjust for this discrepancy, a more slender bird model with a ratio $L/d = 2.2$ was used. The same video footage was used to evaluate whether any rotation of the bird took place during the tests. This, however, did not appear to be the case. Therefore, rotation was not included in the model for any of the tests.

As described in Section 2.4, there are currently two types of bird models that are most commonly used; the Lagrangian and Smoothed Particle Hydrodynamic (SPH) bird models [8]. In this research, both of these models have been evaluated and are shown in Figure 4.7. For the base model, the SPH bird was used. Both models use a tabular equation of state, defined using Equation (2.18) with $f_2(\epsilon_{vol})$=0. Both the Lagrangian and SPH models use a tensile failure criterion to allow for bird flow. For the SPH model a variable smoothing length was used.

$$p = f_1(\epsilon_{vol}) + \rho_{ref} f_2(\epsilon_{vol}) E_m \qquad \text{(2.18 revisited)}$$

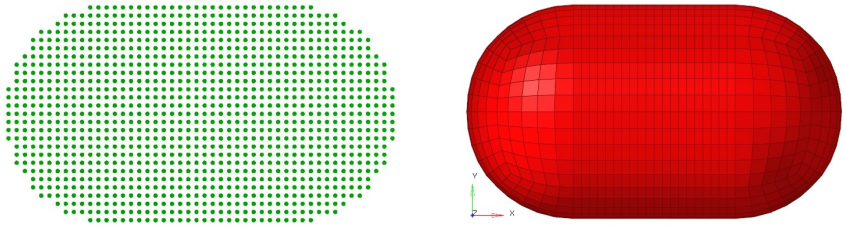

(a) *SPH bird model.* ***(b)*** *Lagrangian bird model.*

Figure 4.7: *Numerical bird models, with a mass of 1.814 kg and* L/d = 1.8.

4.6. Contact

During the bird impact tests many objects come into contact with each other. This is not just limited to the contact between the bird and the plate. Other interacting parts include the plate and test rig, the dummy mass and mounting brackets and the plate and mounting brackets. For such a situation, where many objects interact, Abaqus provides a simple general contact definition using the keyword *CONTACT. With this keyword, contact interactions between multiple surfaces can be defined. Additionally, self-contact can be defined for a surface. Self-contact prevents two sections of the same surface from penetrating each other. This was used in the contact definition between different parts of the structure. One single surface was defined, which includes all the exterior surfaces of all the components of the structure. By defining self-contact for this single surface, all the contact interactions between structural components are defined.

It was found that for shell elements Abaqus/Explicit automatically adjusts the contact thickness used in the contact algorithm. This can lead to nonphysical penetration behaviour. This was prevented by specifying these surfaces in the keyword *CONTACT EXCLUSIONS and using the contact controls *CONTACT CONTROLS ASSIGNMENT, CONTACT THICKNESS REDUCTION = NOPERIMSELF. This prevents Abaqus from adjusting the element contact thickness.

To determine the contact loads the penalty method is used. The general contact definition does not require the user to define a slave and master surface. Instead, a balanced master-slave definition is used. In this definition, first, one of the surfaces in contact is treated as the master surface and the nodal contact loads are determined. Secondly, the other surface

is used as a master surface and the nodal loads are determined. The actual contact loads are then determined by taking the average of both situations [25]. Friction is not considered in the numerical model.

In the case of contact between the SPH bird and the structure, the SPH bird is always considered to be the slave surface. This is caused by the fact that the SPH particles can only be described as a nodal surface, which can never be a master surface. For the Lagrangian bird model, a balanced contact algorithm can be used. To account for element erosion of the outer surface of the bird, the internal element surfaces of the bird were also included in the contact algorithm.

4.7. Material laws

To describe the behaviour of all the components in the model, material laws are needed. While the test rig is only modelled using the elastic material behaviour of steel, this is not sufficient for most other components. Therefore, for all aluminium alloy components, an elastic-plastic material law was used with isotropic hardening.

A tabulated definition is used for the metal plasticity. In this method a table is provided, giving yield stress values as a function of plastic strain. The yield stress for plastic strain values in-between those defined is then found by linear interpolation [25]. Only isotropic hardening is used and kinematic hardening is ignored. The yield criterion used is the von Mises stress criterion, as was given in Equation (2.19).

$$\sigma_{vm} = \frac{1}{\sqrt{2}}\sqrt{(\sigma_1 - \sigma_2)^2 + (\sigma_2 - \sigma_3)^2 + (\sigma_3 - \sigma_1)^2} \qquad \text{(2.19 revisited)}$$

In addition to plasticity, certain parts of the structure may also experience material failure. This is incorporated through a damage variable D, which lowers the stress according to Equation (4.1) and is graphically represented in Figure 4.8.

$$\sigma = (1 - D)\bar{\sigma} \qquad (4.1)$$

Here σ is the stress tensor of an element and $\bar{\sigma}$ is the stress tensor of the element if it were undamaged. The magnitude of the damage variable D is defined as a function of the plastic displacement $\bar{u}^{pl}$ of an element. This relation is defined through a tabular input. Once the damage variable D reaches 1, the element is deleted. In Figure 4.8, σ_0 is the yield stress at zero plastic strain. σ_{y0} and $\bar{\epsilon}_0^{pl}$ are the yield stress and equivalent plastic strain at damage initiation. The plastic strain at failure (D≥1) is given by $\bar{\epsilon}_f^{pl}$.

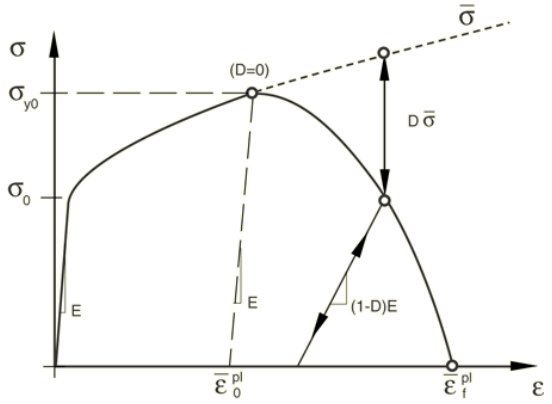

Figure 4.8: *Representation of the aluminium alloy material model used [25].*

As the damage variable is a function of plastic displacement instead of strain, the relation $D(\bar{u}^{pl})$ is only suited to a specific element size. When the same relation is used for an element

of much smaller size than that for which it was intended, $\bar{u}^{pl}$ will remain low even when the plastic strain is high. This results in the element retaining an artificially low damage variable and, thus, a postponed stiffness degradation and failure. Therefore it is important to keep a consistent element size for all elements that use the same material model.

As was described in Section 2.3, aluminium alloys often show strain rate hardening when experiencing high strain rates. This behaviour is neglected in the base model. However, literature is ambiguous on whether to include strain rate hardening in bird impact models.

To investigate the effect of strain rate hardening, this hardening behaviour is included in a second version of the material model. For this, use was made of the Johnson-Cook strain hardening equation given in Equation (4.2) [25, 41]. This is a simplified version of Equation (2.22), such that temperature softening is neglected. This equation describes the yield stress σ_y as a function of several parameters. The first term of this equation gives the strain hardening effect. The second term describes the strain rate hardening effect.

$$\sigma_y = [\sigma_0 + B(\bar{\epsilon}^{pl})^n][1 + C_{JC} \ln \dot{\epsilon}^*] \tag{4.2}$$

In this equation, σ_0 is the yield stress when no plastic strain is present and $\bar{\epsilon}^{pl}$ is the equivalent plastic strain. B and n are the strain hardening coefficient and the strain hardening exponent, respectively. $\dot{\epsilon}^* = \dot{\bar{\epsilon}}^{pl}/\dot{\epsilon}_0$ is a dimensionless plastic strain rate, where $\dot{\bar{\epsilon}}^{pl}$ is the equivalent plastic strain rate and $\dot{\epsilon_0}$ is a user-defined reference strain rate often taken as $\dot{\epsilon_0} = 1\ \mathrm{s}^{-1}$. Parameter C_{JC} is the Johnson and Cook strain rate coefficient.

A separate expression was stated by Johnson and Cook to describe the failure strain of a material. The Johnson-Cook failure equation shown in Equation (4.3) [25, 38] describes the equivalent plastic strain at failure $\bar{\epsilon}_f^{pl}$ as a function of damage parameters D_1-D_5.

$$\bar{\epsilon}_f^{pl} = [D_1 + D_2 \exp(D_3\eta)]\,[1 + D_4 \ln \dot{\epsilon}^*]\,[1 + D_5 T^*] \tag{4.3}$$

Here T^* is the nondimensional (homologous) temperature and η is the stress triaxiality, which is the ratio of pressure p and effective stress q shown in Equation (4.4).

$$\eta = \frac{p}{q} \tag{4.4}$$

The damage variable D, as used in Equation (4.1), is given by Equation (4.5), where $\Delta\bar{\epsilon}^{pl}$ is the increment of the equivalent plastic strain.

$$D = \sum \frac{\Delta\bar{\epsilon}^{pl}}{\bar{\epsilon}_f^{pl}} \tag{4.5}$$

The strain rate effects are only considered for the flat plate. The values of the coefficients in Equations (4.2) and (4.3) for the aerospace grade aluminium alloy used are given in Table 4.2. They were researched by Kay [38], who validated them by comparing the results of an impact test with a numerical model. In this impact test, a fragment of a fan blade impacted an aluminium alloy sheet. As damage constant D_5=0, the last term in Equation (4.3) eliminates and thus temperature effects do not play a role.

Table 4.2: *Constants of the Johnson-Cook material model for an aerospace grade aluminium alloy [38].*

σ_0 [MPa]	B [MPa]	n	C_{JC}	$\dot{\epsilon}_0$ [s^{-1}]	D_1	D_2	D_3	D_4	D_5
369	684	0.73	0.0083	1.0	0.112	0.123	1.5	0.007	0

The effect of strain rate hardening described by Equation (4.2) is shown in Figure 4.9. These curves were created using the values from Table 4.2.

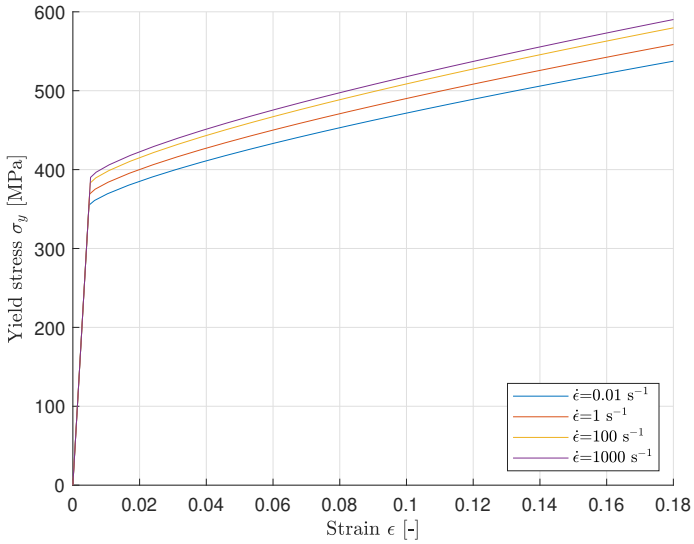

Figure 4.9: *Strain rate hardening of aerospace grade aluminium alloy, determined using the material properties given in Table 4.2.*

4.8. Fasteners

In the physical test setup, bolts were used in several locations to connect different parts of the structure. These bolts are represented by three-dimensional, 2-node connector elements (CONN3D2). These elements can transfer loads in all six DOFs [25].Using the *FASTENER keyword, these elements can be used in a mesh-independent way. The advantage of this is that the fasteners (bolts) can be positioned at their exact physical location without disturbing the mesh of the connecting surfaces.

The radius of influence of the fasteners can be defined using the keyword *FASTENER PROPERTY. This radius determines which nodes on the connecting surfaces are coupled to the fastener element node, as shown in Figure 4.10. The connecting point in such a coupling definition is forced to undergo the average rotation and displacement of the nodes in its radius of influence [25]. The radius of influence that was used, was determined by the radius of each specific bolt. This fastener definition ignores the hole in the connecting surfaces and instead uses a continuous mesh.

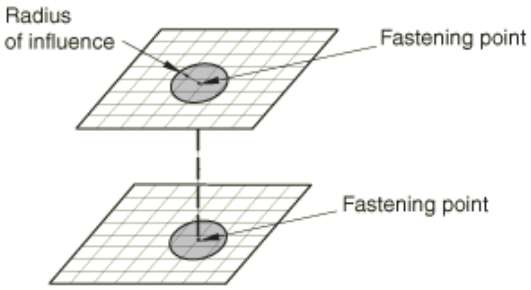

Figure 4.10: *Mesh-independent fastener connection [25].*

All fasteners are modelled using the *CONNECTOR BEHAVIOR keyword in Abaqus. Through this keyword a stiffness definition is given for each of the six degrees of freedom. The longitudinal stiffness K_1 and torsional stiffness K_4 are given by Equations (4.6) and (4.7), respectively.

$$K_1 = \frac{EA}{L} \tag{4.6}$$

$$K_4 = \frac{GJ}{L} \tag{4.7}$$

Here E and A are the Young's modulus and fastener cross-sectional area, respectively. J is the torsional constant. The length of the bolt and the shear modulus are given by L and G, respectively. The shear flexibility C is determined using the Huth equation [65], given in Equation (4.8).

$$C = \left(\frac{h_1 + h_2}{2d}\right)^{a_{fast}} \cdot \left(\frac{b_1}{h_1 E_1} + \frac{b_2}{h_2 E_2} + \frac{b_1}{2h_1 E_3} + \frac{b_2}{h_2 E_3}\right) \tag{4.8}$$

In this equation, h_1 and h_2 are the thicknesses of the two connecting surfaces, d is the bolt diameter and a_{fast} is a fastener type coefficient. In case of metallic bolts $a_{fast} = 2/3$. The Young's moduli of the two surfaces and the bolt are given by E_1, E_2 and E_3, respectively. b_1 and b_2 are coefficients that depend on the material used and the joint type. For bolted single lap shear metallic joints, such as used in the tests, $b_1 = b_2 = 3$ [65].

As the joints in the performed tests are all isotropic, both shear stiffnesses K_2 and K_3 are equal to each other and are given by Equation (4.9).

$$K_2 = K_3 = \frac{1}{C} \tag{4.9}$$

The bending stiffnesses K_5 and K_6 depend on the thickness and material of the fastener and the length over which it can bend. As the fasteners are used to clamp two surfaces together the bending length is almost nonexistent. Additionally, due to the preload in the fasteners, the two surfaces are pressed together. This allows for a negligible amount of bending of the fastener. Therefore the stiffness K_5 and K_6 were set to an arbitrarily high value to inhibit fastener bending behaviour.

When connecting two thin-walled surfaces, such as the L-brackets and the flat plate seen in Figure 3.5, the fastener definition is relatively simple using the method described above. There is, however, also a different type of connection. This occurs when a bolt passes through one of the rig beams, as shown in Figure 4.11. In such a case a choice has to be made whether to connect the two surfaces that are in contact or the two surfaces at the bolt head and nut. The longitudinal and torsional loads in the bolt would act along the entire length of the bolt. The shear load would, however, be carried at the contacting plate when the bolt comes into contact with the edges of the fastener hole.

A combination of both methods is chosen. The fastener elements are positioned at the contacting surfaces, as shown in Figure 4.11. This is done to restrict the motion of the bolt in the Z- and Y-direction, as it would be in the reality. If, instead, the fastener element would be modelled such that it takes the full physical bolt length, the bolt, and thus the plate, would be more free to move in these directions. The bolt length L as used in Equations (4.6) and (4.7) will, however, still represent the actual bolt length. This ensures that the longitudinal and torsional stiffnesses have the correct magnitude.

4.9. Model sensitivities

To study the sensitivity of the numerical model to certain small modelling changes, several alterations of the base model were created. These will be described in this section. Some of these model variations were already described above but will be restated here for clarity.

One modelling choice in the creation of a dynamic finite element model is whether or not damping should be defined in the model. In a dynamic Abaqus/Explicit model, a small

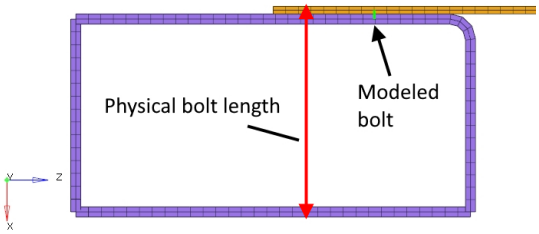

Figure 4.11: *Fastener passing through a beam of the test rig.*

amount of damping is included as standard. This is, however, merely to improve the stability of the model and does not represent any physical effect. This damping is so small that it should not influence the results in any significant way.

Industrial simulations often do not include any material damping since the damping effects are not known for many of the materials used. This leads to conservative modelling results. Additionally, the physics of damping forces in vibrating structures is, as of yet, not understood well. Therefore, it is difficult to model damping forces in vibration problems [66].

To test whether damping could have a positive effect on the accuracy of the numerical model, Rayleigh damping (unrelated to the Rayleigh stress wave) was included as a model variation. Rayleigh damping is a standard function in Abaqus/Explicit and defines a critical damping variable ξ_i for each mode i, as shown in Equation (4.10) [25].

$$\xi_i = \frac{\alpha_R}{2\omega_i} + \frac{\beta_R \omega_i}{2} \tag{4.10}$$

In this equation, ω_i is the natural frequency of mode i. The Rayleigh damping parameters α_R and β_R are user-defined and denote the mass proportional and stiffness proportional damping, respectively. From Equation (4.10) it can be seen that α_R mainly damps the lower frequencies while β_R mainly damps the higher frequencies.

In this research, two damped model versions were created. One with $\alpha_R = 50$ and $\beta_R = 0$ called the α_R-damped model and the other with $\alpha_R = 0$ and $\beta_R = 3e{-}6$ called the β_R-damped model. These values were chosen based on a preliminary sensitivity analysis. The goal was to determine the effect of including material damping. The goal was not to represent the exact damping experienced by the material since no data was available for this.

A second model variation was already described in Section 4.5 and relates to the modelling of the bird. For the base model the SPH bird model was used. This SPH base model is compared to the Lagrangian bird model.

As described previously in Section 4.4, the test rig was added to the FE model. In the base model this test rig was only given elastic material properties. To investigate the validity of assuming only elastic behaviour in the test rig, plasticity was added to the material definition.

In the base model, S4R conventional shell elements were used for most of the structure, except for those components that cannot be assumed as thin-walled. Using S4R elements results in a relatively fast calculation due to a decreased amount of nodes and interpolation points per element.

One problem that occurs in the stiffened plate model when using shell elements can be seen at the intersections between the different stiffeners. The stiffened plate used in the bird impact tests was machined from a solid block of aerospace grade aluminium alloy. As a result of this machining process, fillets were present at these intersections. This is shown in Figure 4.12a. When using shell elements, such a shape cannot be generated. Therefore,

part of the material at these intersections is not included in the model, resulting in a lighter and less stiff intersection.

By using 3D elements these intersections can be approximated more closely, as is shown in Figure 4.12b. A triangular prism element was added at the location of the fillet, representing the extra material in the corner. Similar measures were taken at the other intersection of the plate. This includes the intersection between the stiffeners and the front of the plate seen at the bottom of Figure 4.12b and the intersections at the outward edges of the plate.

(a) *Fillet at a stiffener intersection due to machining.*

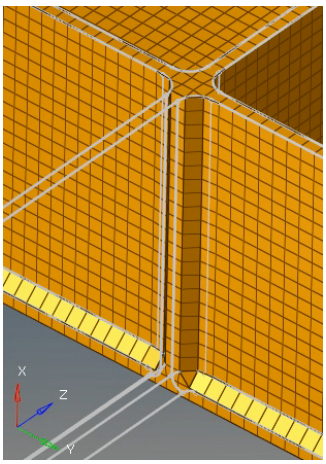

(b) *Improved geometrical approximation when using 3D elements.*

Figure 4.12: *Intersection of two stiffeners in the stiffened plate.*

One drawback of using the 3D elements is the added complexity at these intersections. It took significant extra effort to manually generate these locations, as their geometry was too complex to auto-generate the mesh using Hypermesh. Secondly, to represent the geometry, use had to be made of tetrahedron (C3D4) and triangular prism (C3D6) elements. However, these elements are overly stiff. Therefore, it is recommended that they are used only in non-critical areas [25].

Lastly, as is seen in Figure 4.12b, the created model only used one element through the thickness. When using fully integrated linear brick elements (C3D8), one problem that arises because of this is the effect of shear locking. This effect occurs when the element is loaded in bending and causes the element to overly resist bending deformations [25]. When using elements with reduced integration (C3D8R) instead, the problem of shear locking is solved. However, in its place hourglassing occurs. Hourglassing prevents the element from resisting bending loads. To check whether an excessive amount of hourglassing occurs, a look must be taken at the artificial strain energy in the model. The magnitude of artificial energy must be much lower than the internal energy of the system. Otherwise, this could indicate excessive hourglassing.

To limit shear locking and hourglassing effects, more elements could be used through the thickness. The Abaqus manual [25] recommends using 4 elements through the thickness. For the stiffened plate this would, however, lead to such a fine mesh that Hypermesh could not handle the number of elements. Therefore, this option was not explored. For the flat plate 3 elements through the thickness were used, with each element having a size of 1.5x1.5x1 mm^3.

Due to time constraints, not all model variations were implemented for all 5 tests. Therefore, an overview of the model variations used for each test is given in Table 4.3. In the model investigating the strain rate hardening the base material model was replaced by a Johnson-Cook material definition, as described in Section 4.7.

Table 4.3: *List of model variations that will be analysed per test.*

	Test 2	Test 3	Test 4	Test 5
Base model	x	x	x	x
Damping α_R	x	x	x	x
Damping β_R	x	x	x	x
Rig plasticity	x	x	x	
Lagrangian bird	x	x		
Strain rate hardening	x			
3D full integration elements		x	x	x
3D reduced integration elements		x	x	x
Continuum shell elements	x	x		

4.10. Simplified plate for wave speed determination

As will be described in Section 6.2, the propagation velocity of the stress waves could not correctly be established in the flat plate and stiffened plate models. This was caused by the reflections of stress waves as they hit structural inhomogeneities, such as the accelerometers, dummy mass and stiffeners. Therefore, the theoretical wave speeds described in Section 2.6 could not be compared with any numerical results.

To research the propagation of waves without these interferences, a third finite element model was created, which will be called the 'simplified plate'. This model only consists of a very large square plate, which is impacted at its centre by the SPH bird. This plate uses the same S4R elements, 3.0 mm thickness and aerospace grade aluminium alloy as the base flat plate model. All six degrees of freedom of the nodes at the border are fixed. The plate is meshed using square elements, which are aligned with the borders of the plate. A diagram of the plate is shown in Figure 4.13.

Only the numerical model of this simplified plate was tested and no physical test was created. Therefore, it is only possible to compare its results to the theoretical wave propagation velocities and not to any physical data.

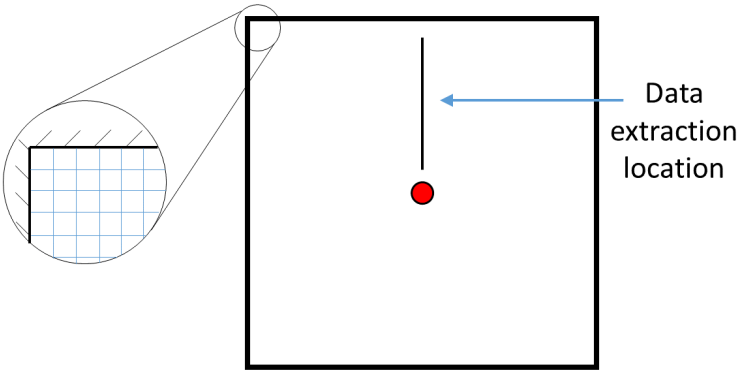

Figure 4.13: *Simplified large plate model.*

When modelling a propagating stress wave using a finite element model, as is the case in this research, the medium through which such waves travel is discretised. The way one chooses to perform this discretisation affects the propagation of the stress waves.

Serón et al. [67] state that a numerical effect that can occur due to the discretisation of a stress wave is that waves can be amplified or attenuated as they propagate. Additionally, the meshing pattern in which the medium is discretised can alter the stress waves as they prop-

agate in different directions. Often the structure through which the stress waves propagate is discretised in a rectangular pattern. This is also done in this research. The effect of this is that stress waves with a certain wavelength are sampled by a different number of nodes, depending on whether they travel tangentially or diagonally through the grid. The diagonally travelling waves will be sampled with $1/\sqrt{2}$ times the number of nodes as those travelling tangentially.

Lastly, as described in Section 2.6 a large number of wave frequencies is excited during bird impact. The high frequency waves will naturally have a shorter wavelength than the low frequency waves. This causes the numerical discretisation to act as a low-pass filter. This is because the high frequency, short wavelength waves are represented in fewer nodes than the low frequency, long wavelength waves. This hinders the propagation of the high frequency waves [67].

It is noted by Serón et al. [67] that to minimise the negative effects of spatial discretisation at least 10 nodes per wavelength are required. The European Space Agency even uses a more stringent recommendation of a minimum of 8 nodes per wavelength [66]. Taking the minimum number of nodes per wavelength N it can be determined what the maximum frequency f_{max} of a correctly represented wave is when using a certain mesh size l. This is determined using Equation (4.11), where c_i the the propagation velocity of the specific wave.

$$f_{max} = \frac{c_i}{N * l} \tag{4.11}$$

Table 4.4 shows for several of the wave types described in Section 2.6, what their maximum frequency is when using a rectangular grid with a mesh size $l = 5mm$ and N=10. In the third column, the maximum frequency is given for waves propagating parallel to the grid. The frequencies $f_{max,diag}$ given in column 4 are scaled by a factor $\sqrt{2}$ for waves travelling diagonally to the grid.

Table 4.4: *Speeds of different types of stress waves for an aerospace grade aluminium alloy plate with h=3 mm, ρ=2.78E-9 tonne/mm³, ν=0.3 and E=74660 MPa.*

Wave type	Wave speed (km/s)	$f_{max}(l = 5\,mm)$ (kHz)	$f_{max,diag}(l = 5\,mm)$ (kHz)
c_L	5.43	103.6	73.3
c_S	3.21	64.2	45.4
c_R	2.98	59.6	42.1

Wave type	Wave speed (km/s)	λ (mm)
$c_F(f = 1\,kHz)$	0.099	99.2
$c_F(f = 10\,kHz)$	0.31	31.4
$c_F(f = 100\,kHz)$	0.99	9.9
$c_F(f = 1000\,kHz)$	3.14	3.1

In Table 4.4, it can be seen that for the flexural waves no f_{max} values are given. This is because for those waves the wave speed and frequency are already interrelated. Therefore, for the different frequency flexural waves the wave speed is known and thus a wavelength λ can be determined using Equation (4.12). This is also given in Table 4.4.

$$\lambda = \frac{c_F}{f} \tag{4.12}$$

5

Analysis methodology

To evaluate and compare the data generated with the physical bird impact tests and the numerical models, the results needed to be processed. A method to determine the propagation velocities of the stress waves is described in Section 5.1. The vibratory response of the plate is evaluated by creating a shock response spectrum, using the data from the accelerometers. The method used to generate such a shock response spectrum is described in Section 5.2. All results were processed using *MATLAB R2018a*.

5.1. Determination of the stress wave velocity

Based on the research questions, the propagation velocities of the stress waves in both the bird impact tests and the numerical models need to be determined. For the bird impact tests, this was done using the displacement data gathered using digital image correlation. For the numerical models, the displacements were directly gathered as nodal outputs. The method described in this section was created by the author. The displacement data is processed and visualised using a MATLAB script written by the author.

To determine the stress wave velocities, a look is taken at the displacements of 'nodes' in the plate. For the numerical model, these are nodes of the finite elements. For the physical plate, these are data points on the DIC grid, as described in Section 3.4. At the start of the experiment, before the bird has impacted the plate centre, the displacement of the entire plate is zero. Upon impact, first, the centre of the plate, that comes into contact with the bird, is displaced. This displacement propagates outward in the form of the stress waves described in Section 2.6. This effect is displayed in Figure 5.1, where the displacement of a range of nodes at increasing distances r from the centre of impact is shown as a function of time for the numerical model of the simplified plate described in Section 4.10.

The wave speed velocity is determined by recording the time at which the wave reaches two distinct nodes, as was shown in Figure 5.1. The nodes that are used for this will be called node 1 at distance r_1 and node 2 at distance r_2 from the centre of impact. The time that these first record a displacement are t_1 and t_2, respectively. The recorded velocity of the stress wave between these two nodes will be called V_{rec} and is determined using Equation (5.1).

$$V_{rec} = \frac{r_2 - r_1}{t_2 - t_1} \tag{5.1}$$

There are two reasons that node 1 is not taken at the centre of impact with r_1=0 mm. Firstly, the bird is not impacting at a single point but over an area dictated by its diameter. This is most clearly seen for the SPH bird described in Section 2.4.2, which has a flattened front. Therefore, the plate is already excited at a location closer to r_2 at the moment of impact. Secondly, during the physical tests, there might be a slight offset in the impact location.

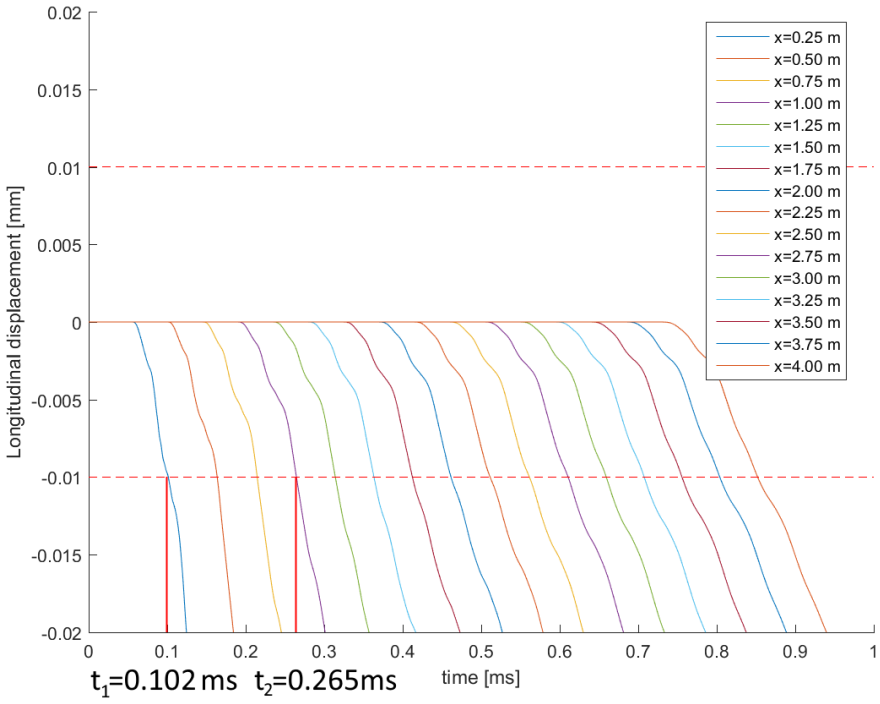

Figure 5.1: *Displacement of nodes, at a distance r=x from the impact, in a direction parallel to the wave propagation, as a function of time. A threshold value of* 10^{-2} *is shown for the wave speed determination.*

Both these factors would change the distance travelled by the stress wave before reaching r_2. This would influence the recorded time t_2. Without correcting for the position of r_1 this would thus lead to a change in V_{rec}. Taking node 1 at a position r_1, which is larger than the diameter of the bird and the potential offset, would eliminate this problem.

One problem in the determination of the wave speeds is the influence of measurement noise or error. In the bird impact tests, for example, to measure the displacement of the plate the digital image correlation (DIC) technique is used. As the DIC technique will always have some margin of error in its data an (erroneous) displacement will influence the recorded wave speed. It might, for example, be that at node 2 some slight movement is already detected due to measurement noise, while in reality, the node has not moved yet. Therefore, a choice must be made for when to count a node to have been displaced. If this is already done for a very small displacement, not the wave itself but the noise is recorded. If this is only done for a large displacement the stress wave might not be recorded at all. Therefore, the concept of a 'threshold value' is used. A wave is only said to have reached a node once the displacement of this node surpasses this threshold value. An example of this is shown in Figure 5.1, in which the threshold value was set to 10^{-2}.

The value to which this threshold value is set will influence the recorded wave speed. This can be seen in Figure 5.2, which shows the same data as Figure 5.1 but with a threshold value of 10^{-5}. The values of both t_1 and t_2 are lower when using this lower threshold value. However, they decrease by differing amounts, resulting in a change of recorded wave speed. Therefore, it must be investigated in what way the choice of threshold value influences the recorded wave speed. From this analysis, it must be determined whether there is a specific threshold value for which the recorded wave speed corresponds to the theoretical wave speeds from Section 2.6. This is done in Section 6.2.

In Section 2.6, multiple types of waves have been described with their own characteristics. When determining the recorded wave speed, a distinction must be made between these wave types. The longitudinal wave shows an in-plane movement of the material, tangentially to

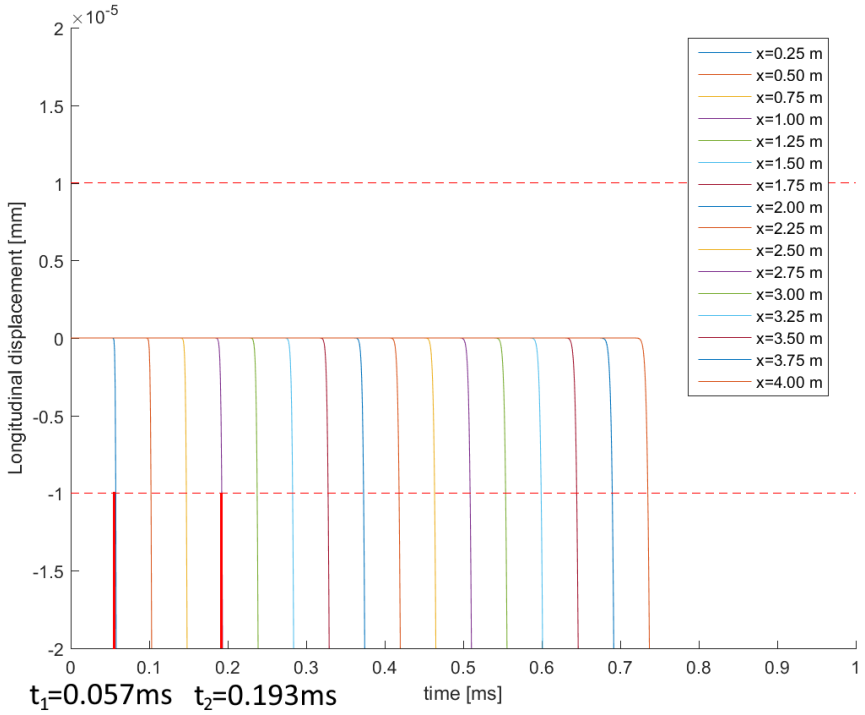

Figure 5.2: *Displacement of nodes, at a distance r=x from the impact, in a direction parallel to the wave propagation, as a function of time. A threshold value of* 10^{-5} *is shown for the wave speed determination.*

the wave propagation direction. Shear horizontal waves also displace the material in-plane, but in a direction parallel to the wave front. Flexural and Rayleigh waves are characterised by an out-of-plane movement. To distinguish between the propagation velocity of these wave types, a distinction is made between the displacement direction of the nodes. However, as flexural and Rayleigh waves both result in out-of-plane displacement, their distinction may not always be clear.

The shear horizontal wave was not evaluated in this research. This was due to the nature of the impact loading used in this research. As the bird impacted perpendicularly with respect to the plate surface, a radial symmetry was present in the loading. Therefore, no loads and, thus, no displacements were expected in the direction parallel to the wave front.

A source of error in the determination of the out-of-plane wave may be caused by the influence of the longitudinal wave. As the velocity of the longitudinal wave is higher than the other waves, it will reach node 2 first. When this happens it might not cause a perfect longitudinal displacement. Instead, a small displacement in the out-of-plane direction may also be seen. Therefore, the threshold value will influence the recorded wave speed of the different wave types. The sensitivity of the recorded wave speeds to different threshold values is discussed in Section 6.2.

5.2. Shock response spectrum

To investigate the accuracy of the numerical model in simulating the vibratory response of the structure, the output data of the accelerometers must be evaluated. However, the vibration data in the form of an acceleration-time history, such as shown in Figure 5.3, is not suitable to determine the severity of vibration [66]. Therefore, the acceleration signal needs to be represented in a different way.

One way to analyse vibrations is by transforming the acceleration-time signal into a shock response spectrum (SRS). This method is commonly used in the space industry for launch

vibrations and pyrotechnic stage separation [66], as well as for earthquake analysis and the testing of computer components [68]. Such an SRS is used to evaluate the ”severity or damaging potential” of a shock event. Additionally, it can be used to compare multiple shock events [66]. The European Space Agency (ESA) characterises the SRS as ”universal tool for describing shocks” [66].

What a shock response spectrum exactly is and how it is created is described in Section 5.2.1. The method described was implemented using MATLAB. The calculation of the SRS itself was done using a MATLAB script made available by NASA shock and vibration specialist T. Irvine [68]. However, this code was adjusted in order to be compatible with the acceleration data used for this thesis. Additionally, the code was expanded to better visualise and compare the shock response spectra.

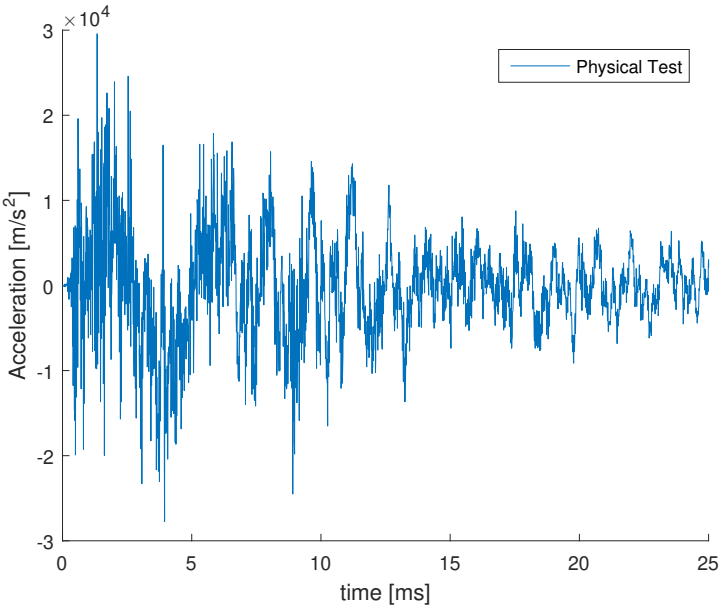

Figure 5.3: *Measured acceleration signal of a bird impact event, recorded near the impact location.*

5.2.1. Generation of the shock response spectrum

To generate a shock response spectrum, the acceleration-time signal $\ddot{y}$ is applied to a set of single degree of freedom (SDOF) damped harmonic oscillators. Each of these oscillators is defined with a certain ordinary natural frequency f_n. This is visualised in Figure 5.4.

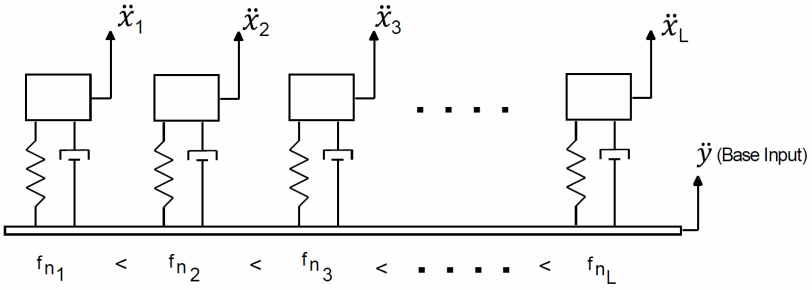

Figure 5.4: *Set of single degree of freedom damped harmonic oscillators subjected to acceleration signal $\ddot{y}$ [68].*

In case of a digital input signal, the acceleration response $\ddot{x}$ of such a SDOF system is calculated using Equation (5.2) [68, 69].

$$\begin{aligned}\ddot{x}_i = &+ 2\exp[-\xi\omega_n\Delta t]\cos[\omega_d\Delta t]\ddot{x}_{i-1} \\ &- \exp[-2\xi\omega_n\Delta t]\ddot{x}_{i-2} \\ &+ \left\{1 - \left(\frac{1}{\omega_d\Delta t}\right)\exp[-\xi\omega_n\Delta t]\sin[\omega_d\Delta t]\right\}\ddot{y}_i \\ &+ \left\{2\exp[-\xi\omega_n\Delta t]\left(\left(\frac{1}{\omega_d\Delta t}\right)\sin[\omega_d\Delta t] - \cos[\omega_d\Delta t]\right)\right\}\ddot{y}_{i-1} \\ &+ \left\{\exp[-2\xi\omega_n\Delta t] - \left(\frac{1}{\omega_d\Delta t}\right)\exp[-\xi\omega_n\Delta t]\sin[\omega_d\Delta t]\right\}\ddot{y}_{i-2}\end{aligned} \tag{5.2}$$

In this equation, $\ddot{y}$ is the acceleration input signal, ξ is the damping ratio, $\omega_n = 2\pi f_n$ is the angular natural frequency in radian per second, ω_d is the damped natural frequency described by $\omega_n\sqrt{1-\xi^2}$, Δt is the time step length and subscript i denotes the time step. A complete derivation of this equation is given by Irvine [70]. Often the damping ratio is given in the form of the quality factor Q as related to ξ by Equation (5.3), where ξ is commonly taken as 5%, resulting in $Q = 10$ [66].

$$Q = \frac{1}{2\xi} \tag{5.3}$$

Equation (5.2) has to be applied to each harmonic oscillator individually and each oscillator therefore has its own response. When this is done, the peak negative and positive accelerations for each oscillator are recorded. These peak accelerations are data points in the shock response spectrum. Figure 5.5a shows how the data points of the harmonic oscillators with $f_{n_{25}} = 40$ Hz, $f_{n_{65}} = 403.2$ Hz, $f_{n_{109}} = 5120$ Hz are used to build up the SRS. These specific natural frequencies are simply examples but their values are determined by Equation (5.4), as explained below. By doing this for a large number of oscillators, the peak acceleration response of a component to a vibration can be plotted as a function of the natural frequency of this component.

The number of harmonic oscillators and their frequencies for which Equation (5.2) is evaluated can be chosen arbitrarily. It is however recommended that the signal sampling frequency is at least 10 times higher than the maximum frequency $f_{n_{max}}$ used [71]. As the sampling frequency used was 100 kHz, the maximum natural frequency to be evaluated is 10 kHz. This also corresponds with the maximum natural frequency recommended by the European Space Agency for medium and far-field impacts [66]. The ESA defines medium-field locations as those where the vibration is influenced by a combination of the direct propagating stress waves and the resonance response of the structure, created by the reflection of waves from the boundaries. At the far-field, the vibrations are mostly dependent on the structural response.

A common choice for the natural frequencies is to use a proportional bandwidth. In this research, it was chosen to use a spacing of 1/12 octave, which is recommended as the maximum spacing [66]. The lowest frequency for which the shock response spectrum is analysed is 10 Hz, which was used in the documentation of T. Irvine [68]. Therefore the ordinary natural frequencies f_n of the harmonic oscillators are given by Equation (5.4).

$$\left\{f_{n_j}\right\}_{j=1}^{j=120} = 10 * 2^{((j-1)/12)} \tag{5.4}$$

Successive natural frequencies are thus related by Equation (5.5).

$$f_{n_{j+1}} = f_{n_j} * 2^{(1/12)} \tag{5.5}$$

In between the frequencies given by Equation (5.4) the peak accelerations are found using linear interpolation.

Often one is only interested in the maximum absolute peak accelerations without the distinction between positive and negative acceleration. Therefore, these two plots are most often combined to form a single absolute peak acceleration graph called the maximax [66]. An example of this process is shown in Figure 5.5b.

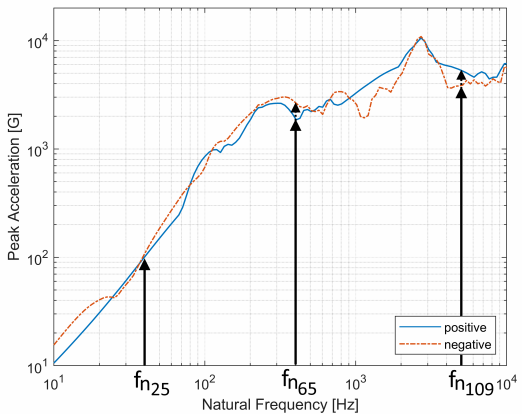

(a) *Construction of the shock response spectrum.*

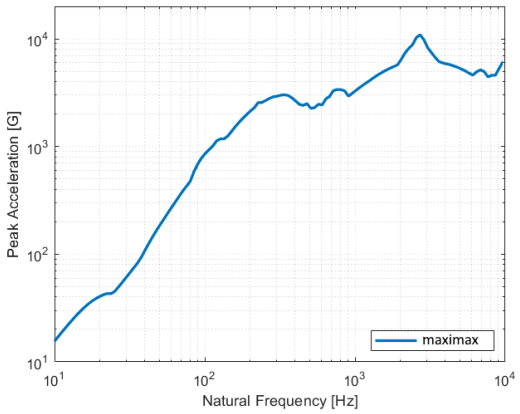

(b) *The maximax shock response spectrum showing only the maximum absolute peak acceleration.*

Figure 5.5: *Visualisation of the construction of the shock response spectrum.*

From the shock response spectrum in Figure 5.5b, it can be determined what the peak acceleration of a component is when subjected to the vibration used to generate this SRS. For example, if this component has a natural frequency of f_n=700 Hz, it would experience a peak acceleration of, approximately, 4000 G. However, if the component subjected to the vibration has a natural frequency of f_n=1000 Hz, it would experience a peak acceleration of 1100 G. Such information can be used in the design of a component. In this example, the peak acceleration experienced by a component can therefore be significantly reduced by altering its natural frequency from 700 to 1000 Hz.

5.2.2. Error sources of the shock response spectrum

One potential source of error can occur due to the transverse sensitivity of an accelerometer. This is the ”sensitivity of the accelerometer at 90 degrees to the sensitive axis of the sensor” [72]. This means that the measured voltage of the accelerometer may be influenced by accelerations perpendicular to its intended direction of measurement. For the used Endevco 7270A-60KM6 accelerometer, this sensitivity may be as high as 5% [63]. This may be problematic when the vibrations perpendicular to the measurement direction of an accelerometer are on the same order of magnitude as those parallel to the measurement direction.

A second source for error in the generation of the SRS signal is a zero shift of the acceleration-time input signal. A zero shift, sometimes called baseline shift, is an offset of the measured acceleration compared to the actual acceleration. This may be caused by several things. For example the effect of temperature on the accelerometer for the used sensor may lead to a maximum shift of 10 mV, which corresponds to 60 g [63].

Such a zero shift can alter the peak acceleration response for low natural frequencies in the shock response spectrum. In the SRS this can be recognised by a large difference between the positive and negative peak accelerations. To correct a shifted signal, the method described by Piersol [73] and the ESA [66] is used. In this method, the mean acceleration over the entire data set is determined. If this deviates from zero, this would indicate a net change in velocity ΔV. However, when the duration over which the acceleration is recorded is long enough, the accelerometer should start and end at rest. This would result in a net velocity change

$\Delta V = 0$. Therefore, the calculated average acceleration is subtracted from the acceleration signal, resulting in a net velocity change $\Delta V = 0$. An example of the effect of this correction is shown in Figure 5.6.

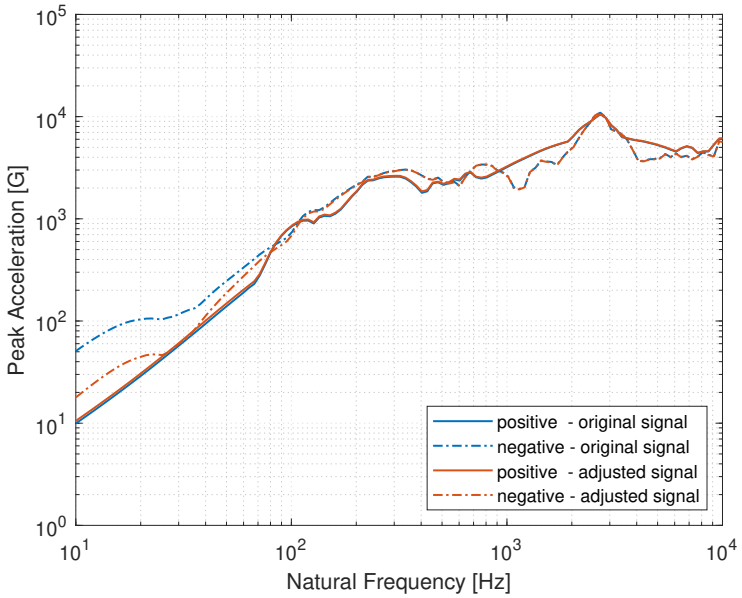

Figure 5.6: *Shock response spectrum of sensor 2 of test 5, with Q=10. Based on the original signal and the signal adjusted for base shift.*

Another factor influencing he generation of the shock response spectrum is the length of the acceleration-time signal used for the input signal $\ddot{y}$. One can imagine that if only short duration signal is used that does not encompass the entire vibration event, not all energy contained in the vibration is taken into account in the SRS calculation. The available recording length of an acceleration signal may, however, be limited. In this research, this was especially the case for the acceleration signal generated with the numerical model. It is computationally expensive to continue the numerical simulation for a long time. Often during bird impact analysis only about 5 ms after impact are simulated. This is because, after that time, the damage created by the bird impact has already occurred.

To establish an appropriate analysis time, the SRS of several different acceleration signals was generated using varying time intervals. This was done using the accelerometer data of some of the physical bird impact tests. This original data had a recording length of 500 ms. Two examples of these signals are shown in Figures 5.7a and 5.7c. The shock response spectra of these signals were generated while limiting the used signal length to 1 ms, 5 ms, 25 ms, 100 ms and 450 ms, starting at the moment of impact. The resulting shock response spectra are shown in Figures 5.7b and 5.7d, respectively.

It is seen that a shorter time interval results in a lower peak acceleration in the SRS. While this effect is present at all natural frequencies, it is most pronounced at lower natural frequencies. Both examples show that, when only a 1 or 5 ms portion of the vibration signal is used, the SRS cannot be correctly generated. When a 25 ms portion of the acceleration signal is used, it depends on the nature of the input signal whether or not the SRS is generated correctly.

The first example shows that a 25 ms signal length results in an almost identical SRS as when the entire 450 ms signal had been taken. The second example, however, indicates a discrepancy between the SRS when using a 25 ms input signal or a longer 100 ms or 450 ms signal.

The difference between these two examples is likely caused by the more rapid decrease in the amplitude of the accelerations in Figure 5.7a. Therefore, after 25 ms, the vibration has

already dampened to such an extent that cutting off the signal after this point does not affect the SRS. In contrast, the acceleration signal in Figure 5.7c shows less damping. Therefore, the amplitude of the signal after t=25 ms is still large enough to influence the SRS. The required evaluation time is therefore dependent on each individual acceleration signal.

In this research, the evaluation time was fixed at 25 ms. This was done to limit the computational time required for the numerical simulation, while still including most of the energy present in the vibration signal. To allow for an accurate comparison between the numerical and physical test results, the evaluation time of the physical tests was therefore also limited to 25 ms. Thus, it is important to realise that this may result in an underestimation of the peak acceleration for low natural frequencies.

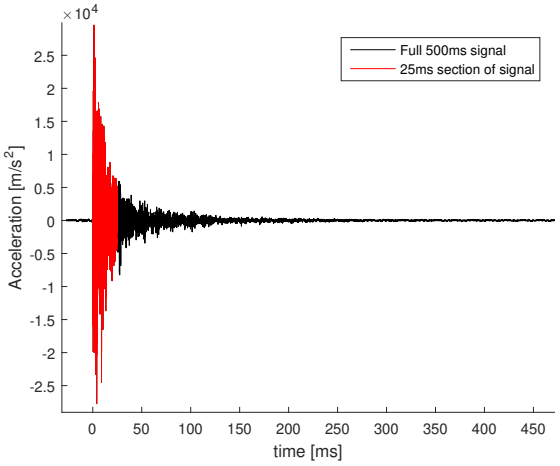

(a) *The acceleration-time signal of accelerometer 1 in test 5.*

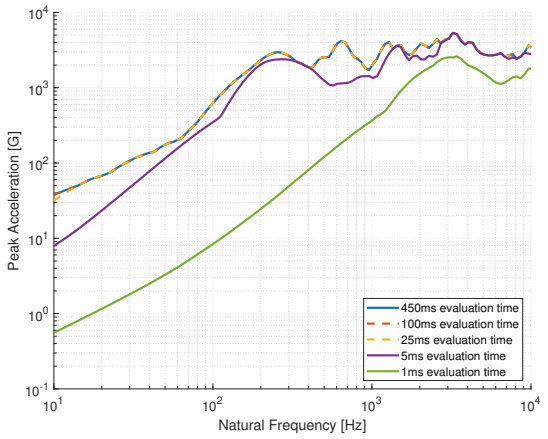

(b) *SRS of the vibration data at accelerometer 1 in test 5, with Q=10.*

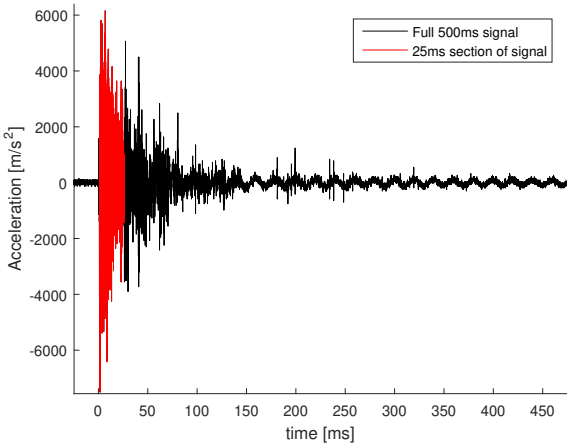

(c) *The acceleration-time signal of accelerometer 6 in test 4.*

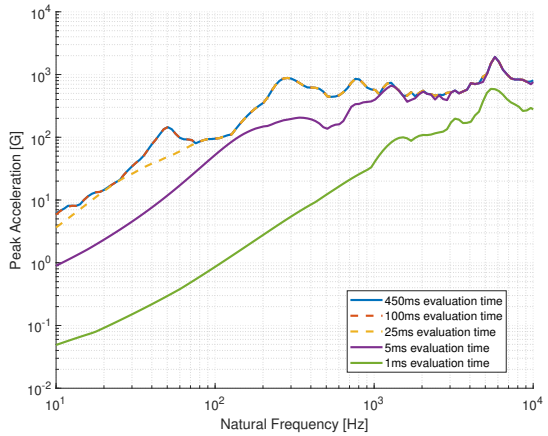

(d) *SRS of the vibration data at accelerometer 6 in test 4, with Q=10.*

Figure 5.7: *The effect of using different evaluation times of the input signal on the SRS.*

5.2.3. From shock response spectrum to shock specification

As described in Chapter 1, this research is meant to assess the capability of a numerical model to predict the vibratory response of components affected by the shock of a bird impact. Therefore, this subsection briefly describes how shock response spectra can be used to set up the shock resistance requirements of a component. This shock resistance requirement can then be taken into account during the design of such a component. The method described is a brief summary of the European Space Agency mechanical shock design and verification

handbook [66]. It will not be applied in this thesis but is only shown for context.

To establish the requirements on the shock resistance of a component, first, all possible vibrations during a components life must be determined. This is done by testing the structure to which this component is attached for all the shock events that it may encounter. For each shock event, the vibratory response at the location of the component is recorded as an acceleration-time signal. These vibrations are either determined using a physical tests or a numerical analysis.

These acceleration-time signals are then converted into their shock response spectra. An example of a collection of such SRSs is shown in Figure 5.8. In this image, the shock response spectra of 9 different vibrations are shown. These shock response spectra can be used to define a shock specification for the component.

Such a shock specification is a simplified curve in the SRS plot that exceeds all used the shock response spectra by a certain margin. ESA describes adding a margin of 3 dB. The specification is often built up of two straight lines on the SRS log-log graph, as is shown in Figure 5.8. The specification consists of a section of constant slope, with a minimum slope of 6 dB/Octave. This transitions into a section of constant magnitude. By taking this shock specification into account during the design process of the component subjected to these vibrations, failure of this component can be prevented.

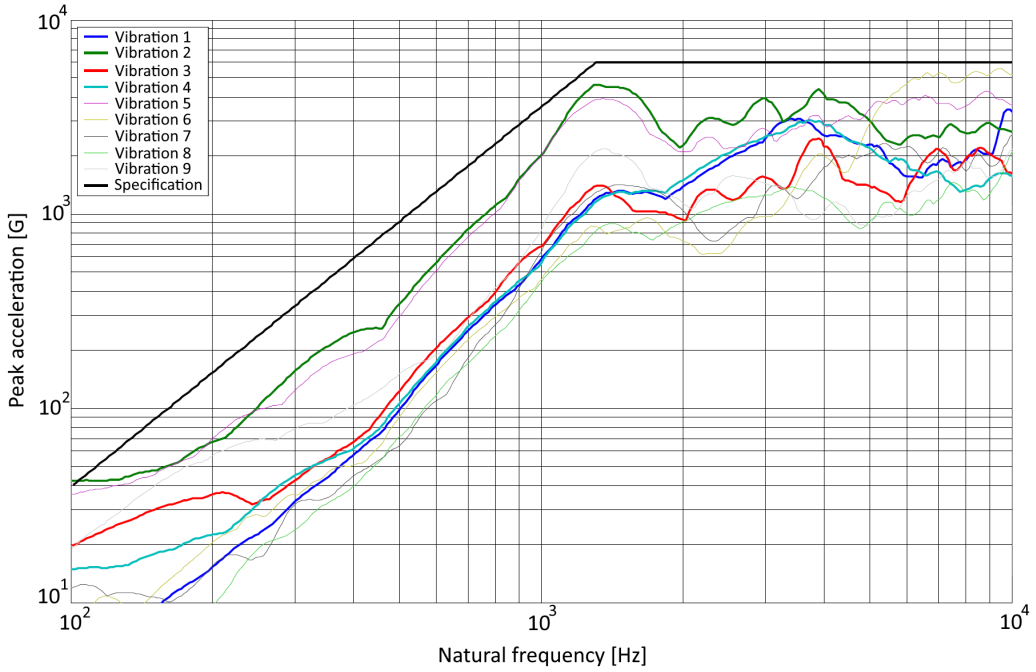

Figure 5.8: *Construction of a component shock requirement specification from a maximum expected shock environment [66].*

6

Results and discussion

Several different types of output have been generated to analyse the results of the numerical model. These output results are presented and discussed in this chapter. Firstly, in Section 6.1 it will be evaluated whether the dynamic response seen in the numerical model agrees with the test data by comparing the displacement at the centre of impact. Additionally, the deformations seen in the bird impact tests will be visually compared to those determined in the models. Secondly, the theoretical wave propagation velocities are compared to that found in the model in Section 6.2. The propagating waves are also analysed qualitatively. Finally, to determine the capability of the numerical model to predict the vibratory response experienced by the plate and the system mounted nearby the impact zone, the shock response spectra are analysed in Section 6.3.

6.1. Global structural response

A first step to validate the accuracy of the numerical models is to look at the dynamic response of the structure. This is done in two ways. Firstly, the out-of-plane displacement at the centre of impact of the models and physical tests is compared. Secondly, the dynamic response generated by the numerical models is visually compared to the video images of the bird impact tests. Sections 6.1.1 and 6.1.2 discuss the response of the flat and stiffened plate, respectively.

6.1.1. Flat plate response

As the first test plate (test 1) ruptured upon impact of the bird, this test will not be analysed. Therefore, first, the results of test 2 will be evaluated. In this test, a dummy mass of 5.0 kg was used and the bird impacted with a velocity V_{imp}=106.1 m/s at the centre of the plate. In Figure 6.1, the out-of-plane displacement at the centre of impact is given for the flat plate during test 2. The physical bird impact test is compared to the base model. The displacement for the physical test is only plotted up to t=16.3 ms because no more data was available. The moment of impact was not exactly known for the DIC data. Therefore, the timing of the DIC data is synchronised by setting the moment at which the displacement starts to rapidly increase as t=0.

It is seen that the maximum displacement at the centre of impact is predicted quite well. While the physical test shows a maximum displacement of $\Delta X_{max,test}$=66.4 mm, the base model predicts a maximum displacement of $\Delta X_{max,base}$=63.6mm. This is an underestimation of only 4.2% in the base model compared to the physical test. The time to reach this maximum displacement t_{max} is shorter for the numerical model than the physical test. Somehow, the numerical model seems to initially provide less resistance to deformation than the plate in the physical test. For test 2, $t_{max,base}$=3.6 ms and $t_{max,test}$= 5.5 ms.

One of the most striking discrepancies between the physical tests and the simulation is seen

after the maximum displacement is reached. The physical test shows that the maximum displacement is retained from approximately t=5.5 ms to t=10 ms. Instead, the numerical result shows an immediate bounce-back. While the exact reason for this discrepancy is unknown, one possible contributing factor could be the assumption of pure elastic behaviour of the test rig. This is further discussed later in this section in the evaluation of Figure 6.9.

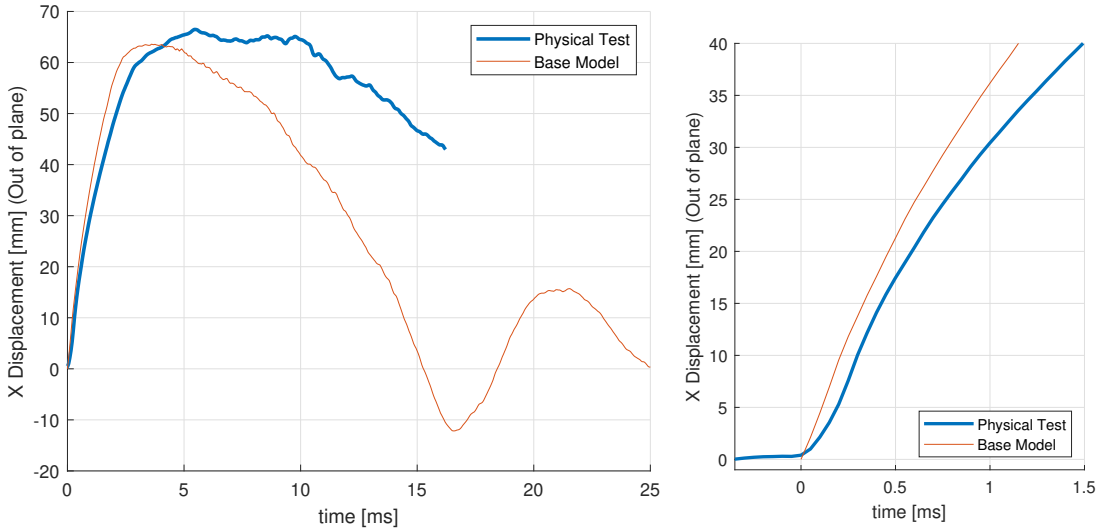

(a) *Overview.* ***(b)*** *Detailed view.*

Figure 6.1: *Comparison of the out-of-plane displacement at the centre of impact of test 2 for the physical test and the base model.*

Another discrepancy between test and simulation is found in the initial response of the plate. This is shown in the detailed view in Figure 6.1b. The physical test shows a slightly more gradual increase in the displacement, whereas the numerical results indicate an immediate response after impact. Despite this slower response of the physical test, both the model and test result show similar increasing slopes between t=0.25 ms and t=0.5 ms. After this, the test and simulation start to slightly diverge. The immediate response of the numerical analysis is likely caused by the flat front of the SPH bird model, as was shown in Figure 2.9. This is further evaluated in the discussion of Figure 6.9.

Additionally, it is seen that in the physical test 2, even before the moment of impact at t=0, a small displacement is recorded at the centre of the plate. The position of the plate at the start of the digital image correlation (DIC) recording (at t=-0.35 ms for test 2) is set as a reference point where the displacements are zero. From this moment on, the displacement is seen to increase from ΔX=0.0 mm at t=-0.35 ms to ΔX=0.3 mm at t=0 ms. Two possible causes are identified. Firstly, it may be the result of a measurement error in the DIC data. Secondly, it may be caused by airflow expelled by the bird cannon, which precedes the bird itself. As the influence of air has been neglected in the numerical analysis this would not be seen in its results.

An additional cause of the discrepancies between test and model, may lie in the recording of the displacement of the physical test instead of the quality of the model. To capture the displacement, digital image correlation was used. As described in Section 3.4, the DIC data consists of a rectangular grid of data points on the plate. However, the alignment of this grid to the actual plate was not exactly known. Therefore, the location on the plate that corresponds to the displacement shown in Figure 6.1 may not be the exact centre of the plate. Instead, the grid point is chosen based on where the maximum displacement occurs. Additionally, the grid has a spacing of 28-35 mm. Therefore, if the maximum displacement occurs at a location in between these data points, the displacement would be underestimated.

For the displacement of the numerical analysis, the centre of the plate was taken. In the

numerical model, this is the exact location of impact. Coincidentally, this is the point which shows the largest displacement. The plate centre is also targeted during the physical tests. In the physical test, however, a slight offset in impact location may be present due to influences such as the aerodynamics of the bird. To ensure that this offset was small, the video footage of the impact was used to verify that the bird impacted, approximately, at the centre of the plate.

A different way to compare the displacement of the physical test with the numerical results is shown in Figure 6.2. Here, the displacement of a cross-section of test 2 is plotted for several different time instances. This cross-section is shown in Figure 6.3. It runs horizontally from one side of the plate (Y=-1000 mm) to the other (Y=+1000 mm) and is centred in the vertical direction (X=0). At Y=0 mm, the position corresponds to the centre of impact. The physical test and base model results are given by the solid line and dashed line, respectively. The interruptions in the physical test data indicate a lack of displacement data generated by the DIC system. From Y=400 to Y=720 mm, this is because the dummy mass blocks the view of DIC cameras. At Y=-500 to Y=-590 mm, this is caused by the accelerometer interrupting the speckle pattern.

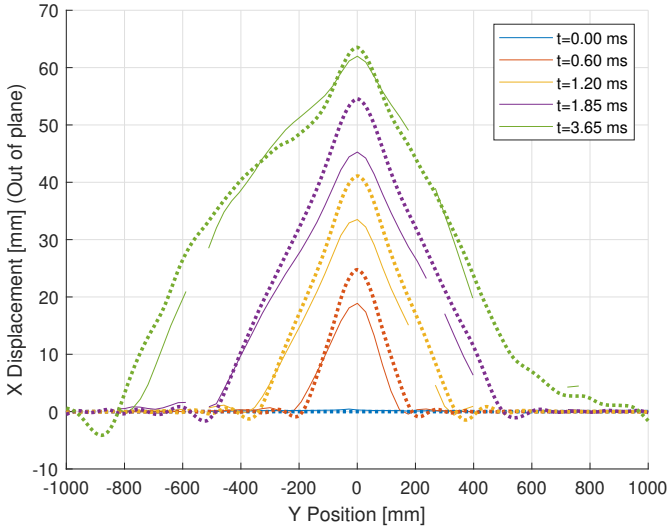

Figure 6.2: *X-displacement of a horizontal cross-section of the plate in test 2 of both the physical test (solid line) and base model (dashed line).*

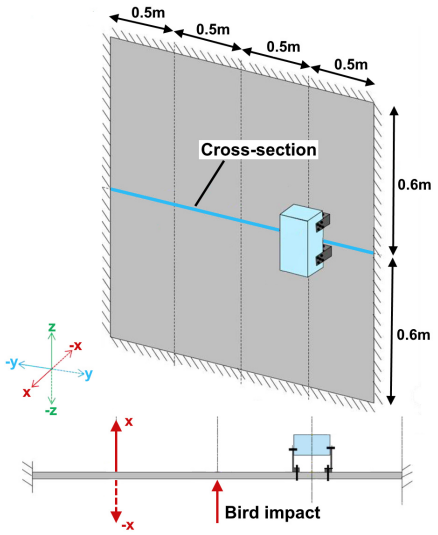

Figure 6.3: *Location of the cross-section shown in Figure 6.2.*

This visualisation method was used by Mohagheghian et al. [23] and gives better insight into the movement of the entire plate. As was seen in Figure 6.1a, at the centre of the plate the numerical model shows a more rapid increase in displacement than the physical test. However, this discrepancy seems to decrease further away from the centre.

A second discrepancy between the physical test and the numerical model is seen in the symmetry of displacement around Y=0 mm. The displacement shown by the numerical model is almost perfectly symmetrical up to t=1.85 ms. This is because, except for the dummy mass, the numerical model is symmetrical over the XZ-plane, where Y=0. Up to t=1.85 ms, the displacement of the plate near the dummy mass is small. Thus, the asymmetry caused by the dummy mass is not clearly visible yet. The displacement of the physical test, however, shows clear asymmetrical behaviour from the start. This can have multiple reasons. Firstly, it might be caused by the spatial calibration of the DIC data. As described before, the spacing of the DIC data points was 28-35 mm. The position of the DIC data points in relation to the plate was calibrated by assuming the point of maximum displacement coincides with the centre of the plate. If the actual location of maximum displacement lies in between two data points, this calibration would result in a slight shift of the DIC data along the Y-axis. A second cause of the asymmetry might be an offset of the impact location of the bird in the

physical test.

The out-of-plane displacement of impact test 2, based on the DIC data, is given in Figure 6.4 and compared to contour plots of the base model. The colours used to indicate a certain displacement in the DIC images are similar, but not exactly equal, to those used in the contour plot. Therefore, some care must be taken when comparing these images.

These images make clear how some details are not captured using the DIC technique. This is seen when comparing Figures 6.4a and 6.4b. While the large displacements are captured in the DIC data, the small ripples seen in the base model are not. This was not due to an absence of such ripples in the physical test, since they were seen in the slow-motion video footage.

A good qualitative agreement is seen between the displacements in the impact test and the base model. At $t \geq 2.75$ ms, it can be seen how, in the base model, the test rig limits the displacement of the plate. Near the edges of the plate, where the plate folds over the inner edge of the test rig, a crease is formed. Additionally, the influence of the bolts, that attach the plate to the test rig, is seen at all the outer edges. Especially in Figure 6.4d, it is seen that in between the bolts, the plate shows a negative displacement, i.e. opposite to the flight direction of the bird. At the bolt locations, the plate is fixed more closely to the test rig. These same influences of the test rig are seen in the DIC images, although not as clearly. This is largely because the edges of the plate are not fully covered by the DIC data.

A good correlation between test and model is also seen in the way in which the dummy mass limits the displacement of the plate when $t \geq 2.75$ mm. A small area of DIC data is available on the upper surface of the dummy mass. When t=2.75 mm, no movement of the dummy mass is seen in both test and model, even though the plate underneath the dummy mass already somewhat displaced. This hinders the displacement of the centre of the plate. However, this does not stop the plate from displacing above and below the dummy mass.

The first movement of the mass is seen at t=4.0 mm, where a displacement of 5 to 10 mm is recorded for both the test and the model. At t=5.25 ms, this increases to, approximately, 15 mm for the impact test and 17 mm for the numerical model. Additionally, a rotation of the dummy mass was seen, which was similar in the test and the model. However, this is not clearly seen from these images.

At t=4.0 ms, the DIC data shows negative displacement in all four corners. This behaviour is correctly shown in the numerical model. A discrepancy that is seen at both t=4.0 ms and t=5.25 ms is that the DIC data shows that a large area is displaced by over 50 mm. This area of high displacement is more limited to the centre of the plate in the base model.

Additional qualitative comparison of the model to the physical test is performed. Firstly, the dynamic behaviour of the dummy mass is evaluated. This is done by comparing high-speed video footage of camera 1 (see Figure 3.1) with an animation of the numerical base model. As shown in Figure 6.5, before t=2.0 ms there is very little deformation in the L-bracket as the plate at this location has not displaced much yet. At t=2.0 ms the plate starts to be pressed towards the dummy mass. At t=2.6 ms this leads to contact between the bolt and the dummy mass. Therefore, from t=2.0 to t=2.6 ms the L-bracket changes from almost zero deformation to maximum outward bending. The video footage of physical test 2 shows the same deformation behaviour of the L-bracket. This footage is not shown here, since the low resolution makes it difficult to see this from still images. In video format, however, this could be seen clearly.

Additionally, the deformation of the flat plate itself is evaluated. In the video images of camera 4 (see Figure 3.1) it is seen that approximately 2.2 ms after impact a folding line appears vertically in between two of the centre bolts. This is shown in Figure 6.6a. This can be compared to the still image of the base model at t=2.25 ms in Figure 6.6b. While some forward displacement of the plate between the bolts does appear in the model, the extent of folding seen in the impact test could not be recreated. In the physical test, this folding

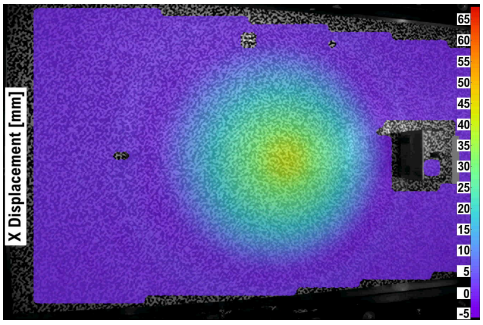

(a) *DIC, t=1.5 ms.*

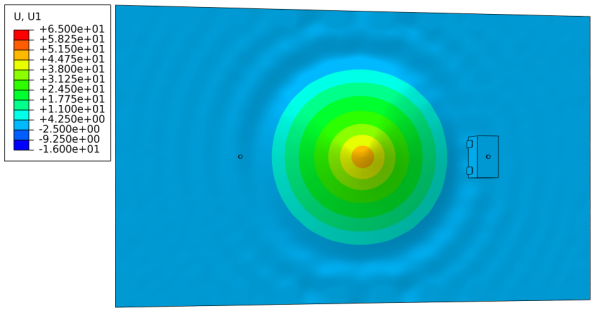

(b) *Base model, t=1.5 ms.*

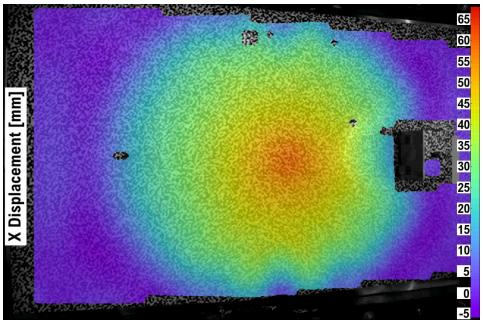

(c) *DIC, t=2.75 ms.*

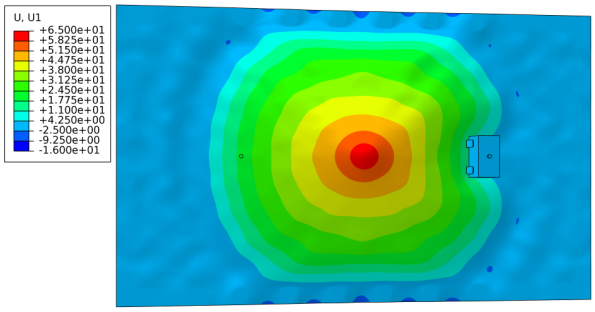

(d) *Base model, t=2.75 ms.*

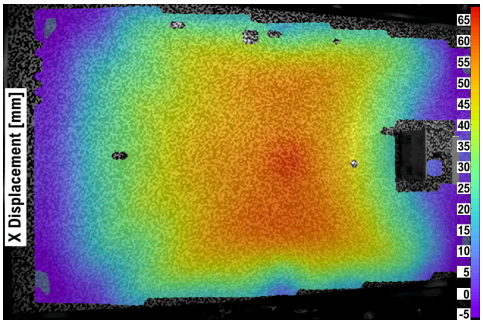

(e) *DIC, t=4.0 ms.*

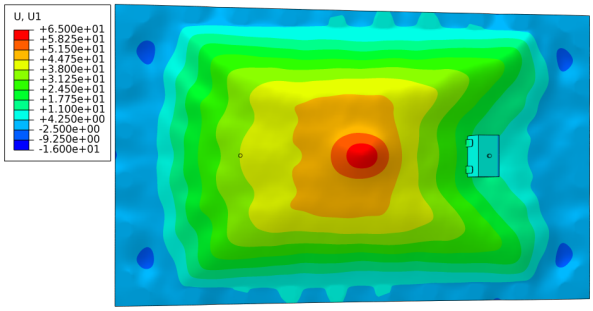

(f) *Base model, t=4.0 ms.*

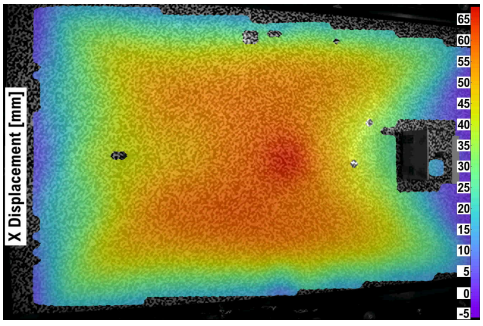

(g) *DIC, t=5.25 ms.*

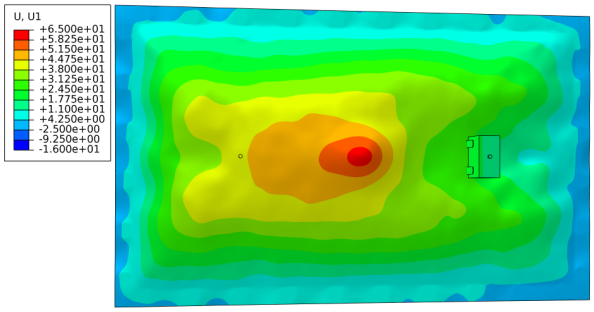

(h) *Base model, t=5.25 ms.*

Figure 6.4: *Comparison of the out-of-plane displacement of the impact test 2 and the base model, in millimetre.*

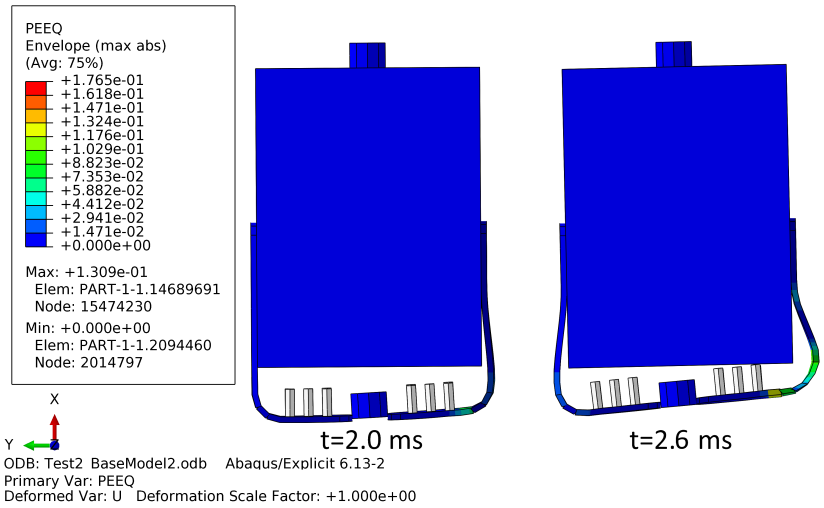

Figure 6.5: *Contour plot of the equivalent plastic strain (PEEQ) of the dummy mass and L-brackets in test 2, at t=2.0 and t=2.6 ms.*

resulted in significant plastic deformation. However, no large plastic deformation was seen at this location in the numerical models.

It is unclear what the exact cause of this folding is. One possible cause is that, in the physical tests, the bolts are pre-tensioned. In the Abaqus/Explicit software a pretension definition was not available and only the stiffnesses of the individual bolts were defined, as described in Section 4.1. This restricts the movement of the plate in the physical tests more than in the numerical tests.

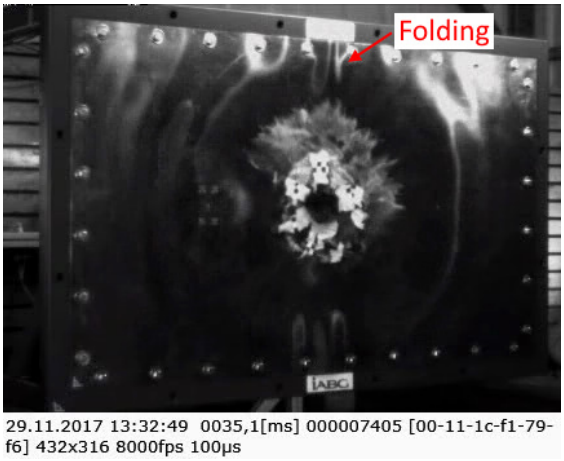

(a) *Physical test 2 at t=2.2 ms.*

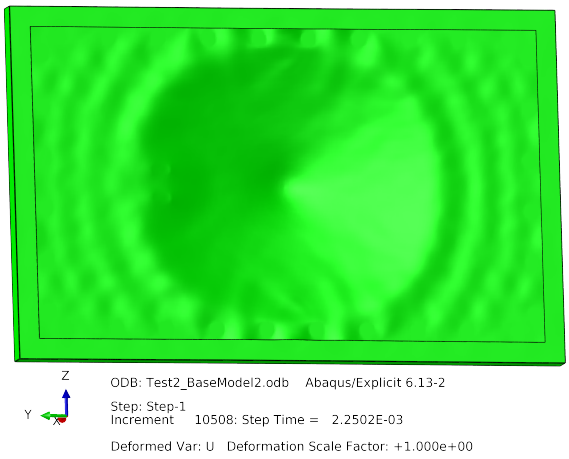

(b) *Base model simulation of test 2 at t=2.25 ms.*

Figure 6.6: *Comparison of the folding seen in the physical test 2 with the numerical simulation at t=2.2 ms.*

Each exact test was only performed once. Therefore, the extent of scatter in the physical test result could not be determined. However, test 3 was equal to test 2 with two exceptions. In test 3, a 7.5 kg dummy mass and an impact velocity of V_{imp}=124.9 m/s was used. Test 3 can be used to evaluate whether the same dynamic behaviour is seen in both tests and whether the numerical model represents the physical test equally well.

As is shown in Figure 6.7, the behaviour of the plate seen for test 3 was very similar to that of test 2. Physical test 3 reaches a higher maximum displacement of $\Delta X_{max,test}$=70.6 mm at $t_{max,test}$=4.5 ms. This higher displacement logically follows from the higher impact velocity.

The result of physical test 3 is only plotted up to t=9.8 ms, as no more data was available. Similarly, no data was available before the moment of impact. Therefore, it is not known whether, like in test 2, the plate already starts to displace before impact.

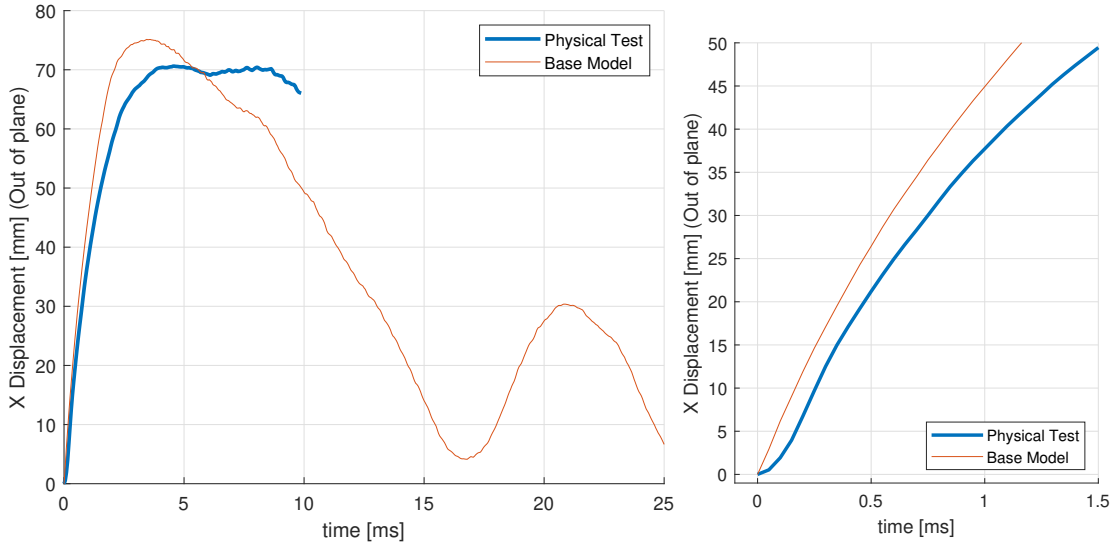

(a) *Overview.* ***(b)*** *Detailed view.*

Figure 6.7: *Comparison of the out-of-plane displacement at the centre of impact of test 3 for the physical test and the base model.*

The maximum displacement predicted by the base model was found to be $\Delta X_{max,test}$=75.1 mm at $t_{max,test}$=3.6 ms. While the base model of test 2 underpredicted the maximum displacement by 4.2%, the base model of test 3 overpredicts it by 6.4%. It is unclear what causes this difference. As both tests and models are very similar, one would expect a similar over- or underprediction. This could be the result of small differences in the physical test, such as material properties or manufacturing differences. However, as each test was only performed once, no such variability can be detected.

As was explained in Section 4.9, several changes to the numerical model were implemented to evaluate the sensitivity of the model to these changes. The first variations to the model that will be evaluated are the models to which material damping is added. For test 2, in addition to the base model and the physical test, Figure 6.8 shows the results of the models with α_R and β_R damping. As damping takes energy out of the system, the damped analysis reaches a lower maximum displacement. In Figure 6.8b, it is seen that the β_R damping already limits the displacement in the initial response. In contrast, the initial response of the α_R damped model is almost indistinguishable from the base model. Only as the moment of maximum displacement is reached, a clear damping effect is seen.

The decrease in displacement due to the added damping increases the discrepancy between the physical test and the numerical model in test 2. The added damping resulted in a similar change in response in test 3. However, as was shown in Figure 6.7, in test 3 the numerical base model overpredicted the displacement of the plate. Therefore, adding damping to the numerical model of test 3 reduces the discrepancy in response the of the numerical model.

The next two model variations are the model with the Lagrangian bird and the model where plastic material behaviour of the test rig is added. These are both shown in Figure 6.9, along with the base model and the physical test for comparison. One effect of using a Lagrangian bird model is seen directly after impact in Figure 6.9b. Instead of an immediate response, there is a slight delay, which resembles the physical test more closely. This is likely to be caused by the difference in geometry of both bird models. As was described in Section 2.4.2, the SPH bird model has a flattened front. This can lead to high initial peak pressures. Con-

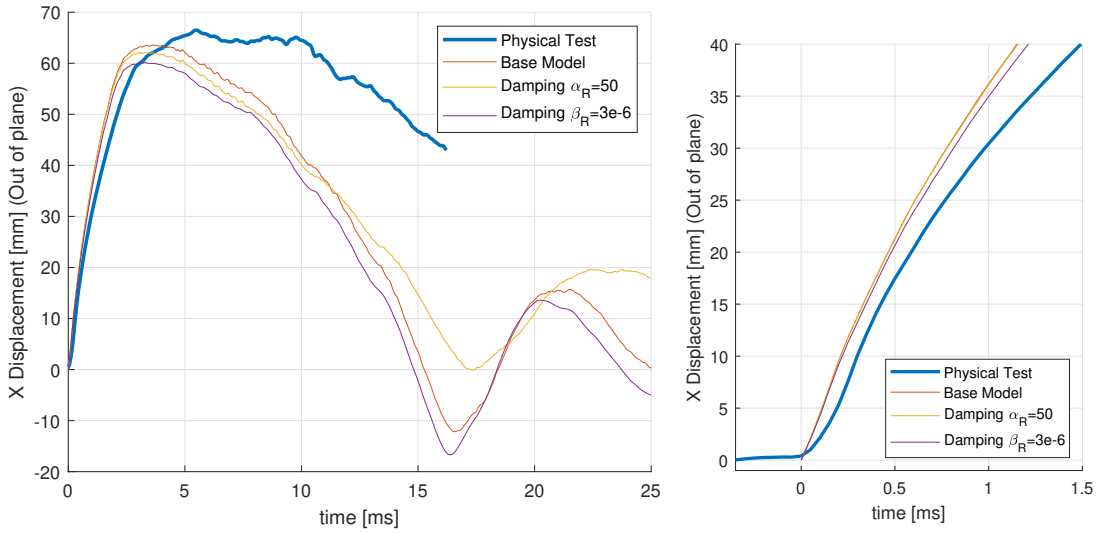

(a) *Overview.* ***(b)*** *Detailed view.*

Figure 6.8: *Out-of-plane displacement at the centre of impact of test 2 for different damping values.*

versely, the Lagrangian bird model has a more rounded front, leading to lower initial pressures and, thus, a delayed response. The rest of the response of the Lagrangian bird model variation is very similar to that of the base model. Only at t>17 ms the displacement start to slightly diverge.

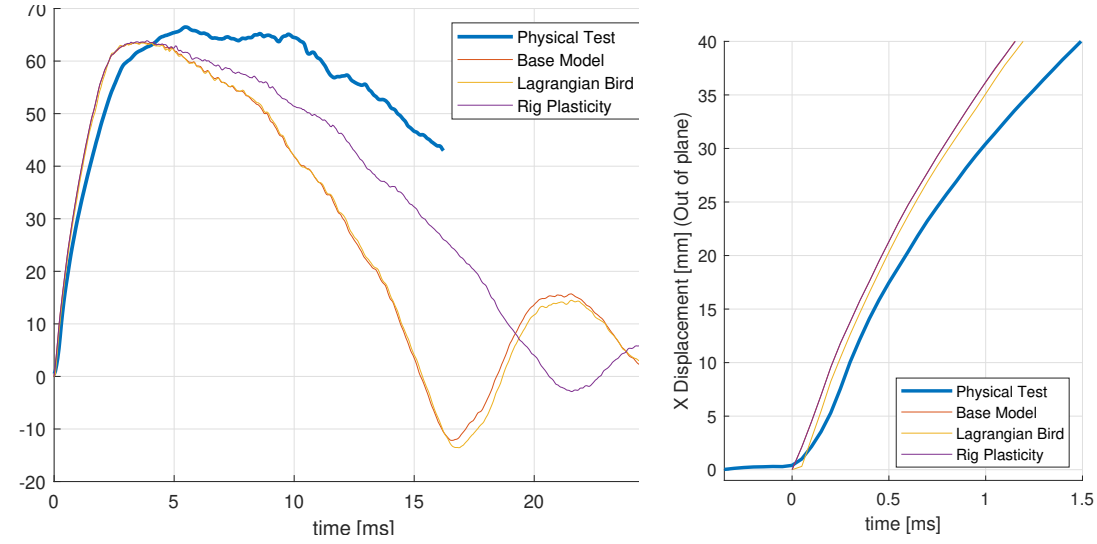

(a) *Overview.* ***(b)*** *Detailed view.*

Figure 6.9: *Out-of-plane displacement at the centre of impact of test 2 for the Lagrangian bird and the rig plasticity model variations.*

While the plasticity of the rig hardly influences the initial response, a great difference is seen in the bounce-back phase, when t>3 ms. This effect is much greater than expected, as it was first assumed that the steel rig would be too sturdy to be plastically deformed. The delayed bounce-back resembles the physical test much more closely.

In addition to being delayed, the magnitude of the bounce-back of the model with rig plasticity at t=21.5 ms is much smaller than that of the base model at t=16.5 ms. This could be caused by a loss of kinetic energy in the model, which is reduced due to the plastic de-

formation performed. This was checked by recording the total kinetic energy (ALLKE) in the base numerical model and the numerical model in which plasticity was added to the rig. Additionally, the energy dissipated by plastic deformation (ALLPD) was recorded. This showed that, at t=25 ms, the kinetic energy was 9% higher in the base model. The energy dissipated by plastic deformation was 18% higher in the model where plastic material behaviour was added to the rig.

Two contour plots of the equivalent plastic strain of the test rig at t=25 ms are shown in Figure 6.10. It is seen that at the bolts connecting the plate with the test rig, as well as the connections between different beams of the rig, plasticity does occur. This is expected to be caused by stress concentrations at these locations. This might indicate that plastic deformation of the rig does occur in the physical test as well. However, these locations were not closely inspected after the physical tests. Therefore, it is not known whether plastic deformation occurred there. If it did, it could have influenced tests 2-5, since the same test rig was reused for all tests.

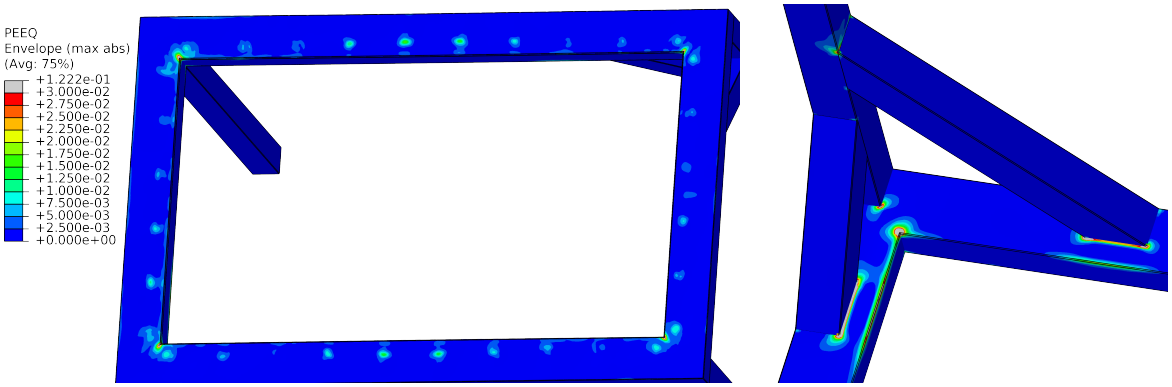

(a) *Front view.* ***(b)*** *Back view.*

Figure 6.10: *Contour plot of the equivalent plastic strain (PEEQ) of the test rig in the numerical model of test 2 at t=25 ms.*

Finally, the influence of the strain rate hardening effect is evaluated in Figure 6.11. This model was created by replacing the tabular material definition of the aluminium alloy plate with the Johnson-Cook material definition as described in Section 4.7. According to the Johnson-Cook material formulation of Equation (4.2), an increase in strain rate results in an increase of the yield stress. Therefore, an increased resistance to deformation would be expected when strain rate hardening is included in the numerical model. Figure 6.11 indeed shows that the material model that takes into account strain rate hardening results in a reduced displacement.

As described in Section 4.9, it is tested what the influence is of using different element types for the plate. In Figure 6.12, the resulting displacement at the centre of impact is shown for four different element types for test 3. In the base model, S4R conventional shell elements with a 5x5 mm mesh size are used, with only one element through the thickness. In the 'continuum shell elements' model, these S4R elements were replaced by SC8R continuum shells with the same mesh size. In the last two models shown, the plate is modelled with reduced integration (C3D8R) and full integration (C3D8) 3D elements. In these models, the mesh size was adjusted to have 3 elements through the thickness. To keep the aspect ratio of the elements close to 1, their in-plane dimension was also reduced, resulting in 1.5x1.5x1 mm elements.

The continuum shell model is seen to have an almost identical response as the base model. As the continuum shell element formulation is very similar to that of the conventional shell, this was to be expected. As was shown in Table 4.1, both shell elements calculate the stresses at 5 section points through the thickness and neglect the out of plane stresses. The main difference between the two element types is that, when using a conventional shell element,

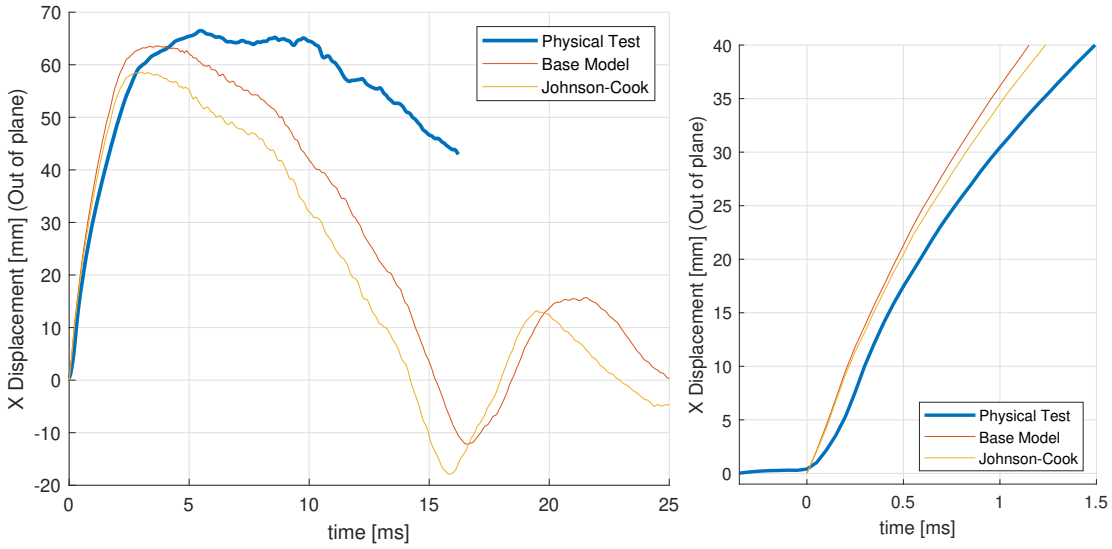

(a) *Overview.* **(b)** *Detailed view.*

Figure 6.11: *Out-of-plane displacement at the centre of impact of test 2 for the Johnson-Cook model variation.*

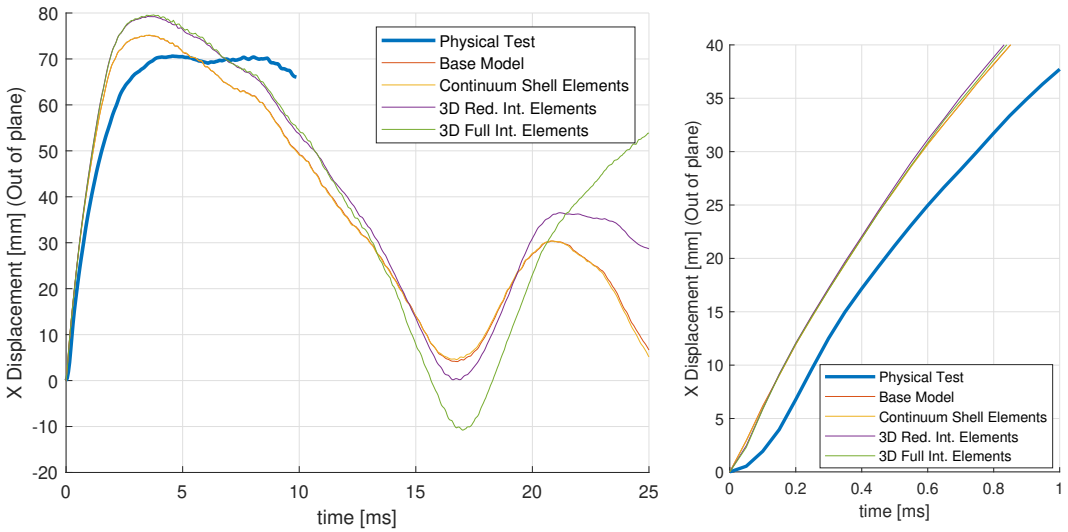

(a) *Overview.* **(b)** *Detailed view.*

Figure 6.12: *Out-of-plane displacement at the centre of impact of test 3 for the models with continuum shell, 3D reduced integration and 3D full integration plate elements.*

forces and moment are applied to the 4 nodes of the element. The continuum shell element has 8 nodes, to which only forces are applied and no moments. The results shown in Figure 6.12 show that this difference only has a very small effect on the resulting modelled response of the plate.

Figure 6.12 also shows that the more finely meshed 3D elements do not resist the impact as strongly as the shell elements, resulting in a larger maximum displacement. Both the elements with reduced and full integration show very similar behaviour. Only when t>11.5 ms, a clear difference between the response of these element types can be seen.

To be able to apply a modelling method in practice, not only the accuracy of the model, but also the computational efficiency is important. As the model used in this research is relatively small, the computational effort required to run the model is similarly small. However, this research is only preliminary. The end goal is that the same methods can, eventually, be

applied to real aircraft structures. These structures are often much larger and the computational effort required to run their models may form a constraint. Therefore, the computational effort required for each model is evaluated here.

As long as the hardware and settings used when running the numerical models is kept constant, the relative computational effort required for a numerical model can be expressed as the run time of the simulation. Running the exact same model twice can result in slightly different calculation times. This, however, only varies by a few percent. Therefore, these computation times give a good indication of the relative computational effort required by each numerical model. In Table 6.1, the relative calculation time required for each model variation is given. These results are normalised compared to the base model.

Table 6.1: *CPU calculation time for different numerical model variations of the flat plate, normalised to the base model.*

	Test 2	Test 3
Base model	1.00	1.00
Damping α_R	1.05	0.98
Damping β_R	25.63	25.22
Rig plasticity	1.05	1.02
Lagrangian bird	1.23	1.09
Strain rate hardening	1.02	-
3D full integration elements	-	27.09
3D reduced integration elements	-	24.07
Continuum shell elements	1.42	1.40

It is seen that adding the α_R damping, rig plasticity and Johnson-Cook material model all had a negligible effect on computation time required. Adding β_R damping resulted in a 25 fold increase in computational effort. The Lagrangian bird model gave a slight increase in the computational effort required. As discussed in Section 2.4.1, this is most likely due to high deformation of the finite elements in the bird and the resulting decrease in time step used.

The high increase in computational time required when using 3D elements has several contributing factors.

Firstly, each 3D element contains twice as many nodes as the conventional shell element. Additionally, use is made of the full 3D stress state instead of plane stress assumption. Secondly, for the full integration elements, the added number of integration points per element increases the required computational time. Additionally, as stated in Section 4.9, multiple elements are required through the thickness of the plate when using these elements. Therefore, the numerical model of the plate using 3D elements contained a much higher number of elements. Lastly, as described in Equation (2.23), the calculation time step is dependent on the minimum mesh size l_{min} present in the model. In the base model, all of the structure was modelled with an approximate mesh size of l=5 mm. To be able to accommodate the required geometry, in some locations smaller elements were used. This resulted in a minimum element length of l_{min} ≈2 mm. However, when using the 3D elements for the plate l_{min} reduced to 1 mm. This decreases the time step and therefore increases the required computational effort.

6.1.2. Stiffened plate response

The out-of-plane displacement at the centre of impact was plotted for stiffened panel test 4 in Figure 6.13. In this test, the bird impacted in between two stiffeners (see Figure 3.8), with a velocity V_{imp}=120.1 m/s. The point of maximum displacement in the DIC data is again assumed to coincide with the centre of impact. In the data of the numerical model, this point of maximum displacement and the centre of impact were confirmed to coincide.

As shown in Figure 6.13a, a maximum displacement of $\Delta X_{max,test}$=31.7 mm was recorded for physical test 4. The base model showed a maximum displacement of $X_{max,base}$=36.0 mm and

thus overestimated the test result with 13.6%. Between t=2.0 ms and t=2.8 ms, a small dip in displacement is seen in the numerical test result. This dip was not seen in the physical test.

Just as in the flat plate tests, Figure 6.13b shows an immediate response after impact for the numerical result and a delayed response for the physical test. This immediate response is most likely again caused by the flattened front of the SPH bird model, as described in Section 2.4.2.

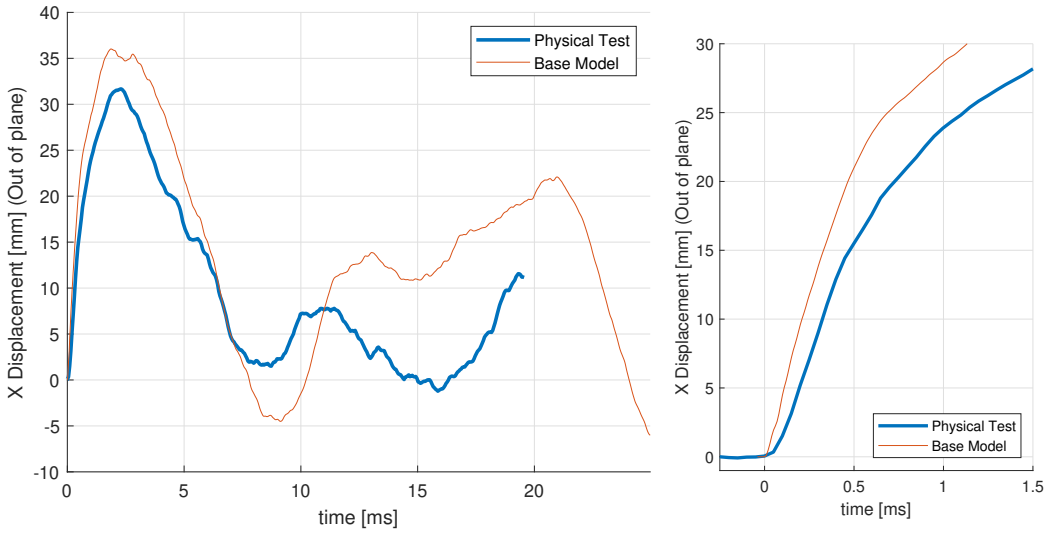

(a) *Overview.* ***(b)*** *Detailed view.*

Figure 6.13: *Out-of-plane displacement at the centre of impact of test 4 for the base model and the physical test.*

The out-of-plane displacement of impact test 4, based on the DIC data, is given in Figure 6.14 and compared to contour plots of the base model. It must be noted that the colours used to represent a specific displacement in the DIC data are not equivalent to those used in the base model. Therefore, care has to be taken when comparing these images. It is seen that large parts of the stiffened plate lack DIC data. At these locations the speckle pattern placed on the plate could not be seen clearly by both DIC cameras. This is mostly caused by the stiffeners when they obstruct the view of either of the two DIC cameras.

At t=1.0 ms, the result of the test and the model are closely correlated. The stiffeners are seen to distribute the deformations through the plate more quickly. Additionally, the stiffeners directly above and below the centre of impact are pushed away from the impact location. This causes a displacement wave to travel through these two stiffeners. In Figure 6.14d this wave is seen just before it reaches the stiffener intersections near accelerometer 3 (see Figure 3.8). When inspecting Figure 6.14c closely, this same phenomenon is seen in the physical test.

Observing the movement of the dummy mass and the mounting profile with which it is attached to the stiffened plate, a good agreement is found between test and model. Figure 6.14e shows that, at t=3 ms, the left and right side of the mounting profile have displaced by, approximately, 10 and 14 mm, respectively. Similar values are given by the numerical model. It is seen that DIC data is only available at a small part of the dummy mass. At t=3 ms, this location of the dummy mass does not yet show any displacement, which is also seen in the numerical model. Only when t=4 ms the mass is displaced by, approximately, 4 mm for both the impact test and the model.

A discrepancy between the test and the model can be seen in the flanges of the mounting profile, to the left of the dummy mass. At t=3 ms, Figure 6.14f shows excessive bending in these flanges. While some bending is also seen at this time in the physical test, the extent of this bending is much lower. Additionally, at t=4 ms, this bending has disappeared in

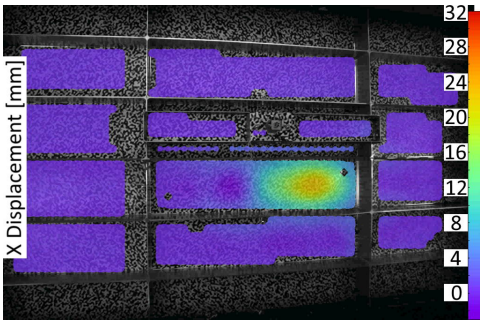

(a) *DIC, t=1.0 ms.*

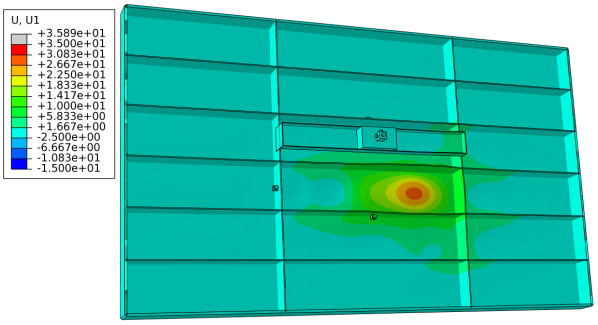

(b) *Base model, t=1.0 ms.*

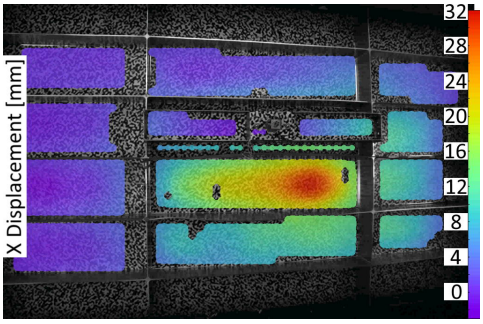

(c) *DIC, t=2.0 ms.*

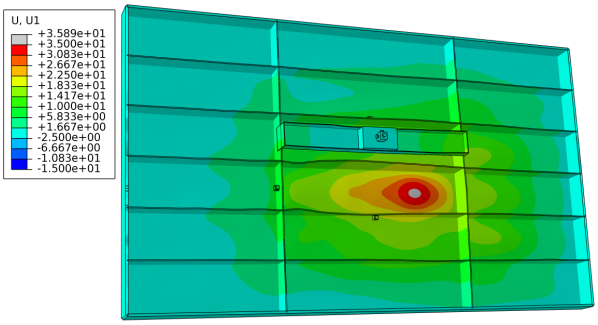

(d) *Base model, t=2.0 ms.*

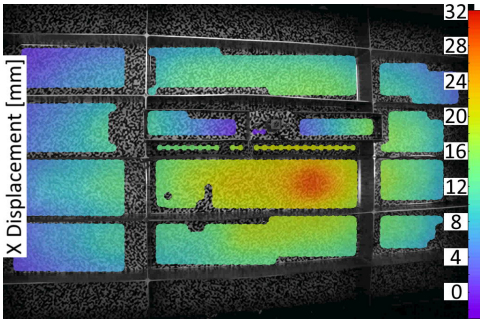

(e) *DIC, t=3.0 ms.*

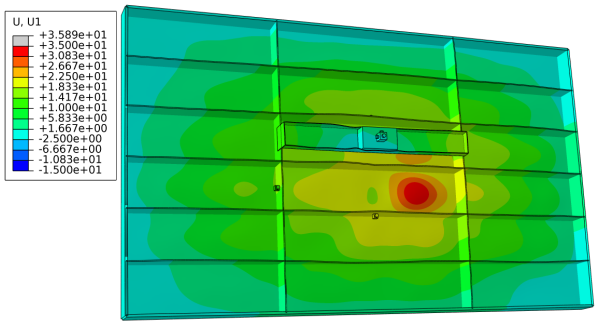

(f) *Base model, t=3.0 ms.*

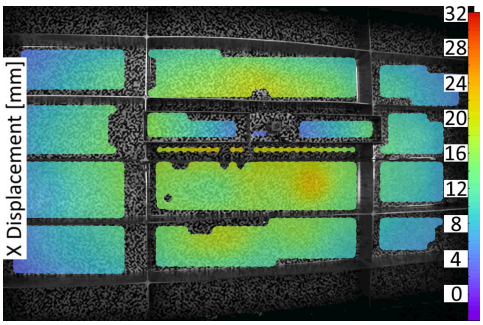

(g) *DIC, t=4.0 ms.*

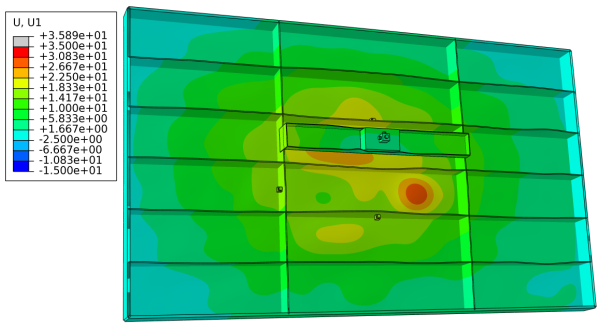

(h) *Base model, t=4.0 ms.*

Figure 6.14: *Comparison of the out-of-plane displacement of the impact test 4 and the base model, in millimetre.*

the physical test, while it remains in the numerical model. It is unknown what causes this bending behaviour.

The damped models of test 4 are compared to the physical test and the base model in Figure 6.15. The added damping results in a lower maximum displacement. Interestingly, the

model with α_R damping represents the behaviour of the physical test very well up to t=10 ms. Additionally, while the β_R damping increases the magnitude of the bounce-back at t=9 ms, the α_R damping reduces this bounce-back.

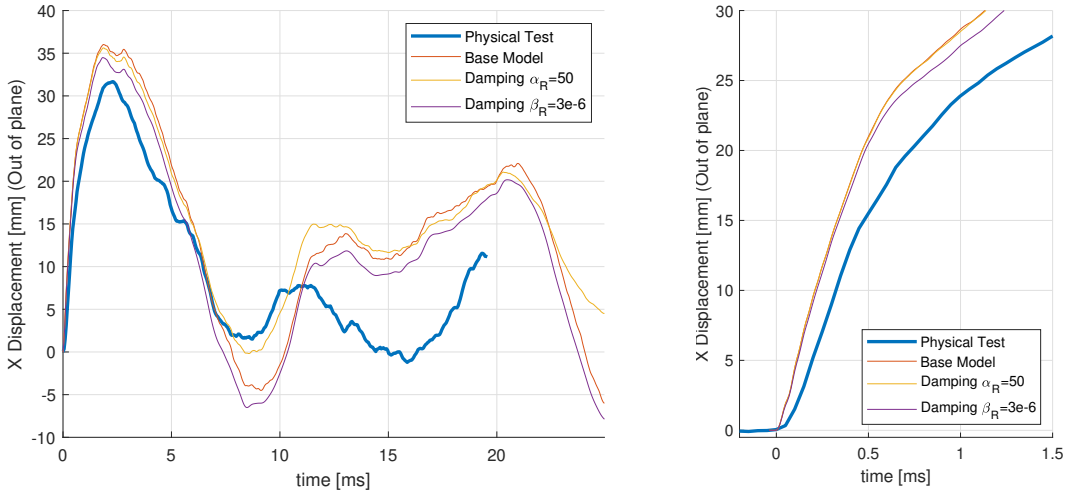

(a) *Overview.* ***(b)*** *Detailed view.*

Figure 6.15: *Out-of-plane displacement at the centre of impact of test 4 for different damping values.*

The influence of the plasticity of the test rig is shown in Figure 6.16. This shows that for the first 8 ms after impact the plasticity of the rig has very little influence. Between t=8 ms and t=11 ms, the result of the plastic test rig model represents the physical test more closely. After t=10 ms the results seem unclear.

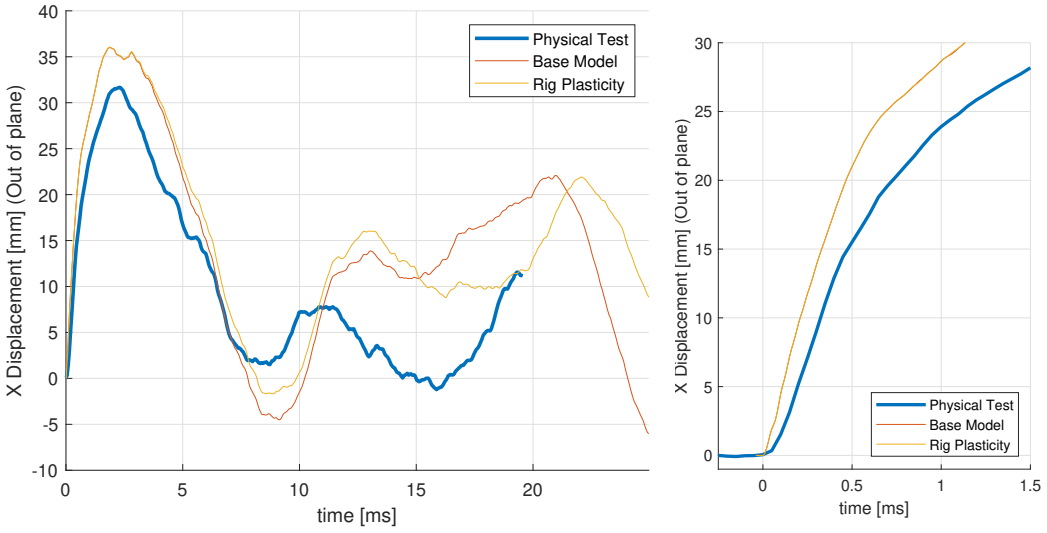

(a) *Overview.* ***(b)*** *Detailed view.*

Figure 6.16: *Out-of-plane displacement at the centre of impact of test 4 for the test rig with a plastic material definition.*

The displacement at the centre of impact for the stiffened plate modelled with 3D elements is shown in Figure 6.17a. For both models, the peak at t=2 ms is slightly higher than that of the base model. The response of the 'Full integration' model during the valley at t=7 until t=10 ms represents the physical test with great accuracy. However, while the physical test reaches a second peak already at t=10 ms, the 'Full integration' model keeps increasing up to t=12 ms.

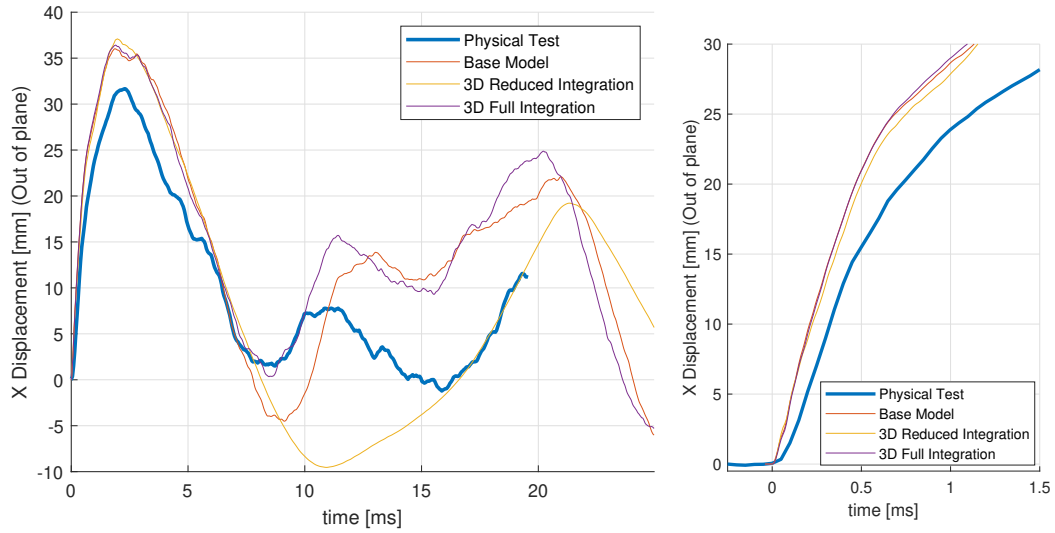

(a) *Overview.* ***(b)*** *Detailed view.*

Figure 6.17: *Out-of-plane displacement at the centre of impact of test 4 for the plate modelled with 3D elements.*

While the response of the model with 3D reduced integration elements is initially very similar to the base model, after t=8 ms the behaviour is unrepresentative of the physical test. In Table 4.3 it was discussed that using reduced integration elements leads to a risk of hourglassing of elements. One way to measure whether an excessive amount of hourglassing is present is to look at the artificial strain energy (ALLAE) in the model. This is an artificial form of energy "associated with constraints used to remove singular modes (such as hourglass control)" [25]. When the artificial energy in the simulation is high compared to the internal energy, this is a strong indication of severe hourglassing. Figure 6.18 shows the artificial and internal energy of the structure in the base model and the 3D reduced integration elements model. These images show that little hourglassing occurs in the base model. However, the high artificial energy in Figure 6.18b indicates that there is likely an excessive amount of hourglassing in the model with 3D reduced integration elements.

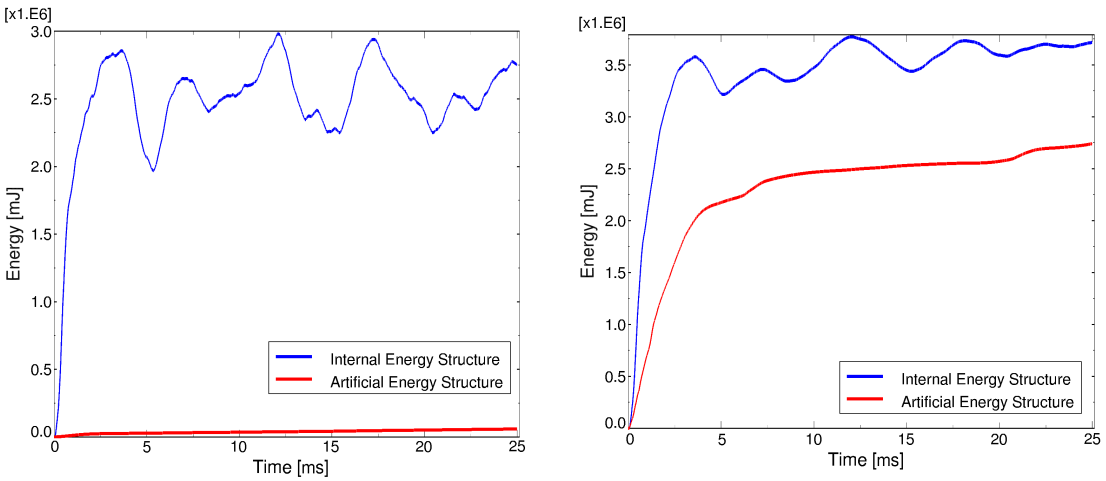

(a) *Base model.* ***(b)*** *3D reduced integration model.*

Figure 6.18: *Internal and artificial energy in the base model and the 3D reduced integration elements model of test 4.*

For impact test 5, no displacement data was available at the centre of impact. In this test, the impact occurred exactly at a crossing of two stiffeners. As was shown before in Figure 6.14,

at this location there is a lack of displacement data due to limitations in the DIC installation. It was attempted to compare the displacement at different locations instead. This, however, was problematic as it was difficult to make sure exactly the same location would be used in the physical test and the numerical model.

As for the flat plate, the relative computational effort required for each model is compared. The effect of different model variations on computational time in the stiffened plate model is seen to be mostly similar as with the flat plate model. Their calculation times are given in Table 6.2. The α_R damping, rig plasticity and Lagrangian bird model all have a minor effect on the calculation time. The β_R damped model required over 19 times more computational time than the base model.

Table 6.2: *CPU calculation time for different numerical model variations of the stiffened plate, normalised to the base model.*

	Test 4	Test 5
Base model	1.00	1.00
Damping α_R	1.02	1.05
Damping β_R	19.14	19.79
Rig plasticity	1.03	-
3D full integration elements	2.45	2.53
3D reduced integration elements	1.70	1.79

The increase in computational time needed for the numerical models using 3D elements for the plate was much less severe than in the flat plate models. This is most likely because in the stiffened plate model only one element was used through the thickness of the plate and the stiffeners. Therefore, the increase in the number of elements compared to the base model is very limited and was only seen at the intersections of the stiffeners and the plate.

6.2. Stress wave propagation

As explained in Section 2.6, there are several types of stress waves that propagate in a plate when impacted. In this section, the propagation of the in-plane and out-of-plane waves are evaluated. The results for the physical tests are described in Section 6.2.1. Secondly, in Section 6.2.2 the wave speeds are determined for the simplified plate using the method described in Section 5.1. This is followed by a qualitative evaluation of the propagating waves in the simplified plate in Section 6.2.3. Lastly, the propagation of the waves in the flat and stiffened plates are evaluated qualitatively in Section 6.2.4.

6.2.1. Physical tests

As described in Section 5.1, for the flat plate physical tests, DIC is used to measure the wave propagation velocity. For test 2, Figures 6.19a and 6.19b give the x- (out-of-plane) and y-displacement (longitudinal) over time for different y positions, respectively. Here, all the shown positions are located on the same vertically centred cross-section as was shown in Figure 6.3. The intervals between the y positions are not as evenly spaced as in the results of the numerical model in Figure 6.2, because the positions were dependent on those available in the DIC data. Additionally, only displacements at negative y positions are shown. This is done because on the +y side the dummy mass disturbs the propagating waves and the DIC measurement of the plate.

What can be noticed in both graphs of Figure 6.19 is that at t=0 ms the displacement at all the y positions is non-zero, while before impact there should be no displacement of the plate yet. As explained in Section 6.1, this may be caused by errors in the DIC data, the airflow ahead of the bird or other environmental disturbances. This leads to problems in the determination of the wave propagation velocities. The technique described in Section 5.1 relies on registering a stress wave to have reached a certain distance when the material at that distance is displaced by more than the threshold value. As the DIC data already shows

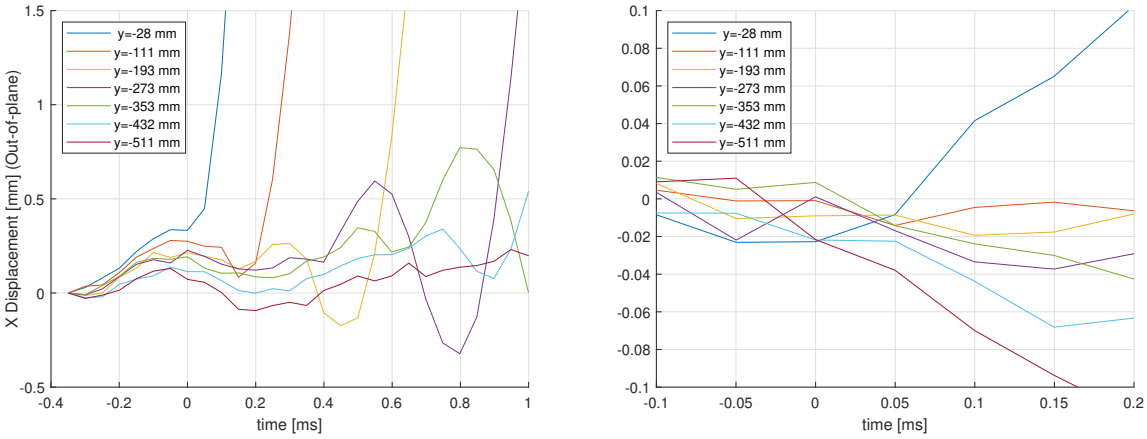

(a) *Out-of-plane displacement.*

(b) *Longitudinal displacement.*

Figure 6.19: *The displacement of physical test 2 at several locations on the plate centreline at distances y from the centre of impact.*

a displacement before impact, the wave propagation velocity cannot be determined with a low threshold value.

Using a high threshold value would not measure the stress waves. Instead, it would indicate how quickly a large displacement propagates outward. Using a threshold value of 1 mm for the out-of-plane wave in test 2 shown in Figure 6.19a and measuring the wave from y_1=-28 mm to y_2=-273 mm gives t_1=0.088 ms and t_2=0.939 ms. Since the bird impacts at y=0 mm, y_1 and y_2 are analogous to r_1 and r_2 in Equation (5.1). Using Equation (5.1) this results in a recorded wave speed V_{rec}=288 m/s. It is unclear whether this could be a low frequency flexural wave. If so, using Equation (2.29) and solving for ω, this would indicate that this is a flexural wave with $\omega \approx$8.4 kHz.

To determine the longitudinal wave propagation velocity, the y-displacements on the horizontal cross-section of the plate must be evaluated. From Table 2.1 it is known that the longitudinal stress wave should have a velocity c_L=5.42 km/s in the aluminium alloy plate used. With a distance of 511 mm from the centre of impact to the furthest node, this takes approximately 0.1 ms. Therefore, only a short time span is shown in Figure 6.19b. The longitudinal wave could not be identified from the DIC data captured. This is influenced by 2 factors. Firstly, the DIC cameras have a frequency of 20000 frames per second. Therefore, it would only take 3 frames from the moment of impact until y=-511 mm is reached by the longitudinal wave. This provides very limited detail and insight on how the plate is displaced in this short amount of time. Secondly, the theory described in Section 2.6 does not describe the magnitude of the displacements caused by stress waves. If this magnitude is smaller than the disturbances affecting the plate, the effect of the longitudinal stress wave would be drowned out by these disturbances. As will be investigated further in Section 6.2.2, the displacements due to the longitudinal stress waves in the simplified plate are on the order of 10^{-3} or smaller. This would indicate that the effect of disturbances, seen in Figure 6.19b even before impact, is much larger than that of the longitudinal wave itself. Thus, indeed the test setup used is not able to identify the longitudinal stress wave.

6.2.2. Recorded wave speed velocities in the simplified plate model

As described in Section 4.10, the simplified plate was created to determine the stress wave speeds without the influence of reflections or boundaries. Figure 6.20 shows the longitudinal (dashed line) and out-of-plane (solid line) wave speed as a function of the threshold value. This is the average wave velocity while it travels from r_1=250 mm to r_2=1000 mm from the impact centre, located along the mesh direction, as shown in Figure 4.13. The longitudinal and Rayleigh stress wave velocities given by Equations (2.27) and (2.31), respectively, are

shown in the figure for reference. Note that the scale on the x-axis is given logarithmically and varies from 10^{-0} to 10^{-25}. The first shown wave speeds are given for a threshold value of 10^{-1} and 10^{-3} for the longitudinal and out-of-plane wave, respectively. This is because for larger threshold values, the node at 1000 mm from the impact centre has displaced by a smaller magnitude than the threshold value at the end of the simulation run time. Thus, the wave is not registered to have reached the second node yet. Therefore, no average wave speed between the two measurement nodes can be given for large threshold values. If the run time were to be increased, wave velocity values for larger threshold values would likely also be found.

Figure 6.20 shows the recorded wave speeds V_{rec} for the large plate with exactly the same material properties and thickness as the flat plate from Section 3.2. To determine the influence of mesh size on the wave speed, mesh sizes of 1.25, 2.50 and 5.00 mm are compared in Figure 6.20. As expected, the wave speed increases as the threshold value decreases. The recorded longitudinal wave speed first quickly rises before it reaches a relatively constant value for threshold values of 10^{-3} and lower. This constant value is relatively close to the theoretical longitudinal wave velocity c_L. Therefore, it seems like a strong indication that this displacement is caused by the longitudinal wave. Figure 6.20 also shows that the recorded longitudinal wave speed becomes lower as the mesh is refined. With this lowering, it approaches the theoretical value more closely. This effect increases as the used threshold value decreases.

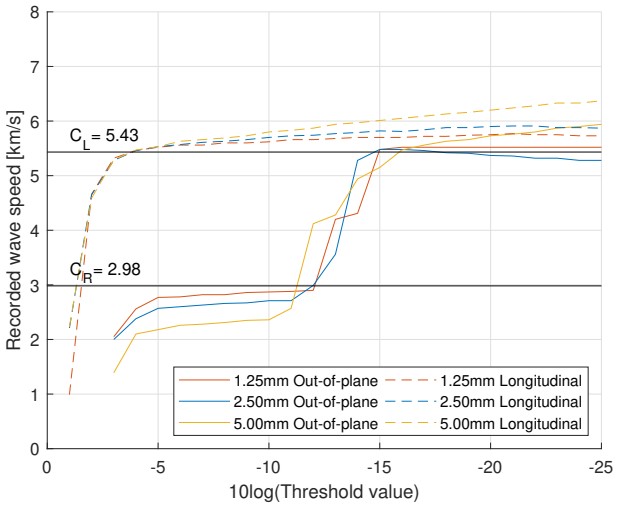

Figure 6.20: *Recorded longitudinal and out-of-plane wave speed as a function of threshold value. Comparison of results using 1.25, 2.50 and 5.00 mm element sizes.*

In addition to the longitudinal wave speed, Figure 6.20 also shows the recorded out-of-plane wave speed. A low recorded wave speed zone is seen from a threshold value between 10^{-4} and 10^{-11}. In this range, the wave speed varies from 2.6 to 2.9 km/s, respectively, when using a 1.25 mm element size. This is followed by a transition zone up to a threshold value of 10^{-15} and ending in a second constant plateau with a wave speed of, approximately, 5.5 km/s.

Since both the Rayleigh wave and the flexural wave evoke an out-of-plane displacement, it is challenging to distinguish between them. Additionally, due to the way in which the numerical model is built up, several limitations apply to both these wave types. Firstly, in the described theory, the Rayleigh wave only propagates along the surface of the plate and damps out deeper into the plate. However, as the plate was only modelled with one shell element through the thickness, no clear distinction can be made between the plate surface and the centre of the plate. Therefore, it was not known whether the numerical model was capable of modelling the Rayleigh waves. Secondly, the flexural waves are dispersive and thus their velocity varies

based on their frequency. Therefore, a one to one comparison between the theoretical and the recorded wave speed, as was done for the longitudinal wave, can not be made for the flexural wave.

As the flexural wave speed is dependent on wave frequency it has no constant value. However, using Equation (2.29), the theoretical wave speed at different frequencies can be compared to the recorded wave speeds in Figure 6.20. It is seen that, before the transition zone, the recorded out-of-plane wave speed lies between 2.2 and 2.4 km/s when using a 5 mm mesh size. For a 1.25 mm mesh size the recorded out-of-plane wave speed is 2.6 to 2.9 km/s. If this out-of-plane displacement is caused by the propagation of a flexural wave, this would indicate a wave frequency of approximately 500 and 800 kHz, respectively. As determined using Equation (4.12), this corresponds to a wavelength of 4.4 and 3.5 mm when using a mesh size of 5.00 and 1.25 mm, respectively. In both cases, this would cause the wave to be represented by much less than the 8 nodes per wavelength recommended by ESA [66]. Thus, these high frequency flexural waves would not be represented accurately in this finite element model. Therefore, the recorded wave speed is likely not caused by the flexural wave.

Instead, the recorded out-of-plane wave speed may be the result of a Rayleigh wave. The recorded out-of-plane wave speed varies from 2.6 to 2.9 km/s. With a Rayleigh wave velocity of 2.98 km/s this lies within 13% to 3% of the theoretical Rayleigh wave velocity.

When using a threshold value smaller than 10^{-11}, the recorded out-of-plane wave speed increases and approaches that of the longitudinal wave. It is suspected that this is not caused by any low amplitude out-of-plane waves. Instead, it might be caused by the longitudinal wave. Theoretically, the longitudinal wave only causes an in-plane displacement. However, as the loading of the plate is in the out-of-plane direction, the longitudinal wave might not remain perfectly in-plane either. Therefore, the longitudinal wave possibly creates, in addition to the in-plane displacement, a slight out-of-plane displacement. This out-of-plane movement would be registered as a propagating out-of-plane wave when using a low threshold value, even though this is only a secondary effect of the longitudinal wave.

Comparing the recorded longitudinal waves in the finite element model with the physical tests also gives an indication of why the stress waves could not be detected using the DIC data. For the longitudinal stress wave, the threshold value required to register the wave with a speed close to the theoretical value is 10^{-3} or smaller. This means that the amplitude of the wave that is registered is on the order of 0.001 mm. In Figure 6.19, it can be seen that the influence of other disturbances, even before impact, is much larger than this. Therefore, the effect of the stress wave front is drowned out by the other disturbances and the stress wave velocity cannot be measured.

In Figure 6.20, the theoretical wave speeds were compared to those found in the numerical model when using an elastoplastic material definition. However, in the determination of the theoretical wave speed velocities only elastic material behaviour was assumed. Therefore, to investigate the influence of plasticity, the simplified plate model was adjusted such that the plate only has its elastic behaviour defined. The recorded wave speed results of the elastic and elastoplastic simplified plate models, using a 2.50 mm element size, are compared in Figure 6.21. It is seen that the effect of plasticity on the recorded longitudinal wave speed is almost unperceivable. For the out-of-plane wave, only a slight difference due to the plasticity is seen at a threshold value of 10^{-3} and 10^{-4}, as well as in the transition zone after 10^{-12}.

The sensitivity of the wave propagation speed to the impact velocity V_{imp} of the bird was also investigated. Figure 6.22a compares the standard model with V_{imp}=120 m/s to that with an adjusted impact velocity of V_{imp}=90 m/s and V_{imp}=150 m/s. The wave speed equations in Section 2.6 do not depend on impact velocity. Additionally, impact velocity was not a factor in the derivation of these equations. Therefore, it was expected that the impact velocity would not influence the recorded wave speed in the numerical model. The results in Figure 6.22a also do not show a dependency on impact velocity. For the longitudinal wave, only a slight discrepancy can be seen for threshold values bigger than 10^{-4}, but once the plateau is reached, the wave propagation velocities are nearly identical for different values of

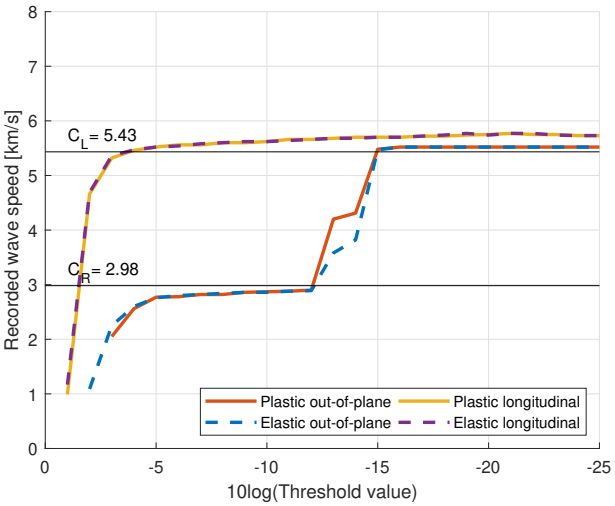

Figure 6.21: *Recorded longitudinal and out-of-plane wave speed as a function of threshold value. Comparison of purely elastic and elastoplastic material definitions.*

V_{imp}. Similarly, the recorded out-of-plane wave speed only shows some discrepancy once the transition zone sets in.

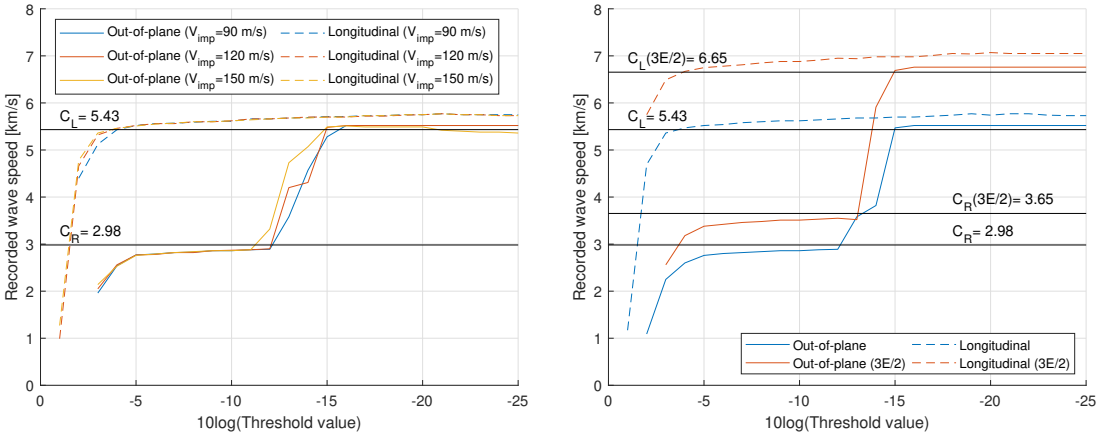

(a) *Varying impact velocities (V_{imp}).* ***(b)*** *Varying Young's modulus (E).*

Figure 6.22: *Recorded longitudinal and out-of-plane wave speed as a function of threshold value. Comparison of varying bird impact velocities and Young's modulus.*

The last model sensitivity tested for the simplified plate was the sensitivity to the Young's modulus E of the plate. Wave speed equations Equations (2.27), (2.29) and (2.31) show that the theoretical wave speeds are directly proportional to $\sqrt{E}$. To test whether this holds true for the numerical model, the model with an elastic material definition only is used. A variation to this model was created with the Young's modulus adjusted by a factor $3/2$. The recorded wave speed velocities for these models are shown in Figure 6.22b. In this figure also the adjusted theoretical wave speeds are shown. It is seen that both the recorded longitudinal and out-of-plane wave speeds correctly scale with the square root of the Young's modulus.

6.2.3. Qualitative evaluation of the simplified plate

Section 6.2.2 only evaluates the recorded wave speed along the line shown in Figure 4.13, which aligns with the mesh. To qualitatively evaluate the dependency on meshing direction a different approach is taken. In Figure 6.23 the out-of-plane displacement over the entire

simplified plate is shown. The black and grey area indicate that the out-of-plane displacement of the plate exceeds the threshold value. A threshold value of 10^{-6} (left) and 10^{-10} (right) was used. The simplified plate model used is that with a 2.50 mm element size, V_{imp}=120 m/s and the material model which includes plasticity.

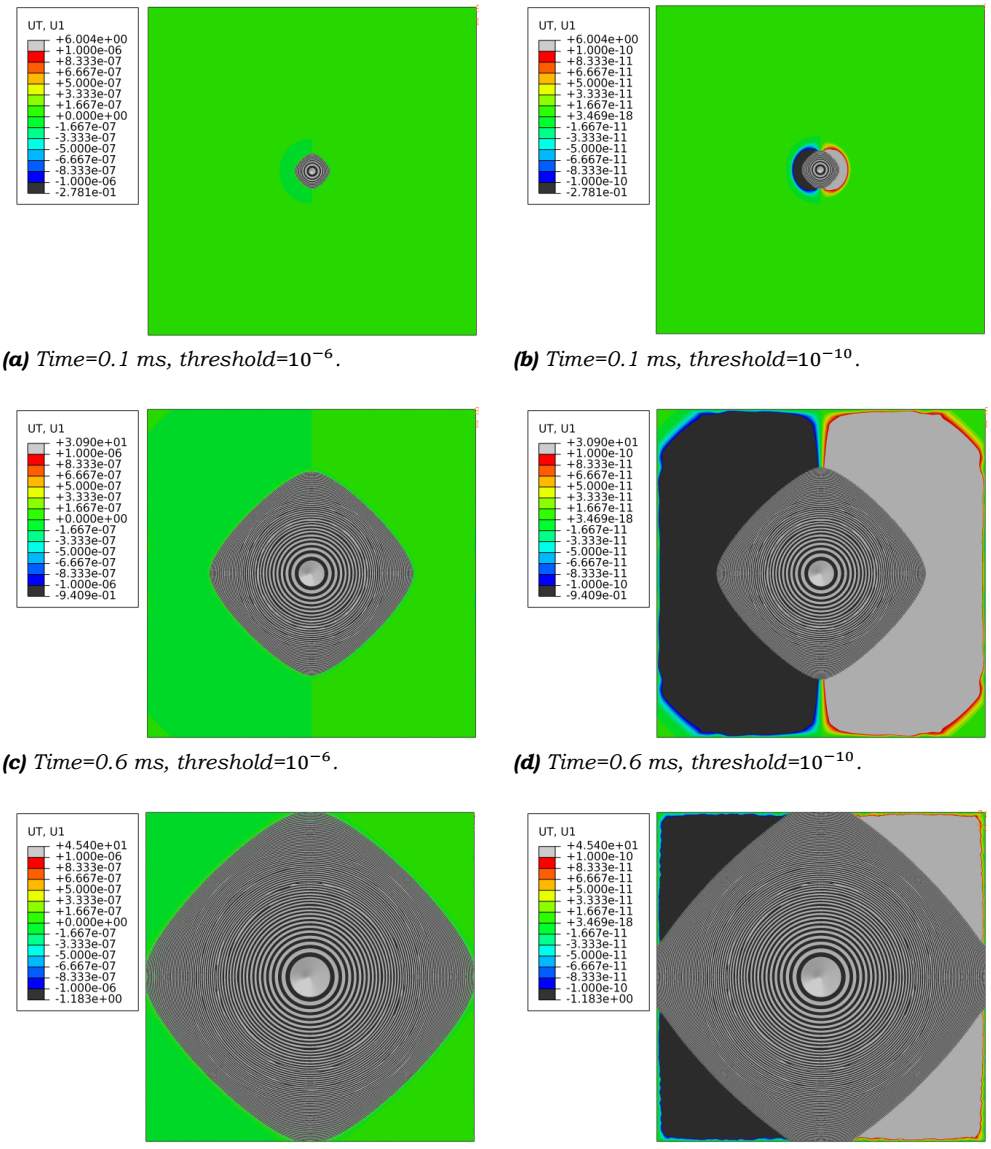

(a) *Time=0.1 ms, threshold=*10^{-6}.

(b) *Time=0.1 ms, threshold=*10^{-10}.

(c) *Time=0.6 ms, threshold=*10^{-6}.

(d) *Time=0.6 ms, threshold=*10^{-10}.

(e) *Time=1.0 ms, threshold=*10^{-6}.

(f) *Time=1.0 ms, threshold=*10^{-10}.

Figure 6.23: *Out-of-plane displacement of the simplified plate, meshed with 2.50 mm elements, at varying moments after impact, for different threshold values.*

With this visualisation, a change in out-of-plane wave speed is seen depending on meshing direction. The wave travels much further and thus faster parallel to the meshing direction than diagonally. This leads to the rounded square shape. Due to time constraints, the method described in Section 5.1 was not used for the wave propagation diagonal to the mesh. However, from the images in Figure 6.23, an estimation was made to compare the wave velocities parallel and diagonally to the mesh. A difference in the out-of-plane wave propagation velocity of approximately 17% was found for the wave travelling from t=0 to t=0.9ms.

One possible cause of this mesh dependency can be found in the filtering behaviour described in Section 4.10. As a wave of a specific wavelength propagates diagonally to the mesh, it is represented by fewer nodes than if that same wave would be travelling tangentially to the

mesh. This could hinder the propagation of short wavelength, high frequency, higher velocity flexural waves.

The images on the right in Figure 6.23 use a threshold value of 10^{-10}. A large extra area exceeds this lower threshold value on both the left and right side of the rounded square at the centre. On the right side of the plate, the plate is displaced slightly in the direction of flight of the bird. On the left, a slight displacement in the opposite direction is seen. As the model was symmetric in both horizontal and vertical direction it is not clear what causes this asymmetry.

Additionally, to determine the wave speed in Section 6.2.2, the displacements were only recorded at a line extending upward from the centre of impact, tangentially to the mesh. It was assumed that, due to symmetry, the resulting wave speed would be identical as to when it would be determined using a line extending horizontally from the centre of impact. However, Figure 6.23 shows that this assumption is false when using a small threshold value.

6.2.4. Flat and stiffened plate

To qualitatively assess how the stress waves propagate through the flat and stiffened plates, a contour plot of their displacement is given. Figure 6.24 shows the y-displacement (left) and out-of-plane displacement (right) of the numerical model of test 2 for t=0.12 and t=0.20 ms after impact. A threshold value of 10^{-6} is used. As Figures 6.24a and 6.24c plot the y-displacement, they indicate how far the in-plane longitudinal wave has travelled at their specific moments after impact. It shows that, contrary to the out-of-plane wave, no mesh dependency is seen. The in-plane wave propagates in all directions with the same velocity.

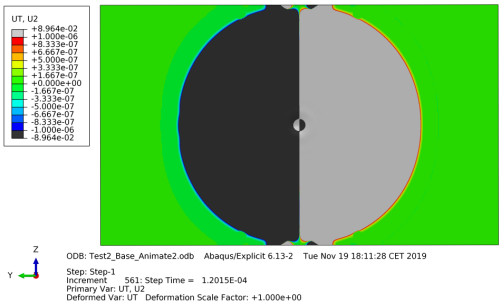

(a) *Time=0.12 ms, y-displacement.*

(b) *Time=0.12 ms, out-of-plane.*

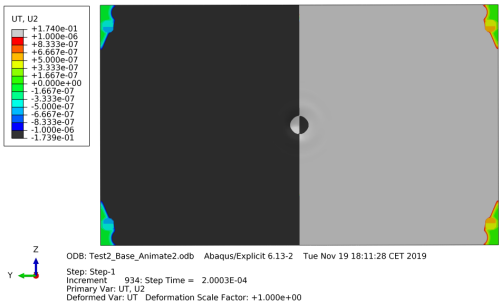

(c) *Time=0.20 ms, y-displacement.*

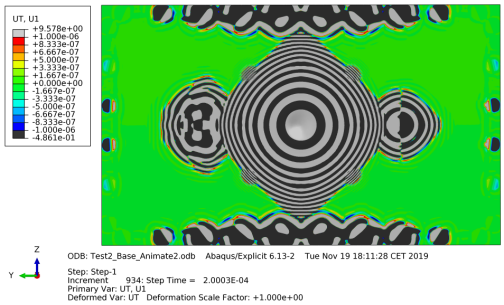

(d) *Time=0.20 ms, out-of-plane.*

Figure 6.24: *Displacement of the flat plate in test 2, for a threshold value of* 10^{-6}.

Additionally, Figure 6.24 shows how the interaction of the in-plane wave with obstructions results in out-of-plane motion. Figure 6.24a shows the moment the longitudinal wave passes accelerometer 1, 5 and the dummy mass. At this same moment, Figure 6.24b shows how the longitudinal wave is reflected in out-of-plane direction upon interacting with these objects. A similar effect is seen in Figure 6.24d at the boundaries of the plate. The reflection of the in-plane wave when hitting the fasteners results in out-of-plane reflections.

This also clearly indicates why it would have been difficult to determine the out-of-plane wave speed velocity using the method described in Section 5.1 for a plate with complexities such as the dummy mass. If the second node in Equation (5.1) would be positioned at a distance r_2 that is near the dummy mass or the plate boundary, it would register the reflections of this dummy mass or boundary instead of the wave that propagates from the centre of impact. This would result in an erroneous wave speed determination.

Similar contour plots are given of the stiffened plate of test 4 in Figure 6.25. Only the frontal area of the stiffened plate is shown and not the stiffeners. Figures 6.25a and 6.25c show that the in-plane wave is not noticeably influenced by the presence of the stiffeners. In Figures 6.25b and 6.25d, the interaction of the stiffeners with the propagating in-plane wave is seen. This interaction causes out-of-plane displacements to reflect off of these stiffeners.

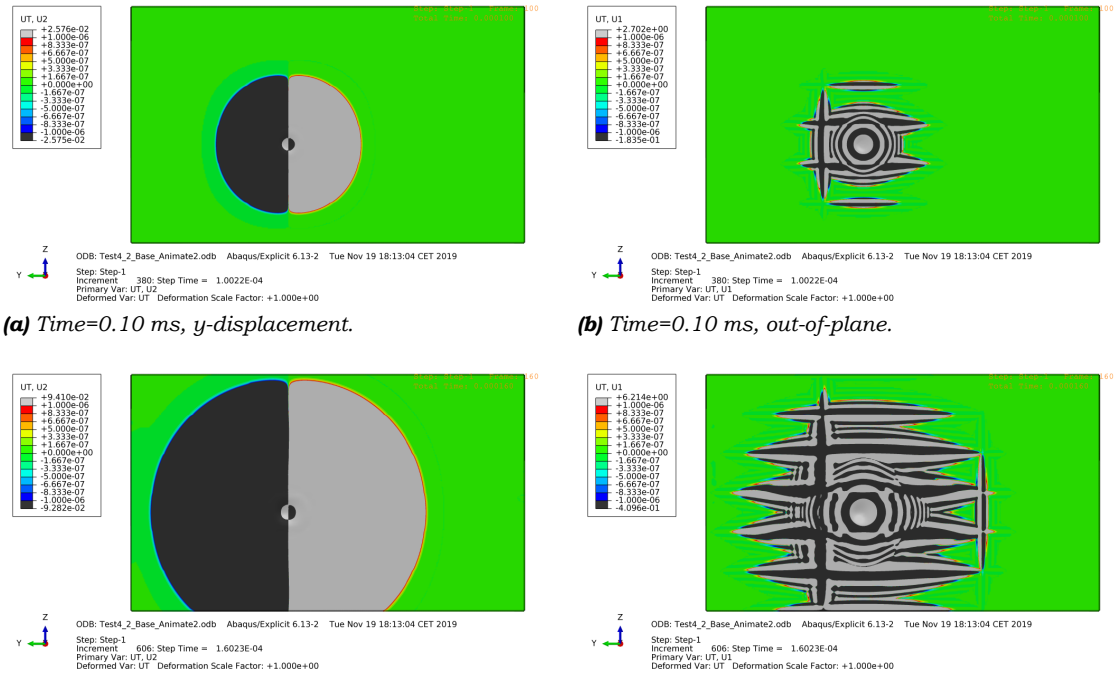

(a) *Time=0.10 ms, y-displacement.*

(b) *Time=0.10 ms, out-of-plane.*

(c) *Time=0.16 ms, y-displacement.*

(d) *Time=0.16 ms, out-of-plane.*

Figure 6.25: *Displacement of the stiffened plate in test 4, for a threshold value of* 10^{-6}.

6.3. Shock response spectrum

In this section, the accuracy of the numerically simulated vibratory response of the plate and the dummy mass is assessed. This is done using shock response spectra, which were generated using the acceleration data from the accelerometers using the method described in Section 5.1. Firstly, the vibratory response of the flat plate is discussed in Section 6.3.1. In this section, a different way to visualise the discrepancy of the shock response spectra of the numerical model compared to the physical test is also discussed. In Section 6.3.2, the shock response spectra of the stiffened plate are evaluated.

6.3.1. Flat plate vibratory response

To compare the vibratory response of the numerical base model to that of the physical test 2, the shock response spectra of accelerometer 1, 2 and 5 are given in Figure 6.26. These are the accelerometers under the dummy mass, on top of the dummy mass and on the other side of the plate, respectively. The discrepancy between the peak acceleration of the physical test and the numerical model at a specific natural frequency is quantified as the error E. The error E is given in decibels, as calculated by Equation (6.1).

$$\mathrm{E} = 20 * 10log\left(\frac{\text{SRS Peak acceleration of numerical model}}{\text{SRS Peak acceleration of physical test}}\right) \tag{6.1}$$

In the figures, a 6 dB error margin is given around the physical test results. Zhao et al. [74] use such a 6 dB error margin to determine if the numerical results represent the physical tests with sufficient accuracy. Equation (6.1) indicates that a +6 dB error E corresponds to a twofold overestimation of the peak acceleration. A -6 dB error indicates an underestimation of the peak acceleration by half. The shock response spectra of both accelerometer 1 and 2 fall mostly within this error margin. The numerical model thus seems to be able to determine the severity of the vibratory response at these locations well. However, at a few natural frequencies this 6 dB error is exceeded. In Figure 6.26a this is seen at f_n=120 Hz, f_n=700 Hz and f_n>4 kHz.

The SRS of accelerometer 5 in Figure 6.26c shows a larger discrepancy between physical and numerical test data. Especially at low natural frequencies, a large deviation is seen.

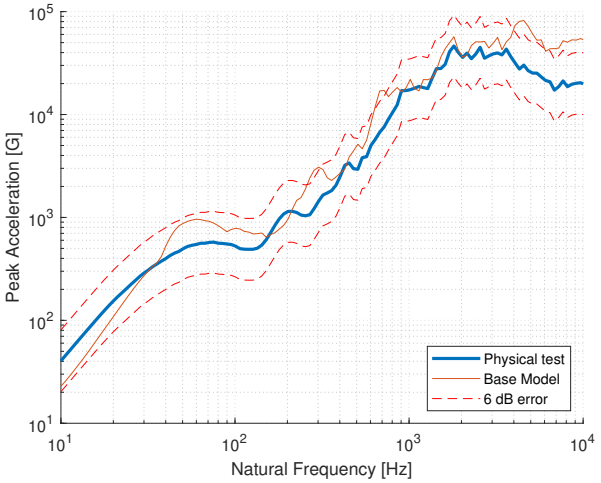

(a) *Test 2, Accelerometer 1.*

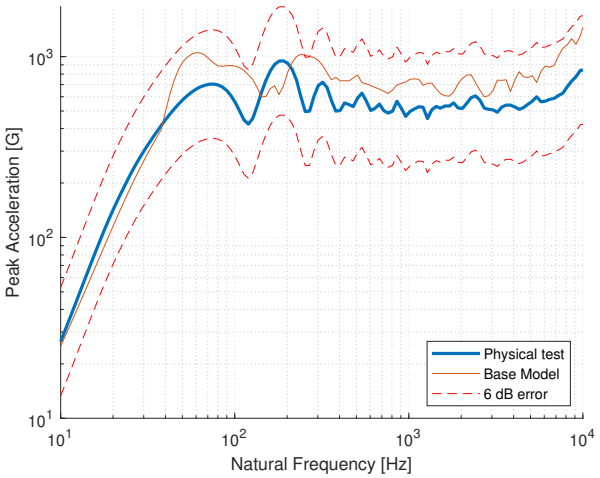

(b) *Test 2, Accelerometer 2.*

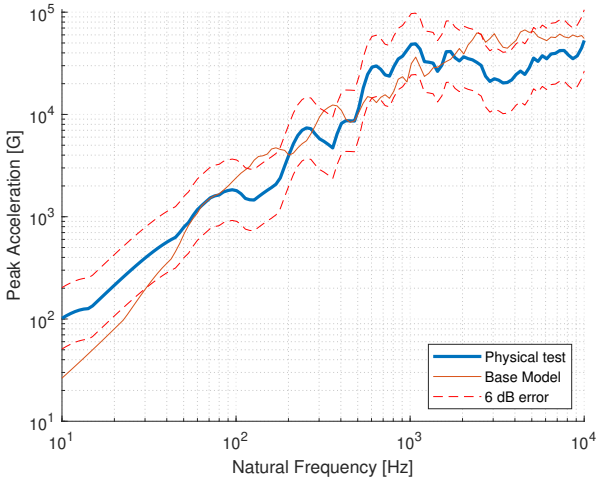

(c) *Test 2, Accelerometer 5.*

Figure 6.26: *Shock response spectra of test 2, with Q=10. A comparison of the base numerical model to the physical test.*

The maximum errors of the numerical model are important when a numerical model is used to determine the severity of a vibration. To derive the shock specification from the SRS using the method described in Section 5.2.3 these maximum errors need to be taken into account.

If the model overestimates the peak accelerations experienced at that location (E>0 dB) the shock specification will be too strict. If the model underestimates the peak accelerations (E<0 dB) this needs to be known and taken into account with an increased safety margin. If not, this would lead to an unconservative shock specification.

To better understand the variations in the error of the numerical model, the results will be visualised in a different way. Figure 6.27 shows error bar graphs of the shock response spectra of test 2 and test 3. Such an error bar graph displays the variation in the discrepancy between the numerical model SRS and the SRS of the physical test. In this figure, the natural frequency range is divided into three parts. This is done because the accuracy of the model might differ at varying natural frequencies. These natural frequency ranges consist of the low (10-100 Hz), medium (100-1000 Hz) and high (1-10 kHz) frequency ranges denoted by A, B and C on the horizontal axis. The numbers on the horizontal axis denote the location of the accelerometer as given in Chapter 3. The error-bar graphs give a clear overview of both the maximum positive and negative discrepancy per natural frequency range.

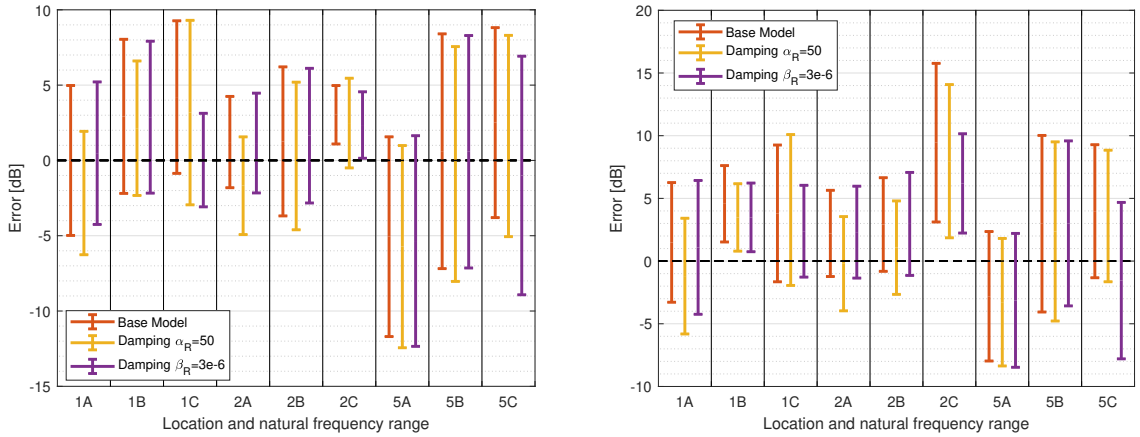

(a) *Test 2.* ***(b)*** *Test 3.*

Figure 6.27: *Discrepancy range between the SRS of the physical test and the numerical model for the flat plates. A comparison of the base and damped models. A, B and C denote the frequency range 10-100, 100-1000 and 1000-10000 Hz respectively.*

To clarify, two examples will be given. Firstly, Figure 6.27a shows that in test 2, at accelerometer 2, in the 10-100 Hz natural frequency range (column 2A), the base model has a maximum under- and overestimation of, approximately, -1.8 and +4.3 dB, respectively. Secondly, Figure 6.26b shows that in the 1-10 kHz natural frequency range the base model continuously overestimates the peak accelerations. This is shown more clearly in Figure 6.27a, where the error is seen to range from +1.1 to +5.0 dB.

In Figure 6.27, large differences are seen in the magnitude of the errors of the base model at different locations and frequency ranges. The errors registered at the dummy mass by accelerometer 2 seem, mostly, smaller than at other locations. However, test 3 shows a large overestimation of peak accelerations in the 1-10 kHz range. As seen in Figure 6.28, the SRS of accelerometer 2 in test 3 showed very similar behaviour as in test 2. However, at natural frequencies above 5 kHz, a sudden sharp rise is seen in the SRS of the base model. This rise is much stronger than in test 2, shown in Figure 6.26b.

Both test 2 and test 3 show that, in general, there is a higher positive than negative error. This indicates that the maximum overestimation of the peak accelerations is higher than the underestimation. A clear exception to this is shown by accelerometer 5 in the 10-100 Hz range.

When evaluating both the shock response spectra from Figure 6.26 as well as the maximum errors shown in Figure 6.27a, it is seen that, while the trend of the physical test and base

model SRSs are very similar, the maximum errors are still large. This is because the shock response spectra are not smooth, but show fickle behaviour with many peaks and troughs. It is expected that slight changes in the acceleration-time input of an SRS might alter the presence of such peaks and troughs without altering its trend.

Two possible reasons for such differences between the acceleration-time signal of the physical test and the base model are identified. Firstly, as with any numerical model, simplifications and assumptions were made during its creation. This leads to discrepancies between the impact test results and the model. A second contributing factor might instead lie in the impact tests. Slight imperfections and (environmental) disturbances may influence the test data. However, as each test is only performed once, it is not known how large this influence is. Therefore it cannot be said to what extent the discrepancy between the model and physical test result is caused by errors in the numerical model or by scatter of the test results.

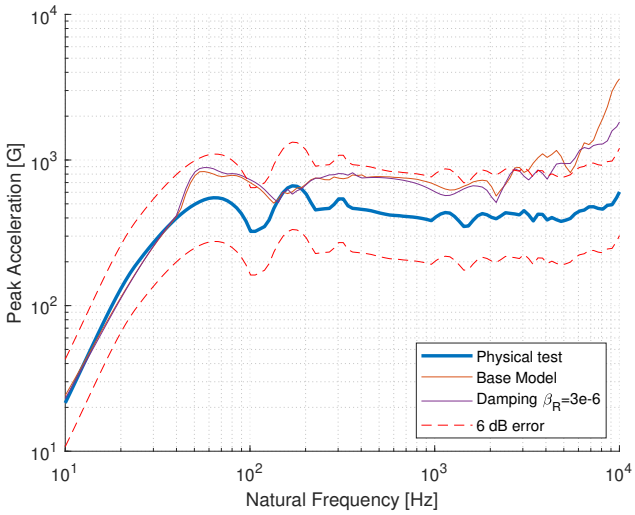

Figure 6.28: *Shock response spectrum of test 3, accelerometer 2, with Q=10. A comparison of the base numerical model, physical test and the β_R damped model.*

To investigate the sensitivity of the shock response spectra to the modelling changes described in Table 4.3, Figure 6.27 does not only show the errors of the base model shock response spectra, but also of the α_R and β_R damped models. The effect of adding damping can be clearly seen and agrees with what would be expected. Setting the low frequency damping parameter $\alpha_R = 50$ clearly lowers the peak accelerations, with the most prominent effect visible in the low natural frequencies. While this is seen at most locations and tests, for some this damping effect is very small.

Setting the high frequency damping parameter $\beta_R = 3e{-}6$ lowers the modelled response in the 1-10 kHz range for every test at each sensor location. At lower frequencies, the effect is very small. In most cases, the modelled response is overestimated at very high frequencies. Therefore, adding β_R damping often reduces the maximum absolute error in the 1-10 kHz range. This is most clearly seen in the SRS of accelerometer 2 in test 3 (Figure 6.28). The sharp rise above 5 kHz is limited due to the high frequency damping. Adding β_R damping may, however, increase the negative error. This can lead to an unconservative result. Therefore, care has to be taken in selecting a correct β_R damping parameter.

The sensitivity of the vibratory response to the plasticity of the rig, strain rate hardening effects and changing to the Lagrangian bird model are seen in Figures 6.29 and 6.30. All of these changes reduce the error at some natural frequencies while increasing them at others. Therefore, it is difficult to state which model variation best simulates the physical test. However, some aspects can be noted. Firstly, no clear improvement or deterioration is seen by using the Lagrangian bird model. Adding plastic behaviour to the test rig, however, does seem to reduce the error at most locations of the shock response spectra.

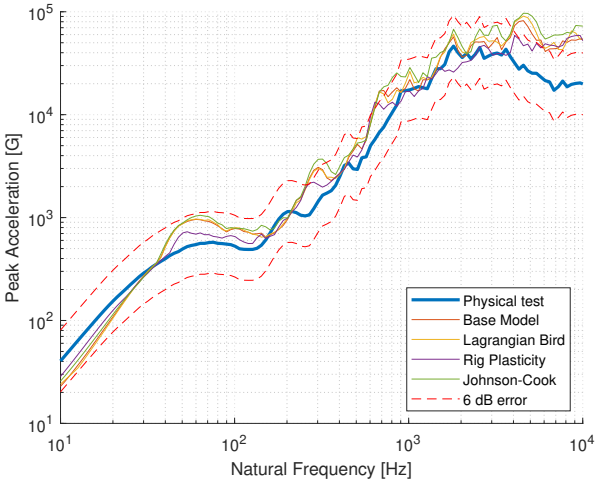

(a) *Accelerometer 1.*

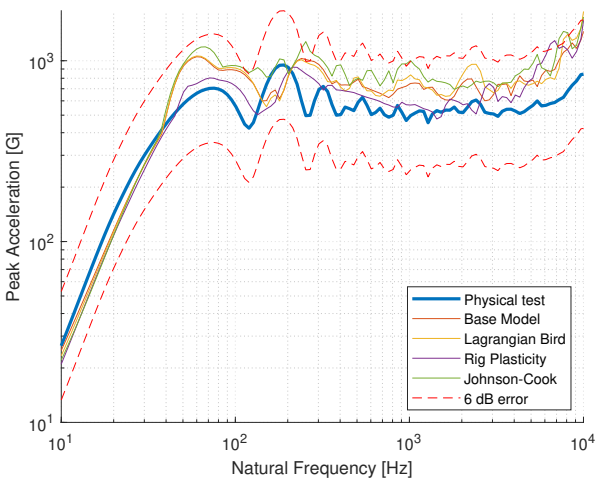

(b) *Accelerometer 2.*

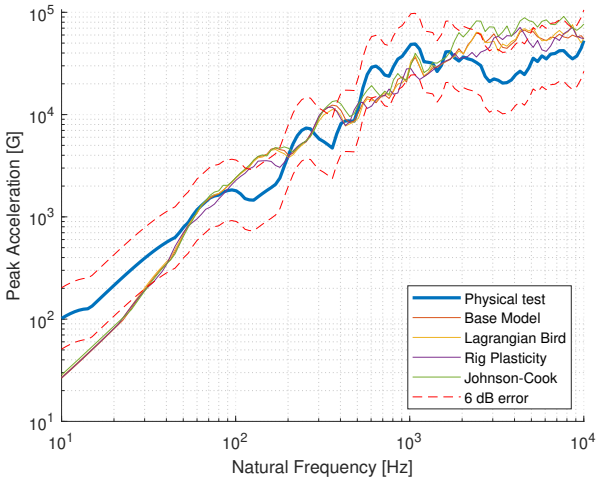

(c) *Accelerometer 5.*

Figure 6.29: *Shock response spectra of test 2, with Q=10. A comparison of the base, rig plasticity, Lagrangian bird and Johnson-Cook models.*

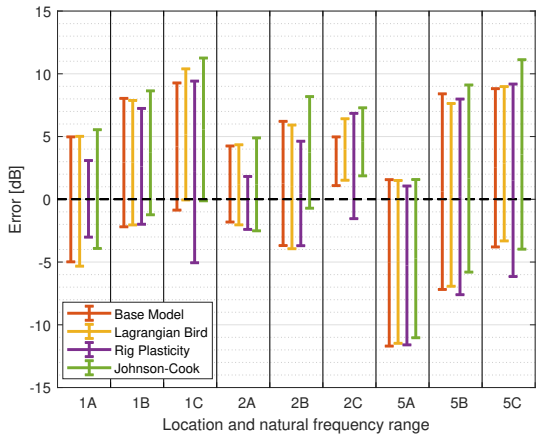

(a) *Test 2.*

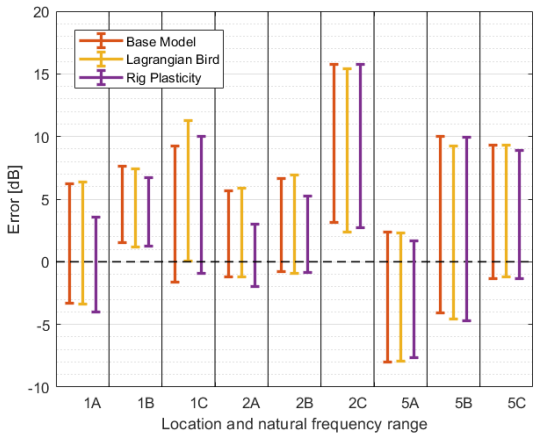

(b) *Test 3.*

Figure 6.30: *Discrepancy range between the SRS of the physical test and the numerical model for the flat plates. A comparison of the base, rig plasticity, Lagrangian bird and Johnson-Cook models. A, B and C denote the frequency range 10-100, 100-1000 and 1000-10000 Hz respectively.*

The numerical model using the Johnson-Cook definition for the aluminium alloy plate shows an increase of the shock response spectrum at medium and high natural frequencies. This is seen at all three accelerometers in test 2. In the low frequency range, this effect is less pronounced. This could be caused by the strain rate hardening effect. This increases the stiffness of the plate, which increases the natural frequency. In Figure 6.30a, it is seen that, for almost all accelerometers and frequency ranges, the Johnson-Cook material definition increased the errors of the SRS.

6.3.2. Stiffened plate vibratory response

The shock response spectra of the stiffened plate were also evaluated. Similarly to the flat plate results, the trend of the numerical shock response spectra in the stiffened plate tests seem similar to that of the physical test. However, the maximum errors are still quite large, especially for sensors 6 and 7. This is shown in Figure 6.31. These sensors were placed upon the dummy mass. That the model is not able to predict the vibrations at these specific locations can have several reasons. One of the more likely causes is that the vibrations must travel through several sets of fasteners to reach the dummy mass. Therefore, any inaccuracy in modelling these fasteners will lead an inaccuracy in the transferred signal. Secondly, the path through which the vibrations must travel is simply much longer than for the other sensors. It is to be expected that as the vibrations travel through the structure any inaccuracies will increase.

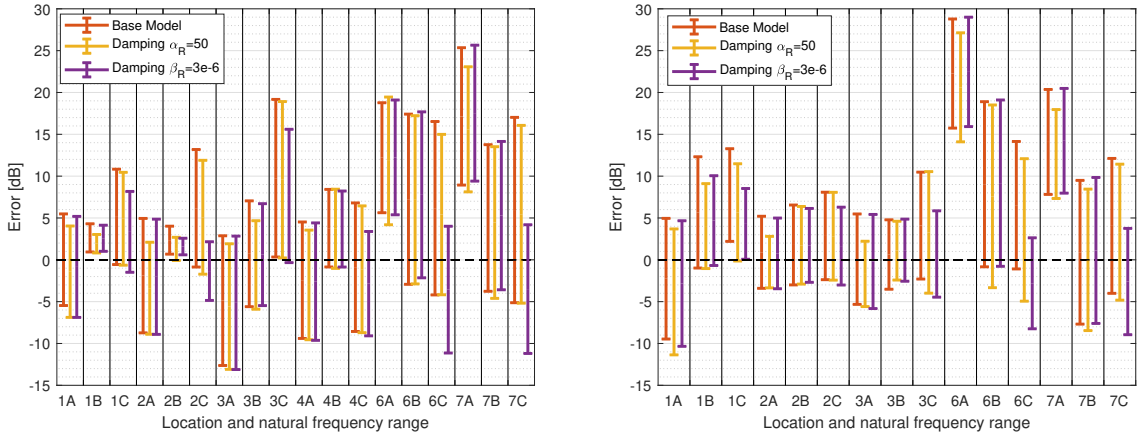

(a) *Test 4.* ***(b)*** *Test 5.*

Figure 6.31: *Discrepancy range between the SRS of the physical test and the numerical model for the Stiffened plates. A comparison of the base and damped models. A, B and C denote the frequency range 10-100, 100-1000 and 1000-10000 Hz respectively.*

Finally, the sensing direction of sensors 6 and 7 is aligned with the z- and y-axis, respectively. However, the main direction of acceleration of the dummy mass is the x-direction. As explained in Section 5.2.2, these accelerometers have a transverse sensitivity of up to 5%. As the accelerations in x-direction are much larger than in y- or z-direction, this transverse sensitivity can have a large erroneous effect on the accelerations measured by accelerometer 6 and 7. In the numerical model, this transverse sensitivity is not present. The discrepancy between physical test and numerical model results might therefore also indicate an error in the measured accelerations of the physical test instead of the numerical model.

When comparing the accuracy found in the different natural frequency ranges, it is seen that the largest negative and thus unconservative errors are seen in the 10-100 Hz frequency range. The only clear exceptions to this are seen in the data of accelerometers 6 and 7.

As explained in the introduction of this chapter, in test 4 and 5 all data from accelerometer 5 was lost. This is problematic as this is the most interesting sensor for the stiffened plate tests. This sensor is placed at the location of the dummy mass (the object of interest) in the

flight direction of the bird. This is the direction in which the largest vibrations were seen to occur.

7

Conclusions and recommendations

The objective of this thesis was to find out whether the vibratory response of an aircraft structure impacted by a bird can be modelled correctly using current state-of-the-art numerical modelling methods. Additionally, it was explored whether the way in which stress waves propagate through the structure is correctly shown in such models. The conclusions of this research, based on the formulated research questions, are given in Section 7.1. In Section 7.2, the most important recommendations for future research are stated.

7.1. Conclusions

To find the answer to these questions, several bird impact tests were performed by Airbus. These were carried out on plate structures, intended to give a simplified representation of an aircraft type structure. Three such tests were performed on a flat plate. Two more impact tests were done with a stiffened plate. To these test structures a dummy mass was attached, representing a system subjected to the vibrations induced by the bird impact. This was the starting point for the author of this thesis, who, with the exception of these impact tests, performed the complete work described in this research. Of each of these test structures, a numerical finite element model was created. By comparing the result of these models to the impact tests, the answer to both research questions could be determined.

Firstly, in the evaluation of the stress waves, it was found that the DIC data of the impact test showed too much disturbance to evaluate these waves. In the numerical model, both an in-plane and an out-of-plane stress wave is seen. Their recorded velocities are seen to approach their theoretical value as the mesh is refined. The propagation velocity of the out-of-plane stress wave is found to depend on the structure of the mesh. When propagating diagonally to the mesh, a lower wave propagation velocity is found compared to a wave travelling tangentially to the mesh. Secondly, from each acceleration measurement, a shock response spectrum is generated (SRS). As no research was available yet that analysed vibrations during bird impact, this technique was taken from the space industry. This is the first known research in which an SRS is applied to a bird impact problem. These SRSs are a way to indicate the severity and damaging potential of a vibration to a component. It is found that the trend of the SRSs obtained from the numerical model approximates the SRSs from the bird impact test closely. However, due to the fickle pattern of the SRSs, maximum discrepancies between model and test of 5 to 10 dB are common. In the next paragraphs, more details will be given regarding the validation of the model, the wave propagation and the shock response spectra, respectively.

Before the numerical models could be used to evaluate the research questions, they needed to be validated. This was done by comparing the dynamic behaviour of the flat and stiffened plate models to the bird impact tests. For the flat plate model, the displacement at the centre of impact was found to be modelled well for up to 5 ms after impact. After this, the centre

of the panel in the impact test remained at its displaced position for several milliseconds. In contrast, in the numerical base model, the plate returned towards its starting position quickly. This might be caused by a lack of plasticity in the material definition of the test rig. Adding plasticity to the test rig greatly improved the result for t>5 ms.

To determine the sensitivity of the numerical model to certain modelling changes, several more variations to the base model were created. Adding material damping to the model reduced the displacement of the plate, but, as test 2 overestimated but test 3 underestimated the displacement, it could not be deduced whether this effect was beneficial. Using a Lagrangian bird model instead of an SPH bird model had little influence on the dynamic behaviour of the structure, except for showing a slightly more gradual initial response. Switching to a Johnson-Cook material model for the flat plate significantly reduced the displacement response. This could be caused by the added strain rate hardening. Replacing the shell elements in the plate by 3D continuum elements was found to provide both benefits and drawbacks. By utilising 3D elements the geometry of the stiffened plate could be approximated much more accurately. However, when using 3D elements, multiple elements are needed through the thickness of the plate. This either leads to a high required computational effort or, when too few elements are used through the thickness, a less accurate result.

The influence of most model variations on calculation effort required was small. However, adding β_R damping increased the required calculation 19 and 25 fold for the flat and stiffened plate, respectively. Additionally, as modelling the flat plate with 3D elements required a much finer mesh, a similarly large increase in computational effort was seen. For more calculation-intensive simulations, this could be a limiting factor in implementing these changes.

The goal related to the first research question was to determine whether the stress waves that propagate the impact loads through the structure are correctly represented in the numerical model. Conclusions to this research question are detailed in the following paragraphs.

In the literature review, four types of stress waves were described. An attempt was made to identify two of these in both the physical test and the numerical model. These were the longitudinal wave and the Rayleigh wave. Two characteristics of these stress waves were used to identify them. The first is the direction in which each wave displaces the material through which it travels. The second is the propagation velocity of the wave type. The longitudinal wave has a high velocity and displaces the material tangentially to the wave propagation direction. The Rayleigh wave has a low velocity and induces an out-of-plane material movement.

Firstly, it was evaluated whether these stress waves could be seen in the physical bird impact tests. The goal was then to compare the wave propagation velocity of the physical impact test to the wave propagation velocity found in the numerical model. Unfortunately, there was too much disturbance in the DIC data of the impact tests to be able to correctly observe the displacement caused by the propagating stress waves. Therefore, the wave propagation velocity values found in the numerical model could not be compared to the impact tests. Instead, the results of the numerical model could only be compared to the theoretical stress wave velocity values.

To determine the wave propagation velocities in the numerical analysis, a separate, simplified model was created, consisting solely of a very large square plate, impacted by the bird at its centre. This was done to eliminate the effect of any obstructions or boundaries. The recording of the wave speeds in the numerical model was found to be dependent on the sensitivity of when a wave is said to pass a specific node. This sensitivity was denoted by the threshold value. For a longitudinal wave, the recorded wave speed in the numerical model maintained a relatively constant value for threshold values of 10^{-3} and smaller. When using an element size of 1.25 mm for the mesh, this recorded wave speed lies within a few percent of the theoretical longitudinal wave speed. Therefore, it can be concluded that the longitudinal wave is likely to be represented well in the numerical model.

The recorded out-of-plane wave speed reached a relatively constant value for threshold values between 10^{-4} and 10^{-11}. The value of the recorded out-of-plane wave velocity lies close to

the theoretical Rayleigh wave speed. For threshold values smaller than 10^{-11}, the recorded out of plane wave speed increases rapidly and approaches the longitudinal wave speed. It is expected that this is not caused by the out-of-plane wave itself. Instead, it might be a secondary effect of the longitudinal wave. If this wave would result in a displacement that is not purely in-plane, but also causes a small out-of-plane displacement, it would influence the recording of out-of-plane wave velocity.

It cannot be concluded with certainty whether the recorded out-of-plane wave speed velocity measurement was caused by the Rayleigh wave or some other out-of-plane displacement, such as a flexural wave. However, the recorded out-of-plane wave speed lies within 13% of the theoretical Rayleigh wave propagation velocity. Therefore, it is likely that it is the Rayleigh wave that has been identified.

The influence of mesh size, plasticity, bird impact velocity and Young's modulus on the recorded wave speed velocity was analysed using variations of the simplified plate model. By lowering the mesh size from 5.00 to 1.25 mm, the out-of-plane wave speed approached the theoretical Rayleigh wave speed more closely. Additionally, the recorded longitudinal wave velocity approached its theoretical value by refining the mesh. No clear change in the recorded wave speed was found when including plasticity in the material model of the plate. The same is true for increasing or decreasing the bird impact velocity by 25%. Increasing the Young's modulus by a factor of 1.5 increased both the longitudinal and out-of-plane wave speed by factor $\sqrt{1.5}$. This agrees with the theoretical wave speeds, which are proportional to the square of the Young's modulus.

The visual analysis of the stress wave propagation showed that the wave propagation velocity of the out-of-plane wave is dependent on the structure of the mesh. For a square mesh, a 17% lower wave speed velocity was found for a wave travelling diagonally through the mesh. The stress wave velocity measurements described above were all performed tangentially to the mesh. This might indicate that stress waves propagating in tangential direction to the mesh are more correctly represented in the numerical models than the stress waves propagating diagonally.

The wave propagation in the flat and stiffened plate was also analysed. It was found that, when the longitudinal wave interacts with obstructions, such as a stiffener or dummy mass, these in-plane waves are reflected as out-of-plane waves. The propagation of the longitudinal wave does not seem to be influenced by obstructions.

The second research question was whether current FEM modelling techniques could determine the severity of vibrations experienced by systems located near the impact. However, when the impact tests were performed to answer this question, no method had been selected yet to quantify and compare the severity and damaging potential of different vibrations. No research was found that evaluated the severity of vibrations during bird impacts. Therefore, the technique to convert an acceleration-time signal into a shock response spectrum was taken from the space sector. Such a conversion is deemed to be a good method to quantify the severity of the vibrations encountered after bird impact.

Using shock response spectra, the peak acceleration experienced by a system subjected to the vibration input was determined, as a function of the natural frequency of that specific system. At all 3 accelerometer locations, the base finite element model of the flat plate could predict the trend of the shock response spectra well. However, at high natural frequencies, the shock response spectra of the base model often diverged, showing an increase in peak acceleration that was not matched by the SRS of the physical test. Additionally, shock response spectrum graphs are full of small peaks and troughs and do not show a smooth line. While the general trend of the SRSs from the base model agreed with the physical test, these peaks and troughs were not always shown correctly in the numerical model results. Therefore, the maximum discrepancy was often high, with values between 5 and 10 dB being common. A maximum error of 16 dB was even recorded.

One reason that such valleys and troughs are not equal in physical test and numerical model may be the simplifications and assumptions used in the creation of the model. A second

reason for this difference in valleys and troughs might be the imperfections in the physical test. Each impact test was only performed once. Therefore, it can not be determined to what extent the shock response spectra of the physical tests would change if each test were to be carried out multiple times.

In the stiffened plate tests, the discrepancy between the SRSs of the impact tests and the base model varied much more than in the flat plate tests. One possible cause of this is that the accelerometers were installed in a direction perpendicular to the main vibration direction. The accelerometers may be somewhat sensitive to acceleration in the direction perpendicularly to its primary measurement direction. Thus, as the primary measurement direction does not align with the primary vibration direction, the acceleration measurement might be disturbed to a higher extent than it normally would. This effect is not present in the numerical model, leading to a discrepancy. The only accelerometer that was placed in the direction of vibration, which was placed on top of the dummy mass, failed during both stiffened plate impact tests. This leads to a certain incomparability of the test and model shock response spectra in the stiffened plate.

The sensitivity of the modelled shock response spectra to certain modelling changes was also investigated. Adding damping lowered the peak accelerations, with the biggest reduction being seen in the low- and high-frequency ranges for the α_R and β_R damping, respectively. Just like the global behaviour of the plates, the SRSs of the numerical model seem to more accurately represent the physical test when plastic deformation is being taken into account for the test rig. When replacing the SPH bird model by a Lagrangian bird model, no clear benefit or disadvantage to the accuracy of the modelled shock response spectra could be found.

The results found in this research show that finite element models can be used to predict the severity of vibrations in an aircraft structure impacted by a bird. However, the magnitude of the discrepancy between the SRS of the impact test and the model can be large. Therefore, a closer look will have to be taken at what is the cause of these discrepancies and how they can be reduced. The knowledge on vibratory response modelling of aircraft structures impacted by birds should, therefore, be expanded. If this is pursued, the combination of such models with analysis through shock response spectra might prove to be a capable future engineering tool that contributes to the safety of the aviation industry.

7.2. Recommendations

This thesis described an investigation into the stress wave propagation and the vibrations induced during a bird impact event on an aircraft structure. This section states the main recommendations for future research, based on the lessons learnt during this thesis.

The first test structure had accelerometers mounted at the centre of the plate. These were connected to the structure using bolts. As the bird directly impacted this location, the stress concentrations resulting from this connection caused the plate to rupture. Therefore, future tests will need to ensure no such alterations to the structure are present at the point of impact.

During the stiffened plate tests, the accelerometers mounted on the stiffeners were mounted such that their measurement direction was parallel to the impact direction of the bird. However, the main direction of vibration of these stiffeners was perpendicular to the stiffener orientation. Therefore, the highest magnitude vibrations were not captured at these locations. In future impact tests care will have to be taken that accelerometers are mounted in the main direction of vibration.

The bird impact tests that were performed are events in which high loads and accelerations occur. This caused several of the sensors to fail. This went unnoticed in between test 4 and 5, resulting in a lack of data in both tests. It is advised that, when sensors are reused, they are inspected in between tests.

In the base model, it was found that, contrary to expectations, the test rig is likely to have

plastically deformed during the impact tests. It is therefore advised that, even relatively far from the location of impact, plastic material behaviour may need to be taken into account. If new tests are performed the test structure will need to be inspected after the tests for signs of plastic deformation, such that this can be confirmed or refuted.

The numerical base models used conventional shell elements for all thin-walled structures. Therefore, the geometry of certain components was simplified. For the stiffened plate this resulted in an absence of fillets at the intersection of stiffeners. This might be one of the reasons why the measured displacement of the stiffened plate was too high. While the stiffened plate model using 3D elements did provide an approximation of the fillets, a lack of elements through the thickness of the plate meant that this model lacked stiffness in bending. One solution that should be explored is to use continuum shell elements. This could approximate the geometry of the plate more accurately while not suffering from the same problems as the 3D elements.

While four types of stress waves were described in the literature review, only the presence of the Rayleigh and longitudinal waves in the numerical model was evaluated. The shear wave was not evaluated while, due to the symmetry of the impact loading, a shear displacement was not expected in the plate. Flexural waves were not evaluated due to their dispersive nature. This causes them to have a variable wave velocity, making the evaluation method used in this thesis inapplicable. Future research could investigate whether these wave types are also found in these types of FE models. To do this, possibly more wave characteristics need to be evaluated than, merely, the wave velocity. If so, evaluating more characteristics would also give a more complete view on the longitudinal and Rayleigh waves.

The method of converting an acceleration signal into shock response spectra to analyse and compare vibrations was only found and selected in a later stage of this research. Therefore, not all relevant aspects could be taken into account. Any future research would benefit from selecting its analysis method earlier on, preferably before the impact tests are carried out. The most extensive guidance that was found on shock response spectra is the mechanical shock design and verification handbook [66]. Therefore, it is recommended that this handbook is consulted before additional tests are set up.

Analysis showed that, to correctly determine the shock response spectrum, acceleration measurements should be of sufficient duration. While in this research a minimum duration of 25 ms was seen to be needed this depends on the nature of the vibration. The longer it takes before the acceleration is damped out, the longer the required acceleration measured needs to be. Especially for simulations of large structures, for which computational time may be high, this might pose problems. Therefore, care will have to be taken to select an appropriate run time.

As discussed in the previous section, the shock response spectra have many troughs and valleys. These can result in large discrepancies between the impact test and model shock response spectra. As each bird impact test was only performed once, it was not known to what extent such discrepancies were influenced by the variability and scatter of the bird impact test results. Therefore, to reduce this uncertainty, it is advised that future impact tests are performed multiple times.

Bibliography

[1] Federal Aviation Administration (FAA), "Frequently asked questions and answers." Accessed: 12-04-2019, from https://www.faa.gov/airports/airport_safety/wildlife/faq/.

[2] T. Curtis, ed., *Raising Public Awareness of Bird Strike Risk Issues with an Enhanced Bird Strike Committee USA Web Site*, (Vancouver, BC), 1999 Bird Strike Committee-USA/Canada, First Joint Annual Meeting, May 1999.

[3] R. Dolbeer, J. Weller, A. Anderson, and M. Begier, "Wildlife strikes to civil aircraft in the united states, 1990–2015," tech. rep., Federal Aviation Administration, November 2016.

[4] International Civil Aviation Organization (ICAO), "2008 - 2015 wildlife strike analyses (IBIS)," tech. rep., Montreal, Canada, May 2017.

[5] European Union Aviation Safety Agency (EASA), "Certification memorandum," Tech. Rep. EASA CM-S–001 Issue:01, April 2012.

[6] N. Dennis and D. Lyle, "Bird strike damage & windshield bird strike - final report," Tech. Rep. 5078609-rep-03, Version 1.1, European Union Aviation Safety Agency (EASA), 2009.

[7] R. Hedayati, M. Sadighi, and M. Mohammadi-Aghdam, "On the difference of pressure readings from the numerical, experimental and theoretical results in different bird strike studies," *Aerospace Science and Technology*, vol. 32, pp. 260 – 266, January 2014.

[8] S. Heimbs, "Computational methods for bird strike simulations: A review," *Computers & Structures*, vol. 89, pp. 2093 – 2112, December 2011.

[9] J. Wilbeck, "Impact behaviour of low strength projectiles," Tech. Rep. AFML-TR-77-134, Wright-Patterson Air Force Base, 1978.

[10] H. Hopkins and H. Kolsky, "Mechanics of hypervelocity impact of solids," in *Proceedings of the Fourth Symposium on hypervelocity impact*, vol. 39, (Florida, United States of America), Air Proving Ground Center, Eglin Air Force Base, 1960.

[11] F. Allaeys, G. Luyckx, W. V. Paepegem, and J. Degrieck, "Numerical and experimental investigation of the shock and steady state pressures in the bird material during bird strike," *International Journal of Impact Engineering*, vol. 107, pp. 12 – 22, September 2017.

[12] U. Dar, W. Zhang, and Y. Xu, "FE analysis of dynamic response of aircraft windshield against bird impact," *International Journal of Aerospace Engineering*, vol. 2013, p. 12, April 2013.

[13] R. Banks and D. Chandrasekhara, "Experimental investigation of the penetration of a high-velocity gas jet through a liquid surface," *Journal of Fluid Mechanics*, vol. 15, no. 1, pp. 13 – 34, 1963.

[14] S. Leach and G. Walker, "The application of high speed liquid jets to cutting," in *Philosophical Transactions of the Royal Society of London*, vol. 260, pp. 295 – 308, July 1966.

[15] S. Abrate, "Soft impacts on aerospace structures," *Progress in Aerospace Sciences*, vol. 81, pp. 1 – 17, February 2016.

[16] A. Khan, R. Kapania, and E. Johnson, "A review of soft body impact on composite structure," in *Collection of Technical Papers - AIAA/ASME/ASCE/AHS/ASC Structures, Structural Dynamics and Materials Conference*, vol. 51, (Orlando, Florida), American Institute of Aeronautics and Astronautics, April 2010.

[17] M. McCarthy, J. Xiao, C. McCarthy, A. Kamoulakos, J. Ramos, J. Gallard, and V. Melito, "Modelling of bird strike on an aircraft wing leading edge made from fibre metal laminates – part 2: Modelling of impact with SPH bird model," *Applied Composite Materials*, vol. 11, pp. 317 – 340, September 2004.

[18] A. Riccio, R. Cristiano, S. Saputo, and A. Sellitto, "Numerical methodologies for simulating bird-strike on composite wings," *Composite Structures*, vol. 202, pp. 590 – 602, October 2018.

[19] C. Bisagni and M. Anghileri, "Specific problems related to simulation of a bird impact against a turbofan inlet," in *Proceedings of the International Crashworthiness Conference (ICrash 2000)*, (London, United Kingdom), pp. 652 – 662, The Royal Aeronautical Society, September 2000.

[20] C. Bisagni and M. Anghileri, "New model of bird strike against aircraft turbofan inlet," in *Proceedings of 3rd international KRASH conference*, (Tempe, Arizona, USA), pp. 8.3.1–8.3.11, Arizona State University, January 2001.

[21] L. Nizampatnam, *Models and Methods for Bird Strike Load Predictions*. PhD thesis, Wichita State University, December 2007.

[22] R. Hedayati and S. Ziaei-Rad, "A new bird model and the effect of bird geometry in impacts from various orientations," *Aerospace Science and Technology*, vol. 28, pp. 9 – 20, July 2013.

[23] I. Mohagheghian, Y. Wang, J. Zhou, L. Yu, X. Guo, Y. Yan, M. Charalambides, and J. Dear, "Deformation and damage mechanisms of laminated glass windows subjected to high velocity soft impact," *International Journal of Solids and Structures*, vol. 109, pp. 46 – 62, March 2017.

[24] D. Zhang and Q. Fei, "Effect of bird geometry and impact orientation in bird striking on a rotary jet-engine fan analysis using SPH method," *Aerospace Science and Technology*, vol. 54, pp. 320 – 329, July 2016.

[25] Dassault Systèmes, *Abaqus Analysis User's Guide*, April 2014.

[26] M. Anghileri, L. Castelletti, and V. Mazza, "Birdstrike: approaches to the analysis of impacts with penetration," in *International Conference on Impact Loading of Lightweight Structures, WIT Transactions on Engineering Sciences*, vol. 49, May 2005.

[27] F. Stoll and R. Brockman, "Finite element simulation of high-speed soft-body impacts," in *Proceedings of the 1997 38th AIAA/ASME/ASCE/AHS/ASC Structures, Structural Dynamics and Materials Conference*, (Kissimmee, Florida), pp. 334 – 344, University of Dayton Research Institute Dayton, April 1997.

[28] J. Liu, Y. Li, and X. Gao, "Bird strike on a flat plate: Experiments and numerical simulations," *International Journal of Impact Engineering*, vol. 70, pp. 21 – 37, August 2014.

[29] L. Yulong, Z. Yongkang, and X. Pu, "Study of similarity law for bird impact on structure," *Chinese Journal of Aeronautics*, vol. 21, pp. 512 – 517, December 2008.

[30] R. Brockman and T. Held, "Explicit finite element method for transparency impact analysis," Tech. Rep. WL-TR-91-3006, Wright Laboratory, Wright-Patterson air force base, Dayton, Ohio, June 1991.

[31] Y. Shmotin, P. Chupin, D. Gabov, V. Romanov, and S. Kukanov, "Bird strike analysis of aircraft engine fan," in *7th European LS-DYNA Conference*, (Salzburg, Austria), May 2009.

[32] S. Heimbs, U. Fischer, W. Theiler, and F. Steenbergen, "Numerical analysis of bird strike resistance of helicopter searchlight," in *Procedia Structural Integrity*, vol. 5, (Funchal, Madeira, Portugal), pp. 689 – 696, September 2017. 2nd International Conference on Structural Integrity, ICSI 2017.

[33] C. Rao, V. Narayanamurthy, and K. Simha, *Applied Impact Mechanics*. Chichester, United Kingdom: John Wiley & Sons Ltd, June 2016.

[34] S. Oller, *Nonlinear Dynamics of Structures*. Cham, Switzerland: Springer International Publishing AG, July 2014.

[35] C. Goyal, "Uncertainty quantification in non-linear seismic wave propagation," Master's thesis, Carleton University, 01 2017.

[36] R. Mao, S. Meguid, and T. Ng, "Transient three dimensional finite element analysis of a bird striking a fan blade," *International Journal of Mechanics and Materials in Design*, vol. 4, pp. 79 – 96, March 2008.

[37] J. Liu, Y. Li, X. Yu, X. Gao, and Z. Liu, "Design of aircraft structures against threat of bird strikes," *Chinese Journal of Aeronautics*, vol. 31, pp. 1535 – 1558, July 2018.

[38] G. Kay, "Failure modeling of titanium 6Al-4V and aluminum 2024-T3 with the Johnson-Cook material model," Tech. Rep. DOT/FAA/ARR-03/57, Lawrence Livermore National Laboratory, September 2003.

[39] J. Liu, Y. Li, X. Gao, and X. Yu, "A numerical model for bird strike on sidewall structure of an aircraft nose," *Chinese Journal of Aeronautics*, vol. 27, pp. 542 – 549, June 2014.

[40] I. Smojver, D. Ivančević, and D. Mihaljevic, "An explicit numerical modeling of soft body impact damage in metallic airplane structures," *Computer Modeling in Engineering and Sciences*, vol. 70, pp. 191–215, December 2010.

[41] G. Johnson and W. Cook, "A constituve model and data for metals subjected to large strains, high strain rates and high temperatures," in *Proceedings of the 7th International Symposium on Ballistics*, (The Hague, the Netherlands), pp. 541 – 547, April 1983.

[42] L. Fu, Z. Jiazhen, H. Zhongmin, and Z. Mingyi, "Numerical analysis of bird impact on a glare plate," *Polymers & Polymer Composites*, vol. 21, no. 9, pp. 587 – 592, 2013.

[43] R. Vignjevic, M. Orłowski, T. D. Vuyst, and J. Campbell, "A parametric study of bird strike on engine blades," *International Journal of Impact Engineering*, vol. 60, pp. 44 – 57, October 2013.

[44] B. Langrand, A.-S. Bayart, Y. Chauveau, and E. Deletombe, "Assessment of multi-physics FE methods for bird strike modelling-application to a metallic riveted airframe," *International Journal of Crashworthiness*, vol. 7, pp. 415 – 428, March 2002.

[45] M. Guida, F. Marulo, M. Meo, A. Grimaldi, and G. Olivares, "SPH – Lagrangian study of bird impact on leading edge wing," *Composite Structures*, vol. 93, pp. 1060 – 1071, February 2011.

[46] S. Zhu, M. Tong, and Y. Wang, "Experiment and numerical simulation of a full-scale aircraft windshield subjected to bird impact," in *50th AIAA/ASME/ASCE/AHS/ASC Structures, Structural Dynamics and Materials Conference*, (Palm Springs, California), May 2009.

[47] R. Mao, S. Meguid, and T. Ng, "Finite element modeling of a bird striking an engine fan blade," *Journal of Aircraft*, vol. 44, no. 2, pp. 583 – 596, 2007.

[48] R. Gingold and J. Monaghan, "Smoothed particle hydrodynamics: theory and application to non-spherical stars," *Monthly notices of the Royal Astronomical Society*, vol. 181, pp. 375 – 389, December 1977.

[49] L. Lucy, "A numerical approach to the testing of fission hypothesis," *The astronomical journal*, vol. 82, pp. 1013 – 1024, December 1977.

[50] P. Groenenboom, "Numerical simulation of 2D and 3D hypervelocity impact using the SPH option in PAM-SHOCK™," *International Journal of Impact Engineering*, vol. 20, pp. 309 – 323, January 1997.

[51] S. Audic, M. Berthillier, J. Bonini, H. Bung, and A. Combescure, "Prediction of bird impact in hollow fan blades," in *36th AIAA/ASME/SAE/ASEE joint propulsion conference and exhibit*, (Huntsville, Alabama), p. 3201, American Institute of Aeronautics and Astronautics, July 2000.

[52] C. Bisagni and M. Anghileri, "Specific problems related to a bird impact against a turbofan inlet," in *CEAS Forum on Crash Questions*, (Capua, Italy), pp. 199 – 211, CIRA, February 2000.

[53] C. Huertas-Ortecho, "Robust bird-strike modeling using LS-DYNA," Master's thesis, University of Puerto Rico, Mayaguez Campus, 2006.

[54] L. Castelletti and M. Anghileri, "Multiple birdstrike analysis: a survey of feasible techniques," in *30th European Rotorcraft Forum*, (Marseilles, France), pp. 495 – 505, September 2004.

[55] Y. Meleán, L. Sigalotti, and A. Hasmy, "On the SPH tensile instability in forming viscous liquid drops," *Computer Physics Communications*, vol. 157, pp. 191 – 200, March 2004.

[56] J. Monaghan, "SPH without a tensile instability," *Journal of Computational Physics*, vol. 159, pp. 290 – 311, April 2000.

[57] A. Airoldi and B. Cacchione, "Modelling of impact forces and pressures in Lagrangian bird strike analyses," *International Journal of Impact Engineering*, vol. 32, pp. 1651 – 1677, October 2006.

[58] S. Meguid, R. Mao, and T. Ng, "FE analysis of geometry effects of an artificial bird striking an aeroengine fan blade," *International Journal of Impact Engineering*, vol. 35, pp. 487 – 498, June 2008.

[59] S. McCallum and C. Constantinou, "The influence of bird-shape in bird-strike analysis," in *5th European LS-DYNA Users Conference*, (Birmingham, United Kingdom), May 2005.

[60] S. Hiermaier, *Structures under crash and impact: continuum mechanics, discretization and experimental characterization*. New York, United States of America: Springer Science+Business Media, 2008.

[61] V. Giurgiutiu, *Structural Health Monitoring with Piezoelectric Wafer Active Sensors*. Oxford, United Kingdom: Academic Press, second ed., 2014.

[62] J. Doyle, *Wave Propagation in Structures: Spectral Analysis Using Fast Discrete Fourier Transforms*. New York, United States of America: Springer Science+Business Media New York, second ed., 1997.

[63] Endevco, "Piezoresistive accelerometer model 7270a datasheet." Accessed: 18-08-2019, from `https://buy.endevco.com/ContentStore/MktgContent/Endevco/Datasheet/7270A_DS_083119.pdf`.

[64] HBM, "LY Linear Strain Gauges with 1 Measuring Grid." Accessed: 18-08-2019, from `https://www.hbm.com/en/4561/ly-linear-strain-gauges-with-1-measurement-grid/`.

[65] H. Huth, “Influence of fastener flexibility on the prediction of load transfer and fatigue life for multiple-row joints,” in *Fatigue in Mechanically Fastened Composite and Metallic Joints* (J. Potter, ed.), pp. 221–250, ASTM International, January 1986.

[66] European Cooperation for Space Standardisation, “Space engineering: Mechanical shock design and verification handbook,” tech. rep., ESA-ESTEC Requirements and Standards Division, Noordwijk, the Netherlands, July 2015.

[67] F. Serón, F. Sanz, M. Kindelán, and J. Badal, “Finite-element method for elastic wave propagation,” *Communications in Applied Numerical Methods*, vol. 6, pp. 359–368, July 1990.

[68] T. Irvine, “An introduction to the shock response spectrum,” July 2012. Accessed: 29-12-2019 from www.vibrationdata.com.

[69] D. Smallwood, “An improved recursive formula for calculating shock response spectra,” *Shock and Vibration Bulletin*, vol. 51, no. 2, pp. 211–217, 1981.

[70] T. Irvine, “Derivation of the filter coefficients for the ramp invariant method as applied to base excitation of a single-degree-of-freedom system - revision E,” September 2019. Accessed: 16-09-2019 from www.vibrationdata.com.

[71] H. Himelblau, A. Piersol, J. Wise, and M. Grundvig, *Handbook for Dynamic Data Acquisition and Analysis - IES Recommended Practices 012.1*. Institute of Environmental Sciences and Technology, 1994.

[72] Endevco, “Ask the experts: What does the transverse sensitivity specification mean in an accelerometer datasheet?.” Accessed: 12-01-2020 from https://endevco.com/Our-Resources/ask-the-experts/What-does-the-transverse-sensitivity-specification-mean-in-an-accelerometer-datasheet.

[73] A. Piersol, “Pyroshock data acquisition and analysis for U/RGM-109D payload cover ejection tests,” Tech. Rep. NWC TP 6927, Naval Weapons Center, China Lake, CA, 1988.

[74] H. Zhao, J. Ding, W. Zhu, Y. Sun, and Y. Liu, “Shock response prediction of the typical structure in spacecraft based on the hybrid modeling techniques,” *Aerospace Science and Technology*, vol. 89, pp. 460 – 467, 2019.